Material Failure Simulation with Random Microstructure using Lattice Particle Method and Neural Network

by

Haoyang Wei

A Dissertation Presented in Partial Fulfillment
of the Requirements for the Degree
Doctor of Philosophy

Approved April 2021 by the
Graduate Supervisory Committee:

Yongming Liu, Chair
Aditi Chattopadhyay
Hanqing Jiang
Yang Jiao
Jay Oswald

ARIZONA STATE UNIVERSITY

May 2021

ABSTRACT

Extensive efforts have been devoted to understanding material failure in the last several decades. A suitable numerical method and specific failure criteria are required for failure simulation. The finite element method (FEM) is the most widely used approach for material mechanical modelling. Since FEM is based on partial differential equations, it is hard to solve problems involving spatial discontinuities, such as fracture and material interface. Due to their intrinsic characteristics of integro-differential governing equations, discontinuous approaches are more suitable for problems involving spatial discontinuities, such as lattice spring method, discrete element method, and peridynamics. A recently proposed lattice particle method is shown to have no restriction of Poisson's ratio, which is very common in discontinuous methods. In this study, the lattice particle method is adopted to study failure problems. In addition of numerical method, failure criterion is essential for failure simulations. In this study, multiaxial fatigue failure is investigated and then applied to the adopted method. Another critical issue of failure simulation is that the simulation process is time-consuming. To reduce computational cost, the lattice particle method can be partly replaced by neural network model.

First, the development of a nonlocal maximum distortion energy criterion in the framework of a Lattice Particle Model (LPM) is presented for modeling of elastoplastic materials. The basic idea is to decompose the energy of a discrete material point into dilatational and distortional components, and plastic yielding of bonds associated with this material point is assumed to occur only when the distortional component reaches a critical value. Then, two multiaxial fatigue models are proposed for random loading and biaxial tension-tension loading,

respectively. Following this, fatigue cracking in homogeneous and composite materials is studied using the lattice particle method and the proposed multiaxial fatigue model. Bi-phase material fatigue crack simulation is performed. Next, an integration of an efficient deep learning model and the lattice particle method is presented to predict fracture pattern for arbitrary microstructure and loading conditions. With this integration, computational accuracy and efficiency are both considered. Finally, some conclusion and discussion based on this study are drawn.

ACKNOWLEDGMENTS

Firstly, I would like to thank my advisor, Professor Yongming Liu, for his guidance and support throughout the years at Arizona State University. His intellectual and professional suggestions helped me a lot of my research. I am grateful to him for his sincere care for not only my research but also my career development.

I would also like to thank all members of my dissertation supervisory committee, Professor Aditi Chattopadhyay, Professor Hanqing Jiang, Professor Yang Jiao and Professor Jay Oswald. Without their help, I cannot complete this work.

I would like to express my great gratitude to the former and current members of Prognostic Analysis and Reliability Assessment (PARA) group. Without them, my stay at Arizona State University would not have been wonderful as it is now. Special thanks go to Dr. Hailong Chen for an internship opportunity he provided at Idaho National Laboratory and his instructions of computational mechanics. I would like to thank Dr. Tishun Peng for his care of my work and life. I also want to thank Yi Gao for many discussions and collaborations.

Last but not least, I appreciate all encouragement, support and love from my family and friends over years. I know I owe a special thanks to my parents for their unconditional support of all my decisions.

TABLE OF CONTENTS

Page

CHAPTER Page

LIST OF TABLES

Table Page

LIST OF FIGURES

Figure Page

Figure Page

1. INTRODUCTION

1.1 Motivation and Objects

Material failure is a catastrophic issue for many practical engineering structures and components. Accurate fracture prediction is necessary to ensure the safety of these structures and components. Since material failure problems involves a couple of complex stress states, different orientation of crack and randomness of material microstructure, it is a challenge to simulate material failure precisely and efficiently. A suitable numerical method and specific failure criteria are required for failure simulation. Besides, computational cost of simulation should be considered.

For materials mechanical modeling, both continuous and discontinuous approaches have been extensively and intensively developed. The continuous approaches assume that the material is continuous in the domain. Numerical methods such as finite element methods (FEM), finite difference methods (FDM), and many other schemes belong to this category. The FEM is the most widely used approach for material mechanical modelling. Since FEM is based on partial differential equations, it may be hard to solve problems involving spatial discontinuities, such as fracture and material interface. Because there is singularity issue due to the spatial derivative at the discontinuities. Some techniques are required before continuous approaches can solve the discontinuous problems. Most of techniques treat every new configuration as every new problem with the crack surface and boundary conditions change by crack propagation. The adaptive remeshing technique[1], cohesive element[2], the level set methods and crack tip/front enrichment are among the most frequently used techniques in continuous approaches.

Due to their intrinsic characteristics of integro-differential governing equations, discontinuous approaches are more suitable for problems involving spatial discontinuities. Numerical methods such as discrete element methods (DEM)[3], lattice spring methods (LSM)[4], Peridynamics[5], and other discrete formulations belong to this category. One group of models in the discontinuous approach is the lattice models. The origin of lattice models can be traced back to the work by Hrennikoff[6], in which framework method has been firstly used to solve elasticity problems. Comparing continuous approaches, lattice models are natural for crack propagation with bond breakage between two lattices. There is a well-known restriction on effective Poisson's ratio for discontinuous approached[7], due to using only one spring parameter. The Poisson's ratio is fixed to 1/4 for plane strain and 1/3 for plane stress. Chen has developed a non-local lattice particle method LPM)[8], which has no restriction of Poisson's ratio. Because the interaction is determined by not only local two particles but also nonlocal neighbors. LPM is adopted in this study as a numerical method for failure simulation. However, the proposed model is limited to simulate brittle or quasi brittle material behavior, because there is not rigorous plasticity theory for the model. Thus, in order to widely using LPM in ductile or general material, a rigorous plasticity is needed, including equivalent yield criterion, flow rule and strain hardening rule.

It has demonstrated that the fracture failure process can be simulated using LPM[9], [10]. Bonds in LPM are set to be broken once they reach a critical value, which can be a specific bond stretch or bond force. Currently, there is not a fatigue criterion for LPM to simulate fatigue failure process under cyclic loadings. Fatigue is a major failure mode, and multiaxial fatigue is a complex problem. It is commonly seen in many mechanical and structural components. Extensive models have been proposed for the multiaxial fatigue life prediction,

especially during the past two decades. In general, the multiaxial fatigue models can be classified into four major categories: stress-based [11], [12], strain-based [13], [14], energy-based [15], [16], and fracture mechanics-based approaches [17] In recent years, fatigue models based on the critical plane approach for multiaxial fatigue evaluation have been gaining popularity due to their success in accurately predicting lives. Many models assume the maximum shear stress range plane as the critical plane which is suitable for ductile failure [18]–[20]. Other models assume that the maximum normal stress range plane as the critical plane which is mostly suitable for brittle failure [21]–[23]. However, when these two failure modes mix or the material is neither ductile nor brittle, it is hard to select an appropriate mode. Several attempts trying to solve these issues have been proposed in the past. One successful approach is to let the critical plane change its orientation for different failure modes, i.e., along the maximum normal stress range plane for brittle materials and along the maximum shear stress range plane for ductile materials. The concept was initially done by an empirical function [24]–[27]. Liu and Mahadevan [28], [29] proposed an analytical solution for the critical plane orientation based on the material ductility in stress and strain terms. Wei and Liu extended the Liu-Mahadevan critical plane concept in energy terms, which includes out-of-phase hardening without additional calibration[30]. Previous investigation of the Liu-Mahadevan critical plane concept focuses on constant loadings. The Liu-Mahadevan critical plane concept extension for random loadings is in demand. The authors observed that most critical plane-based approaches ignore the damage contribution from axial stress/strain parallel to the critical plane (in another words, hydrostatic stress/strain components). This approach may be appropriate under uniaxial loadings and tension-torsion loadings but is questionable for biaxial tension-tension loading.

It should be noticed that the stress state in LPM is more complex than uniaxial or tension-torsion loadings. A universal multiaxial fatigue model is still lacking for LPM.

Failure simulation is a nonlinear process, because material stiffness is decreasing during crack propagation. An integration of incremental method with numerical method is needed to solve nonlinear problems, which involving a lot of iterations. Therefore, the incremental method brings high computational cost. Besides, in order to obtain accurate failure simulation, a large number of particles is required in LPM, which makes the LPM simulation time-consuming. Neural network is a hot topic since it shows the power to solve many complicated problems, in which nonlinear process is included. LPM can be partly replaced by neural network to reduce simulation time.

Based on the discussion above, the objectives of this research work are summarized below:

- Propose a rigorous plasticity formulation for LPM. The formulation is based on the maximum distortional energy. The corresponding equivalent strain hardening rules are also developed.
- Investigate multiaxial fatigue model. The Liu-Mahadevan critical plane concept is extended for random loading scenario, and a universal multiaxial fatigue model is proposed to address fatigue damage under complex loading rather than tension-torsion loading.
- Combine the proposed universal fatigue model and LPM to investigate fatigue problems, such as fatigue initiation and fatigue crack propagation. LPM scheme with the fatigue model can simulate fatigue behavior of material with arbitrary

geometries, under complex loading conditions. Furthermore, microstructural effect on fatigue problem can also be studied.

- Propose a neural network working with LPM to reduce computational cost of fracture simulation. The LPM is used for linear elastic deformation, and the neural network handles the following nonlinear fracture process. This integration of LPM and neural network takes advantages of accuracy of LPM and efficiency of neural network.

1.2 Outlines of the Dissertation

This report contains four chapters and is organized as follows:

Chapter 2 presents the development of a nonlocal maximum distortion energy criterion in the framework of a Lattice Particle Model for modeling of elastoplastic materials. Similar to the maximum distortion energy criterion in continuum mechanics, the basic idea is to decompose the energy of a discrete material point into dilatational and distortional components, and plastic yielding of bonds associated with this material point is assumed to occur only when the distortional component reaches a critical value. Formulation of equivalent strain hardening rules for the nonlocal yield model were also developed.

Chapter 3 focuses on the development of a multiaxial fatigue life prediction model under general multiaxial random loadings. The new model development based on the Liu-Mahadevan critical plane concept for random loading is presented. The key concept is to use two-steps to identify the critical plane: identify the maximum damage plane due to normal stress and calculate the critical plane orientation with respect to the maximum damage plane due to normal stress. The equivalent stress is then used for fatigue life predictions.

Chapter 4 proposes a new energy-based fatigue life prediction model for arbitrary multiaxial constant loadings in this paper. The proposed multiaxial fatigue model includes damage contributions of equivalent tensile energy, torsional energy, and hydrostatic energy, which can handle not only tension-torsion loadings but also tension-torsion loadings. The proposed model is validated with extensive experimental data under both tension-torsion loadings and biaxial tension-tension loadings from open literature. Comparison with several widely used multiaxial model is also given to show the model performance with respect to different biaxial tension-tension loadings.

Chapter 5 studied fatigue cracking in homogeneous and composite materials using LPM. The proposed energy-based fatigue criterion in Chapter 4 is implemented in LPM scheme to analysis fatigue crack initiation and propagation. Bi-phase material fatigue crack simulation is performed.

Chapter 6 proposed an integration of an efficient deep learning model and LPM to predict fracture pattern for arbitrary microstructure and loading conditions. LPM and the proposed deep learning model are combined for the linear stage and nonlinear stage, respectively. LPM is also used here to generate a training dataset of fracture pattern. With this integration, computational accuracy and efficiency are both considered. Several scenarios of various microstructure and random loading are studied.

Chapter 7 is devoted to some conclusion of the research work in this dissertation and scope of potential work in the future.

2. A LATTICE PARTICLE MODEL FOR ELASTOPLASTIC MATERIAL

In virtue of their intrinsic integro-differential formulation of underlying physical behavior of materials, discontinuous computational methods are more beneficial over continuum-mechanics-based approaches for materials failure modeling and simulation. However, application of most discontinuous methods is limited to elastic/brittle materials, which is partially due to their formulations are based on force and displacement rather than stress and strain measures as are the cases for continuous approaches. In this paper, we formulate a nonlocal maximum distortion energy criterion in the framework of a Lattice Particle Model for modeling of elastoplastic materials. Similar to the maximum distortion energy criterion in continuum mechanics, the basic idea is to decompose the energy of a discrete material point into dilatational and distortional components, and plastic yielding of bonds associated with this material point is assumed to occur only when the distortional component reaches a critical value. However, the formulated yield criterion is nonlocal since the energy of a material point depends on the deformation of all the bonds associated with this material point. Formulation of equivalent strain hardening rules for the nonlocal yield model were also developed. Compared to theoretical and numerical solutions of several benchmark problems, the proposed formulation can accurately predict both the stress-strain curves and the deformation fields under monotonic loading and cyclic loading with different strain hardening cases.

2.1 Introduction

For materials mechanical modeling, both continuous and discontinuous approaches have been extensively and intensively developed. Due to their intrinsic characteristics of integro-differential governing equations, discontinuous approaches are more suitable for problems involving spatial discontinuities, such as crack and material interface. Detailed review and

comparison of these two approaches is beyond the scope of this paper and can be found elsewhere, such as Refs[31], [32]. A brief review on relevant studies is given below.

One group of models in the discontinuous approach is the lattice models. The origin of lattice models can be traced back to the work by Hrennikoff[6], in which framework method has been firstly used to solve elasticity problems. Subsequent developments have been focused on studying the elastic/brittle behavior of solid materials. A large volume of research on this topic can be found in the literature[33]–[41]. Detailed review on lattice models can be found in Refs[4], [42]–[44].

Compared to the large amount of research for elastic problems using lattice models, there are very few studies focus on the development of elastoplastic modeling capability for lattice models. Buxton et al.[45] introduced plasticity into the classical Born spring model[46] by decreasing the elastic moduli locally whilst maintaining stress continuity. This model has the problem of fixed upper bound of a quarter for the Poisson's ratio irrespective of volume conservation for plastic deformation. Zhao et al.[47] recently implemented a modified Drucker-Prager model in the lattice spring model for plasticity and fracture problems. The basic idea was to construct displacement fields for each lattice point using the least square technique and the strain field was then obtained to develop the plasticity model. Plasticity has also been developed for other discontinuous lattice-like models, such as discrete element method[48], [49] and peridynamics[5], [50], [51].

Among various lattice models, the Lattice Particle Model (LPM)[52], [53] is a recently developed nonlocal reformulation of the conventional lattice model. LPM is distinct from other lattice models at least in following aspects: (1) only axial bonds is used to maintain both formulation and implementation simplicities of the conventional lattice models while being

able to model advanced complex material behavior; (2) inspired by the Embedded Atom Method (EAM)[54], a multi-body potential is introduced in addition to the pair-wise potential to fix the issue of limited range of materials Poisson's ratio; (3) rather than material stiffness matrix transformation, material anisotropy can be represented uniquely in LPM by lattice rotation scheme[10]. Similar to other lattice models, LPM discretizes the domain of interest into regularly packed particles (or material points) system. The motion of each discrete material point is governed by integro-differential equations rather than partial differential equations, which better avoids the spatial discontinuities resulted singularity issues. Crack nucleation and propagation can be modelled using the breakage of active bonds connecting material points. LPM is nonlocal in the sense that the interaction between two neighboring material points depends on not only the deformation states of the material points themselves but also all the neighboring material points surrounding these two material points. This nonlocality is a direct result of the introduction of a nonlocal multi-body energy term in addition to the local pair-wise energy in the potential formulation at each discrete material point.

Developments of LPM have been focused on elastic materials[52], [53], [55], however, a rigorous formulation of LPM for ductile materials is still lacking. Chen et al.[56] proposed a local bond stretch based yield criterion for modeling elastoplastic materials using LPM. This bond stretch based yield criterion is local and only depends on the deformation states of the two material points, which is inconsistent with the nonlocality formulation of LPM. Also, the critical value needs to be calibrated based on a given material's yield stress and it is lattice structure dependent. What's more important, deformation isotropy cannot be guaranteed during elastoplastic modeling of an isotropic material. This bond stretch-based yield criterion

can only be used to simulate elastoplastic deformation where the nonlocal contribution is negligible. For arbitrary geometries and multiaxial loading, bond stretch-based yield criterion is difficult to be used as no explicit yielding condition is defined and trial-and-error method is needed for model calibration.

Based on the above discussion, it is the goal of this study to develop a rigorous yield criterion to model elastoplastic material using the three-dimensional LPM. Since the focus of this study is to develop a valid yield criterion and establish its validity and prediction accuracy, application of the developed yield criterion to study fracture of ductile materials is out of the scope of this study. The remainder of this paper is organized as follows: First, a brief review of LPM formulation for elastic materials is presented in Section 2. Derived LPM parameters in terms of material constants for different lattice structures are provided. Following this, the proposed nonlocal maximum distortion energy criterion is formulated based on the concept of energy separation into dilatational and distortional parts, in which the distortion energy governs the state of plastic deformation. Important ingredients including additive decomposition of bond stretch, incremental LPM formulation for plastic analysis, yield function, consistency conditions and equivalent strain hardening rules are discussed. Implicit solution scheme for plastic analysis in LPM is outlined in Section 4. In Section 5, numerical examples considering different geometries and loading scenarios are studied using the proposed nonlocal yield criterion. LPM predictions are compared with theoretical benchmarks and numerical solutions. Discussions and conclusions based on the proposed study are drawn in Section 6.

2.2 Brief Review of Lattice Particle Model for Elastic Materials

Similar to other lattice models[44], the LPM formulation depends on the lattice structure used to discretize the solution domain. So far, five different types of lattice structures have

been used in LPM. These lattice structures are triangular and square lattice structures for two-dimensional analyses and simple cubic, body-centered cubic and face-centered cubic lattice structures for three-dimensional analyses. In LPM, a typical material point can interact with its neighboring material points up to certain distance via bonds. For a given interaction distance, different unit cells are identified for different type of neighbors (e.g., a unit cell for the first nearest neighbors and a second unit cell for the second nearest neighbors etc.). The potential energy for a material point is the summation of the energy associated with all these unit cells. For each unit cell, its energy is the summation of a local pairwise energy corresponding to the stretch of the bond connecting two material points and a non-local multi-body energy associated with volume change of a unit cell. For a material point *I*, the energy in one of its unit cell can be generally written as

$$U_I = U_I^{local} + U_I^{nonlocal} \tag{2.1}$$

with the local energy U_I^{local} can be expressed in terms of bond length change between material point *I* and its neighbors of the same unit cell as

$$U_I^{local} = \frac{1}{2}\sum_{J=1}^{N_I} k_{IJ}\left(\delta l_{IJ}\right)^2 \tag{2.2}$$

and the nonlocal energy $U_I^{nonlocal}$ as

$$U_I^{nonlocal} = \frac{1}{2}T_I\left(\sum_{J=1}^{N_I}\delta l_{IJ}\right)^2 \tag{2.3}$$

In Eqs.(2.2) and (2.3), k_{IJ} is the local parameter for bond *IJ*, T_I is the nonlocal parameter associated with the summation of all length change for a unit cell, δl_{IJ} is the length change of

bond IJ, N_I is the total number of neighboring material points interacting with material point I or bonds connected with material point I for the same unit cell.

Equating the energy of a material point in LPM to its continuum counterpart, the material stiffness tensor can be obtained by theory of hyperelasticity as

$$C_{ijkl} = \frac{1}{V_I} \frac{\partial^2 \sum U_I}{\partial \varepsilon_{ij} \partial \varepsilon_{kl}} \tag{2.4}$$

where ε_{ij} is the continuum strain tensor at a material point.

For small deformation problem, the bond length change can be related to the strain tensor using following relationship[57]

$$\varepsilon_{IJ} = \frac{\delta l_{IJ}}{L_{IJ}} = \varepsilon_{ij} n_i n_j \tag{2.5}$$

where L_{IJ} is the initial length, n_i and n_j are the components of unit vector in the bond direction.

LPM parameters can be determined by comparing the material stiffness tensor given in Eq.(2.4) with that of generalized Hooke's law. Certain constraint(s) needs to be imposed between LPM parameters for different neighbors, such as k and T should be the same for the same type of neighbors for an isotropic material. For isotropic materials, the derived LPM parameters in terms of material constants for different lattice structures are given in Table 2-1.

Table 0-1 LPM Parameters for Isotropic

(using both 1st and 2nd nearest neighbors)	Local parameter k (k_1, k_2)	Nonlocal parameter T
Triangular lattice (only 1st nearest neighbors)	$k = \frac{4E}{\sqrt{3}(1+\nu)}$	$T = \frac{E(3\nu-1)(1-\nu)}{2(1+\nu)(1-2\nu)^2}$

Square lattice	$k_1 = \frac{2E}{(1+\nu)}, k_2 = \frac{E}{(1+\nu)}$	$T = \frac{E(4\nu-1)}{2(1+\nu)(1-2\nu)}$
Simple cubic lattice	$k = \frac{2RE}{1+\nu}$	$T = \frac{RE(4\nu-1)}{9(1+\nu)(1-2\nu)}$
Face-centered cubic lattice	$k_1 = \frac{2\sqrt{3}RE}{1+\nu}, k_2 = \frac{2}{3}\frac{2\sqrt{3}RE}{1+\nu}$	$T = \frac{\sqrt{2}RE(4\nu-1)}{12(1+\nu)(1-2\nu)}$
Body-centered cubic lattice	$k_1 = \frac{2\sqrt{3}RE}{1+\nu}, k_2 = \frac{2}{3}\frac{2\sqrt{3}RE}{1+\nu}$	$T = \frac{\sqrt{3}RE(4\nu-1)}{7(1+\nu)(1-2\nu)}$

Given the LPM parameters, the interaction in bond *IJ* between material point *I* and its neighbor *J* can be determined by differentiating the total energy with respect to its length change as

$$\mathbf{f}_{IJ} = \frac{\partial U_I}{\partial \delta l_{IJ}} \mathbf{n}_{IJ} \tag{2.6}$$

In LPM, the equation of motion for a material point *I* at time t is given by

$$m_I \ddot{\mathbf{u}}_I\left(t, \mathbf{x}_I\right) = \sum_{J=1}^{N_I} \mathbf{f}_{IJ}\left(t, \mathbf{x}_I, ..., \mathbf{x}_J\right) + \mathbf{b}_I\left(t, \mathbf{x}_I\right) \qquad \forall\left(I,t\right) \in \Omega \times \left(0,\tau\right) \tag{2.7}$$

where m is the mass scalar, $\mathbf{u}$ is the displacement vector, $\mathbf{f}_{IJ}$ is the interaction force from neighbor *J*, and $\mathbf{b}_I$ is external body force.

2.3 Proposed Maximum Distortion Energy Criterion for Lattice Particle Model

As discussed in previous section, formulation of LPM for elastic/brittle materials is straightforward, and it is based on the theory of hyperelasticity and generalized Hooke's Law. However, for elastoplastic materials, the formulation is quite involved, and all the details will be presented in this section. Firstly, additive decomposition of bond stretch into elastic and plastic parts is discussed. Following this, derivation of model parameters for incremental LPM

formulation for plastic deformation analysis is presented. Next, the energy of an LPM material point is separated into dilatational and distortional components. Yield function is formulated. Lastly, the consistent conditions and different equivalent strain hardening rules are presented.

Additive decomposition of bond stretch

The initial work by Chen et al.[56] linearly estimated elastic and plastic stretches without considering the non-local effect inherently existed in LPM. In this subsection, the elastic and plastic components of bond stretch are decomposed based on non-linear relationship between stretch and interaction.

From Eq. (2.6), the value of interaction force between material point *I* and its neighbor *J*, i.e., force of bond *IJ*, under elastic deformation can be calculated using

$$f_{IJ} = k_{IJ}\delta l_{IJ} + T_I \sum_{M=1}^{N_I} \delta l_{IM} \tag{2.8}$$

where expressions for parameters k_{IJ} and T_I are given in Table 2-1 for isotropic materials.

For material points under plastic deformation, the incremental interaction for bond *IJ* can be calculated using

$$\Delta f_{IJ} = k_{IJ}^{p}\Delta\delta l_{IJ} + T_I^{p} \sum_{M=1}^{N_I} \Delta\delta l_{IM} \tag{2.9}$$

The superscript *p* of parameters k_{IJ} and T_I in above Eq. (2.9) indicates these parameters needs to be evaluated using materials plastic properties. Determination of these parameters will be discussed in Section 3.2.

The incremental stretch can be decomposed into elastic and plastic components as

$$\Delta\delta l_{IJ} = \Delta\delta l_{IJ}^{e} + \Delta\delta l_{IJ}^{p} \tag{2.10}$$

Elastic stretch $\Delta\delta l_{IJ}^{e}$ is reversible, while plastic stretch $\Delta\delta l_{IJ}^{p}$ is permanent even after unloading.

The summation of incremental stretches from all neighbors also can be decomposed into elastic part and plastic part as

$$\sum_{M=1}^{N_I}\Delta\delta l_{IM}=\sum_{M=1}^{N_I}\Delta\delta l_{IM}^{e}+\sum_{M=1}^{N_I}\Delta\delta l_{IM}^{p} \tag{2.11}$$

Due to the incompressibility of plastic deformation, the following condition must be satisfied

$$\sum_{M=1}^{N_I}\Delta\delta l_{IM}^{p}=0 \tag{2.12}$$

Therefore,

$$\sum_{M=1}^{N_I}\Delta\delta l_{IM}=\sum_{M=1}^{N_I}\Delta\delta l_{IM}^{e} \tag{2.13}$$

For material points under plastic deformation, it is assumed that the incremental interaction between these material points is the result of elastic stretch only. Thus, the increment interaction also can be expressed in terms of elastic stretch as

$$\Delta f_{IJ}=k_{IJ}^{e}\Delta\delta l_{IJ}^{e}+T_I^{e}\sum_{M=1}^{N_I}\Delta\delta l_{IM}^{e} \tag{2.14}$$

The superscript e indicates the parameters k_{IJ} and T_I are evaluated using materials elastic properties.

Equating Eq. (2.9) to Eq. (2.14), the incremental elastic stretch can be determined as

$$\Delta\delta l_{IJ}^{e}=\frac{k_{IJ}^{p}\Delta\delta l_{IJ}+(T_I^{p}-T_I^{e})\sum_{M=1}^{N_I}\Delta\delta l_{IM}}{k_{IJ}^{e}} \tag{2.15}$$

Given the incremental elastic stretch, the incremental plastic stretch is then obtained as

$$\Delta\delta l_{IJ}^{p} = \Delta\delta l_{IJ} - \Delta\delta l_{IJ}^{e} = \left(1 - \frac{k_{IJ}^{p}}{k_{IJ}^{e}}\right)\Delta\delta l_{IJ} - \frac{T_I^p - T_I^e}{k_{IJ}^{e}} \sum_{M=1}^{N_J} \Delta\delta l_{IM} \tag{2.16}$$

Incremental formulation for plastic analysis

In order to calculate the elastic bond stretch using Eq. (2.15), the model parameters k_{IJ}^{p} and T_I^p need to be determined for the corresponding plastic deformation stage. Similar to k_{IJ}^{e} and T_I^e for elastic deformation, the values of k_{IJ}^{p} and T_I^p for isotropic materials can be evaluated using the same expression given in Table 2-1 but in terms of plastic material properties for the corresponding deformation. For elastic deformation stage, the Young's modulus E^e and Poisson's ratio v^e are used to evaluate k_{IJ}^{e} and T_I^e. For plastic deformation stage, the tangent modulus E^p and Poisson's ratio v^{in} for corresponding load increment are used. The tangent modulus E^p for a given bilinear stress-strain curve is always known. The Poisson's ratio v^{in} is load increment dependent and will be determined in following content.

Under elastoplastic deformation, the effective Poisson's ratio for a specific load increment can be calculated as

$$v^{eff} = -\frac{\varepsilon_t}{\varepsilon_a} = \frac{v^e \varepsilon_a^e + v^p \varepsilon_a^p}{\varepsilon_a} \tag{2.17}$$

where ε_a and ε_t are the axial and transverse strains, ε_a^e and ε_a^p are the elastic and plastic parts of the axial strain, v^p is the plastic Poisson's ratio. Due to the incompressibility of plastic deformation, the Poisson's ratio $v^p = 0.5$.

Consider a uniaxially loaded material under plastic deformation, the incremental axial strain and transverse strain can be calculated as

$$\Delta\varepsilon_a = \frac{\Delta\sigma}{E^p} \tag{2.18}$$

$$\Delta\varepsilon_t = -\left(v^e \Delta\varepsilon_a^e + v^p \Delta\varepsilon_a^p\right) = -\left(v^e \frac{\Delta\sigma}{E^e} + v^p \left(\frac{\Delta\sigma}{E^p} - \frac{\Delta\sigma}{E^e}\right)\right) \tag{2.19}$$

where $\Delta\sigma$ is a stress increment in axial direction.

Therefore, the incremental Poisson's ratio can then be obtained as

$$v^{in} = -\frac{\Delta\varepsilon_t}{\Delta\varepsilon_a} = v^e \frac{E^p}{E^e} + v^p \frac{E^e - E^p}{E^e} \tag{2.20}$$

It can be observed from Eq. (2.17) that the effective Poisson's ratio is deformation dependent since it depends on both elastic and plastic strain components. However, the incremental Poisson's ratio is a constant for a given bilinear stress-strain curve, as can be seen from Eq. (2.20).

Non-local yield function and yield criterion

For now, the force increments within bonds connect material point *I* and its neighbors under both elastic and elastoplastic deformation can be calculated. Next, we need to determine whether a bond is under plastic deformation or not based on the deformation states of all its neighbors. For this purpose, a nonlocal maximum distortion energy criterion is developed in this section. A bond is plastic yielding if and only if when the distortion energy reaches a critical value. This yield criterion is nonlocal and the determination of yield condition for a bond is not limited to its distortion energy but also depends on the distortion energy of all bonds connected at the same material point.

For a discrete material point *I*, its energy can be decomposed into dilatational and distortional parts as

$$U_I = U_I^{dis} + U_I^{dil} \tag{2.21}$$

The distortion energy associates only with distortional deformation. Thus, using Eqs. (2.2) and (2.3), the distortion energy can be expressed as

$$U_I^{dis} = \frac{1}{2}\sum_{J=1}^{N_I} k_{IJ}(\delta l_{IJ}^{dis})^2 + \frac{1}{2}T_I\left(\sum_{J=1}^{N_I}\delta l_{IJ}^{dis}\right)^2 \tag{2.22}$$

in which δl_{IJ}^{dis} is distortional stretch and $\sum_{J=1}^{N_I}\delta l_{IJ}^{dis} = 0$ due to the fact of zero volume change under distortional deformation.

Therefore, the distortion energy can be rewritten as

$$U_I^{dis} = \frac{1}{2}\sum_{J=1}^{N_I} k_{IJ}\left(\delta l_{IJ}^{dis}\right)^2 \tag{2.23}$$

Next, we need to calculate the distortional stretch. Considering the regularity of unit cells for each material point, the dilatational deformation can be calculated in terms of average bond length change, which is the volume change. So, the dilatational stretch is given as

$$\delta l_{IJ}^{dila} = \frac{1}{N_I}\sum_{M=1}^{N_I}\delta l_{IM} \tag{2.24}$$

The distortional stretch is obtained by subtracting the dilatational stretch from the total stretch as

$$\delta l_{IJ}^{dis} = \delta l_{IJ} - \delta l_{IJ}^{dila} \tag{2.25}$$

Therefore, the incremental distortional stretch for plastic deformation can be calculated as

$$\Delta\delta l_{IJ}^{dis} = \Delta\delta l_{IJ} - \Delta\delta l_{IJ}^{dila} \tag{2.26}$$

where

$$\Delta\delta l_{IJ}^{dila} = \frac{1}{N_I}\sum_{M=1}^{N_I}\Delta\delta l_{IM} \tag{2.27}$$

Based on Eqs. (2.6) and (2.23), the incremental interaction due to incremental distortional stretch under plastic deformation can be obtained as

$$\Delta f_{IJ}^{dis} = k_{IJ}^{p}\Delta\delta l_{IJ}^{dis} \tag{2.28}$$

The total interaction due to distortional stretch is the summation of the incremental interactions at each load step as

$$f_{IJ}^{dis} = \sum \Delta f_{IJ}^{dis} \tag{2.29}$$

Identical to Eq. (2.23), the incremental distortion energy also can be calculated as the product of total distortional interaction and elastic incremental distortional stretch as

$$\Delta U_{I}^{dis} = \sum_{M=1}^{N_I}\left(f_{IM}^{dis} \times \Delta\delta l_{IM}^{dis,e}\right) \tag{2.30}$$

where $\Delta\delta l_{IM}^{dis,e}$ is the elastic part of the incremental distortional stretch calculated using Eqs. (2.15) and (2.26).

Given the incremental distortion energy at each load step, the total distortion energy is the summation as

$$U_{I}^{dis} = \sum \Delta U_{I}^{dis} \tag{2.31}$$

According to the maximum distortion energy density criterion, plastic yielding occurs when total distortion energy density reaches the critical value. Thus, the nonlocal yield function is defined as

$$Y(U^{dis}, W_{Y}^{dis}) = \frac{U^{dis}}{V} - W_{Y}^{dis} \tag{2.32}$$

where V is the volume of a material point and W_Y^{dis} is the critical distortion energy density which relates to the material yielding stress σ_Y as

$$W_Y^{dis} = \frac{\sigma_Y^2}{6\mu} \tag{2.33}$$

When $Y < 0$, all bonds associated with the material point are under elastic deformation. The plastic stretch rate for bond *IJ* is zero due to no plastic deformation.

$$\delta\dot{l}_{IJ}^{p} = 0 \tag{2.34}$$

When $Y = 0$, all the bonds associated with the material point is under plastic deformation. For a given time increment Δt, the plastic stretch rate for bond *IJ* is expressed in terms of incremental plastic stretch as

$$\delta\dot{l}_{IJ}^{p} = \frac{\Delta\delta l_{IJ}^{p}}{\Delta t} \tag{2.35}$$

where $\Delta\delta l_{IJ}^{p}$ can be calculated using Eq. (2.16).

Consistency conditions and equivalent strain hardening rules

Restricted by the Kuhn-Tucker conditions, loading-unloading conditions for the plastic deformation in LPM are described as

$$Y \le 0, \dot{\lambda} \ge 0, \dot{\lambda} Y(U^{dis}, W_Y^{dis}) = 0 \tag{2.36}$$

where λ is the plastic multiplier in the classical plasticity theory for a continuous medium, and the sign of $\dot{\lambda}$ can be informed from $\sum_M \left|\delta\dot{l}_{IM}^{p}\right|$ in LPM.

Conditions presented in Eq. (2.36) are valid for each discrete material point in LPM. However, the plastic stretch of a bond is explicitly calculated using Eq. (2.16) rather than from the plastic strain which can be determined using the plastic multiplier λ in classical plasticity

theory. But the status (yield or not) of a bond is determined by the distortion energy densities of the two end material points.

The consistency condition for LPM can be obtained by taking time derivative of the third equation in Eq. (2.36) for plastic response as

$$\dot{\lambda}\dot{Y}(U^{dis}, W_Y^{dis}) = 0 \tag{2.37}$$

Above Eq. (2.37) can be rewritten as

$$\dot{Y}(U^{dis}, W_Y^{dis}) = \frac{\dot{U}^{dis}}{V} - \dot{W}_Y^{dis} = 0 \tag{2.38}$$

Therefore,

$$\dot{W}_Y^{dis} = \frac{\dot{U}^{dis}}{V} \tag{2.39}$$

where the total distortion energy $\dot{U}^{dis}$ is a function of plastic deformation rate, $\dot{U}^{dis}(\delta\dot{l}^{p})$, and the explicit form of this function is dependent on strain hardening rules.

Above Eq. (2.39) can be rewritten in incremental form as

$$\Delta W_Y^{dis} = \frac{\Delta U^{dis}}{V} \tag{2.40}$$

For isotropic hardening, if an incremental change ΔW_Y^{dis} in tension state occurs, the same incremental change ΔW_Y^{dis} in compression state occurs correspondingly, and vice versa. So, the total elastic region expands by $2\Delta W_Y^{dis}$. For material point *I* under plastic deformation, the incremental distortion energy for isotropic hardening can be calculated as

$$\Delta U_I^{dis,iso} = \sum_{M=1}^{N_I}\left[f_{IM}^{dis} \times \left(\Delta\delta l_{IM}^{dis} - \Delta\delta l_{IM}^{dis,p}\right)\right] = \sum_{M=1}^{N_I}\left(f_{IM}^{dis} \times \Delta\delta l_{IM}^{dis,e}\right) \tag{2.41}$$

where the superscript *iso*, *p* and *e* represent isotropic hardening, plastic and elastic, respectively.

Eq. (2.41) is identical to Eq. (2.30) and shows that plastic deformation has no contribution to yield surface expansion for isotropic hardening. As an example to demonstrate the change of yield surface during plastic deformation, Figure 2-1 shows the stress-strain curve and yield surface in two dimensional isotropic hardening. As can be seen from figure 2-1, area ① represents elastic strain energy density, so the distortional part of area ① is the initial yield point. With stress changing from σ_1 to σ_2 , the distortional part of area ② and ③ indicates yield point after isotropic strain hardening, which is only related with elastic deformation. The area ② and area ③ are the same, which means the same yield surface change in tension and compression for isotropic hardening.

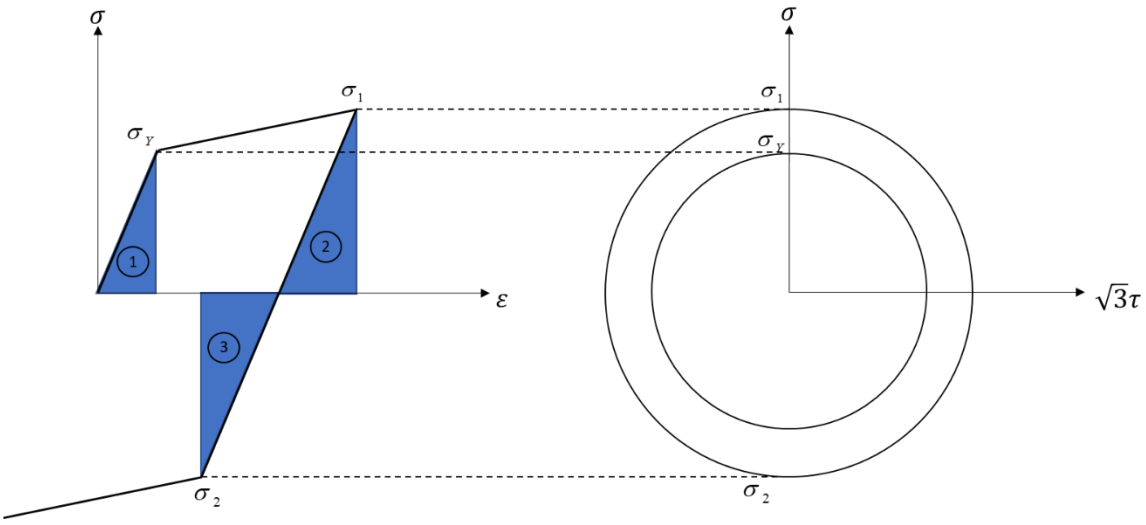

Figure 0-1 Illustration of Elastic Strain Energy Density and Yield Point Update

Substituting Eq. (2.40), the incremental yield surface for isotropic hardening is given as

$$\Delta W_Y^{iso} = \frac{\sum_{M=1}^{N_I} \left(f_{IM}^{dis} \times \Delta\delta l_{IM}^{dis,e} \right)}{V_I} \tag{2.42}$$

Isotropic hardening is widely used in monotonic loading conditions due to its simplicity. However, it is not suitable for cyclic loading conditions. Kinematic hardening is more suitable to be used for strain hardening under cyclic loading. For kinematic hardening, it is assumed that if an incremental change ΔW_Y^{dis} in tension state occurs, an incremental change $-\Delta W_Y^{dis}$ in compression state occurs correspondingly, and vice versa. But the elastic region for one cyclic loading keeps the same range. In order to capture kinematic hardening response, the counterpart concepts of back force and back stretch to the back stress in kinematic hardening in continuum mechanics are introduced in LPM.

For materials with kinematic hardening, the incremental distortion energy under plastic deformation can be expressed as

$$\Delta U_I^{dis,kin} = \sum_{M=1}^{N_I}\left[\left(f_{IM}^{dis}-\alpha_{IM}\right)\times\left(\Delta\delta l_{IM}^{dis}-\Delta\delta l_{IM}^{dis,p}-\beta_{IM}\right)\right]=\sum_{M=1}^{N_I}\left[\left(f_{IM}^{dis}-\alpha_{IM}\right)\times\left(\Delta\delta l_{IM}^{dis,e}-\beta_{IM}\right)\right] \quad (2.43)$$

where α and β are the back force and back stretch of a bond, respectively.

The total back force is the summation of incremental back force of a bond as

$$\alpha_{IM} = \sum \Delta\alpha_{IM} \quad (2.44)$$

When $Y = 0$,

$$\begin{cases}\Delta\alpha_{IM} = \Delta f_{IM}^{dis} \\ \beta_{IM} = \Delta\delta l_{IM}^{dis} - \Delta\delta l_{IM}^{dis,p}\end{cases} \quad (2.45)$$

When $Y < 0$,

$$\begin{cases}\Delta\alpha_{IM} = 0 \\ \beta_{IM} = 0\end{cases} \quad (2.46)$$

It can be observed that $\Delta\delta l_{IM}^{dis} - \Delta\delta l_{IM}^{dis,p} - \beta_{IM}$ is zero in plastic stage, so the incremental yield surface for kinematic hardening can be obtained by substituting Eq. (2.43) into Eq. (2.40) as

$$\Delta W_Y^{kin} = \frac{\sum_{M=1}^{N_I}\left[\left(f_{IM}^{dis} - \alpha_{IM}\right)\times\left(\Delta\delta l_{IM}^{dis,e} - \beta_{IM}\right)\right]}{V_I} = 0 \tag{2.47}$$

in which the yield surface range for one complete cyclic loading remains unchanged.

The mixed hardening rule combines isotropic and kinematic hardening by introducing a factor φ who range is from 0 to 1. For two extremes of φ, $\varphi = 0$ represents isotropic hardening and $\varphi = 1$ represents kinematic hardening.

The incremental distortion energy for mixed hardening is given as

$$\Delta U_I^{dis,mix} = \sum_{M=1}^{N_I}\left[\left(f_{IM}^{dis} - \varphi\alpha_{IM}\right)\times\left(\Delta\delta l_{IM}^{dis,e} - \varphi\beta_{IM}\right)\right] \tag{2.48}$$

Similarly, the incremental yield surface for mixed hardening can be obtained as

$$\Delta W_Y^{mix} = \frac{\sum_{M=1}^{N_I}\left[\left(f_{IM}^{dis} - \varphi\alpha_{IM}\right)\times\left(\Delta\delta l_{IM}^{dis,e} - \varphi\beta_{IM}\right)\right]}{V_I} \tag{2.49}$$

So far, we have derived the important ingredients including additive decomposition of stretch, incremental formulation for plastic analysis, yield function, consistency conditions and strain hardening rules of the maximum distortion energy criterion for LPM. Given all these, next section is to outline the solution algorithms for the formulated model.

2.4 Solution Algorithms

In LPM, for solution of problems under static or quasi-static loadings, the Atomic-scale Finite Element Method (AFEM)[58], [59]is used. The total energy of the discrete material

points system can be expressed as a function of position vectors of all material points in the system.

$$E_{total}(\mathbf{x}) = \sum_{I=1}^{N} U_I(\mathbf{x}_I) - \bar{\mathbf{f}}_{ext}^T \cdot \mathbf{x}_I \tag{2.50}$$

where position vector is $\mathbf{x} = (\mathbf{x}_1, \mathbf{x}_2, ..., \mathbf{x}_N)^T$, $\mathbf{x}_I$ is the coordinates of material point I and $\bar{\mathbf{f}}_{ext} = (\mathbf{f}_1, \mathbf{f}_2, ..., \mathbf{f}_N)^T$ is a external force vector.

Using Taylor expansion to expand the system total energy with respect to the initial state position vector $\mathbf{x}^{(0)}$ and apply the energy minimization condition $\partial E_{total}(\mathbf{x}) \big/ \partial \mathbf{x} = 0$, which yields

$$\mathbf{K}\mathbf{u} = \mathbf{R} \tag{2.51}$$

with

$$\mathbf{K} = \left. \frac{\partial^2 E_{total}(\mathbf{x})}{\partial \mathbf{x} \partial \mathbf{x}} \right|_{\mathbf{x}=\mathbf{x}^{(0)}} = \left. \frac{\partial^2 \sum_{I=1}^{N} U_I(\mathbf{x}_I)}{\partial \mathbf{x} \partial \mathbf{x}} \right|_{\mathbf{x}=\mathbf{x}^{(0)}} \tag{2.52}$$

$$\mathbf{R} = -\left. \frac{\partial E_{total}(\mathbf{x})}{\partial \mathbf{x}} \right|_{\mathbf{x}=\mathbf{x}^{(0)}} = \bar{\mathbf{f}}_{ext} - \left. \frac{\partial \sum_{I=1}^{N} U_I(\mathbf{x}_I)}{\partial \mathbf{x}} \right|_{\mathbf{x}=\mathbf{x}^{(0)}} \tag{2.53}$$

where $\mathbf{u}$ is the global displacement matrix and $\mathbf{u} = \mathbf{x} - \mathbf{x}^{(0)}$, $\mathbf{K}$ is the global tangent stiffness matrix and $\mathbf{R}$ is the global residual force.

For linear elastic problems, the above solution scheme can be readily applied. For nonlinear problems, incremental force method is used. During each load step, the problem is solved as linearized system. The solution of previous step is used as the initial guess for the next load

step. The elastic predictor-plastic corrector solution procedure[60]using LPM for elastoplastic problems is outlined in following content. The idea is to calculate the distortion energy at a material point by assuming elastic deformation for a load step. Then the calculated distortion energy is used to determine the material real deformation stage (elastic or plastic) using the proposed yield criterion. If the material point is under plastic deformation, model parameters k^p and T^p are then chosen for the actual deformation solution for the same load step. Otherwise, simulation proceeds to next load step.

(1) At step $[n+1]$, assuming the material is under elastic deformation, linear equations system is formulated using parameters k^{e} and T^{e}. The displacements of each discrete material point is obtained and the incremental stretch of each bond is calculated. The total stretch is the summation of previous total stretch and incremental stretch of step $[n+1]$

$$\delta l_{IJ(trial)}^{[n+1]} = \delta l_{IJ}^{[\mathrm{n}]} + \Delta\delta l_{IJ(trial)}^{[n+1]} \tag{2.54}$$

(2) Decompose the incremental bond stretch into elastic and plastic parts as

$$\Delta\delta l_{IJ(trial)}^{[n+1]} = \Delta\delta l_{IJ(trial)}^{\mathrm{e}[\mathrm{n}+1]} + \Delta\delta l_{IJ(trial)}^{p[n+1]} \tag{2.55}$$

Due to initial elastic assumption in (1), the incremental plastic stretch is zero. The elastic stretch is same as total stretch

$$\Delta\delta l_{IJ(trial)}^{e[n+1]} = \Delta\delta l_{IJ(trial)}^{[n+1]} \tag{2.56}$$

(3) The elastic incremental distortional stretch can be calculated as

$$\Delta\delta l_{IJ(trial)}^{dis,e[n+1]} = \Delta\delta l_{IJ(trial)}^{dis,e[n+1]} - \frac{1}{N_I}\sum_{M=1}^{N_I}\Delta\delta l_{IM(trial)}^{e[n+1]} \tag{2.57}$$

(4) The incremental interaction due to incremental distortional stretch can be calculated as

$$\Delta f_{IJ(trial)}^{dis[n+1]} = k_{IJ}^{e} \Delta\delta l_{IJ(trial)}^{dis[n+1]} \tag{2.58}$$

(5) The incremental distortional potential energy can be calculated as

$$\Delta U_{I(trial)}^{dis[n+1]} = \sum_{M=1}^{N_I} \left[\left(f_{IM(trial)}^{dis[n+1]} - \varphi\alpha_{IM}^{[n+1]} \right) \times \left(\Delta\delta l_{IM(trial)}^{dis,e[n+1]} - \varphi\beta_{IM}^{[n+1]} \right) \right] \tag{2.59}$$

where back force $\alpha_{IM}^{[n+1]}$ and back stretch $\beta_{IM}^{[n+1]}$ is zero for assumed elastic deformation. φ is dependent on hardening rule and is a given material parameter.

(6) The total distortion energy can be calculated as

$$U_{I(trial)}^{dis[n+1]} = U_{I}^{dis[n]} + \Delta U_{I(trial)}^{dis[n+1]} \tag{2.60}$$

And the status of yield function can be determined using

$$Y_{(trial)}^{[n+1]} = \frac{U_{I(trial)}^{dis[n+1]}}{V_I} - W_Y^{dis[n]} \tag{2.61}$$

(7) If $Y_{(trial)}^{[n+1]} \le 0$, the initial elastic deformation assumption is correct and update the state variables using the trial values, $\Delta\delta l_{IJ}^{e[n+1]} = \Delta\delta l_{IJ(trial)}^{e[n+1]}$, $U_I^{dis[n+1]} = U_{I(trial)}^{dis[n+1]}$, and $W_Y^{dis[n+1]} = W_Y^{dis[n]}$, and then go to (9). If $Y_{(trial)}^{[n+1]} > 0$, parameters k^p and T^p are in (1) to determine the displacement solution. All values corresponding to plastic deformation are nonzeros.

(8) Update yield surface as

$$\Delta W_Y^{dis[n+1]} = \frac{\Delta U_I^{dis[n+1]}}{V_I} \tag{2.62}$$

and

$$W_Y^{dis[n+1]} = W_Y^{dis[n]} + \Delta W_Y^{dis[n+1]} \tag{2.63}$$

(9) Go on next load step.

2.5 Numerical Examples

Several benchmark elastoplastic problems are investigated using the proposed nonlocal maximum distortion energy criterion in LPM. To verify the proposed yield criterion, LPM predictions are compared with theoretical and ABAQUS solutions. The first example studies the stress-strain curve prediction accuracy under tensile and cyclic yielding. The second example checks the yielding surface with von Mises yielding surface for biaxial loading. The last example verifies the prediction accuracy of both deformation and plastic zone for a localized yielding case. Specimens in all these examples are loaded slowly such that quasi-static assumption is valid.

Bilinear constitutive material model is used in this section, which can be characterized using following material properties: Young's modulus $E = 146$ GPa, Poisson's ratio $\nu = 0.3$, hardening modulus $K = 30.6$ GPa, and yield stress $\sigma_Y = 200$ MPa. For all the examples in this section, the simple cubic lattice structure is used to discretize the solution domain with material point diameter of 0.0001 m. It should be noted that the stress and strain presented in this section for LPM are converted from corresponding force and displacement for comparison purpose.

Three-dimensional beam under tensile tests

In this example, a vertically positioned three-dimensional beam that has dimension of 0.01 m x 0.01 m cross section and 0.03 m height is studied under two yielding cases: tensile yielding and cyclic yielding with different strain hardening. The top face of the beam is fixed in the

vertical z- direction while the bottom face is applied with downward uniform distributed loads. The left and back faces are fixed in the y- and x- directions, respectively.

Case I: Tensile yielding

Two loading scenarios are considered in this case, see Figure 2-2. The first loading scenario is to monotonically load the specimen to 300 MPa. For this loading, material starts to yield when the applied load reaches 200 MPa and yielding continues as the load increases. The second loading scenario is to firstly load the specimen to 250 MPa, then unload to 150 MPa, and reload to 300 MPa. For this loading, during the first loading phase, material yielding occurs at the stress level of 200 MPa and continues to yield before unloading starts at 250 MPa. Elastic unloading occurs during decreasing of stress level from 250 MPa to 150 MPa. During the reloading from 150 MPa to 300 MPa, materials yielding occurs at the new yielding stress of 250 MPa which is the starting point of previous unloading. Since the specimen doesn't undergo reverse compressive yielding, strain hardening doesn't play a role in these cases.

Comparison of predicted stress-strain curves with theoretical curves for both loading scenarios are shown in Figure 2-2. As can be seen, for both loading scenarios, the predicted stress-strain curves in the axial direction and the history of transverse strains agree very well with their theoretical values, respectively. A slight delay in the occurrence of unloading in LPM. This is possibly due to the implementation of the elastic predictor-plastic corrector solution scheme for LPM, since no cut in load step size was used by assuming the pre-assigned uniform load step size is already small enough. Overall, LPM can accurately reproduce the theoretical results in both axial and transverse directions under both tensile yielding scenarios for elastoplastic materials. Thus, the proposed nonlocal maximum distortion energy criterion is valid.

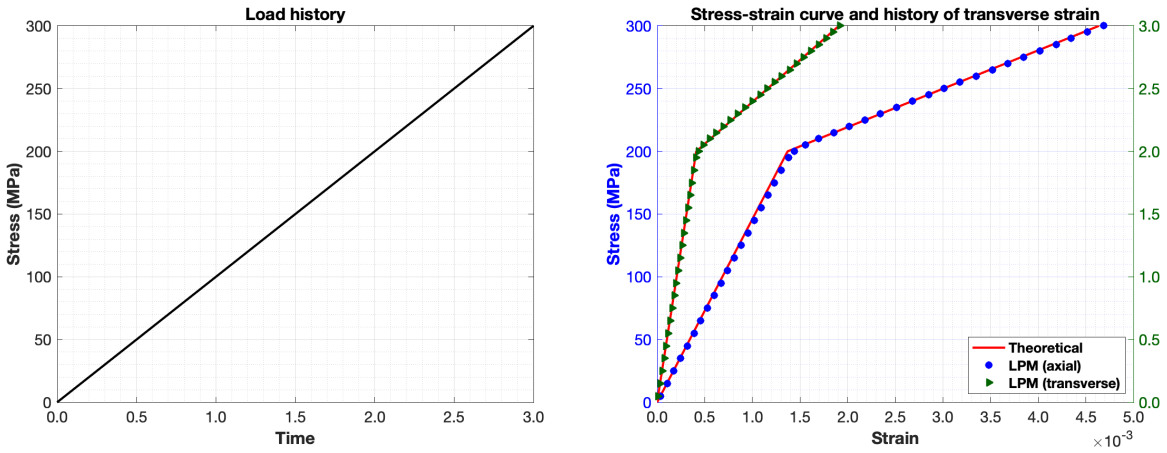

under monotonic loading

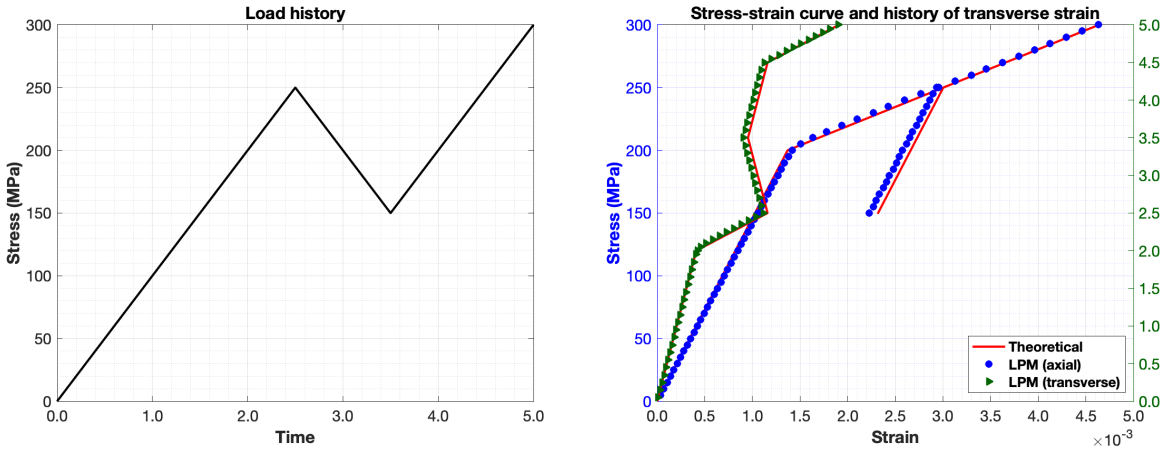

under load-unload-reload loading

Figure 0-2. Loads History and Comparison of Axial Stress-strain Curve and Transverse Strain for 3D Beam

Case II: Cyclic yielding

The same specimen as for *Case I* is subjected to cyclic loading is studied in this example to verify the developed equivalent strain hardening rules, i.e., isotropic hardening, kinematic hardening and mixed isotropic-kinematic hardening. For mixed hardening case, different values of the factor φ are used.

The load history and comparison of stress-strain curves for the case of isotropic hardening are shown in Figure 2-3. For materials of isotropic hardening under the given load, yielding occurs

at the stress level of 200MPa and continues until the commence of unloading. The yield stress is reset to the value of 250 MPa, which is the start point of unloading. Elastic unloading continues up to stress level of -250 MPa. Continuing reverse loading beyond -250 MPa renders the reverse yielding of the specimen. A new yield stress of 300 MPa is reset and specimen is elastically loaded from -350 MPa to 350 MPa. Plastic yielding occurs again at the stress level of 350 MPa and beyond. From the comparison, the proposed equivalent isotropic strain hardening rule can accurately capture the material's isotropic hardening response, i.e., yield surface dilatation, under cyclic loading. Small discrepancies at the turning points may results from the constant load step size.

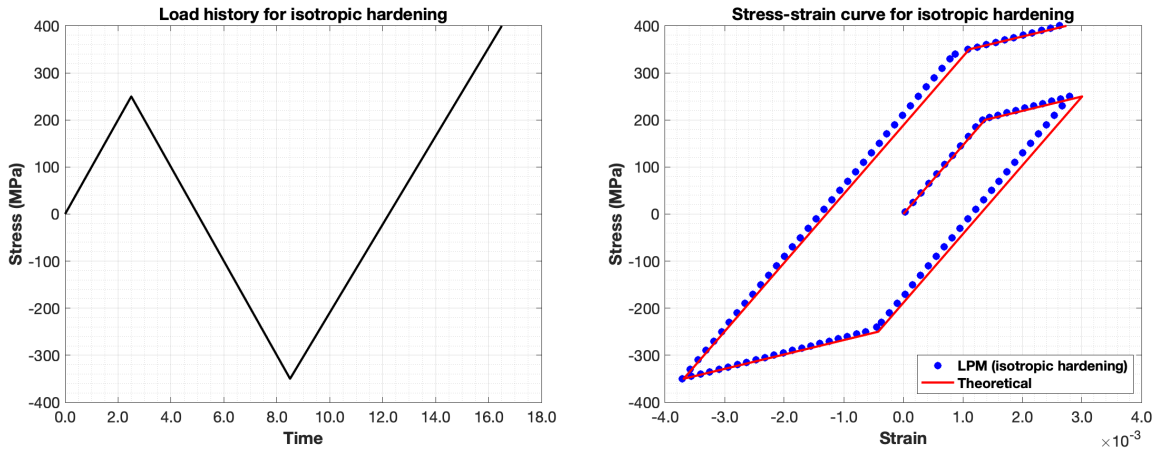

Figure 0-3. Load History and Comparison of Stress-strain Curve for Isotropic Hardening

The load history and comparison of stress-strain curves for the case of kinematic hardening are shown in Figure 2-4. Different from isotropic hardening, kinematic hardening resets the yield stress while keep the range between tensile yield stress and immediate compressive yield stress the same, i.e., yield surface translation, during cyclic loading. In this case, the yield stress initially was (200 MPa, 200 MPa) and reset to (250 MPa, -150 MPa) and (-250 MPa, 150 MPa) during the subsequent loading. From the comparison, the proposed equivalent kinematic strain

hardening rule can accurately capture the material's kinematic hardening response under cyclic loading.

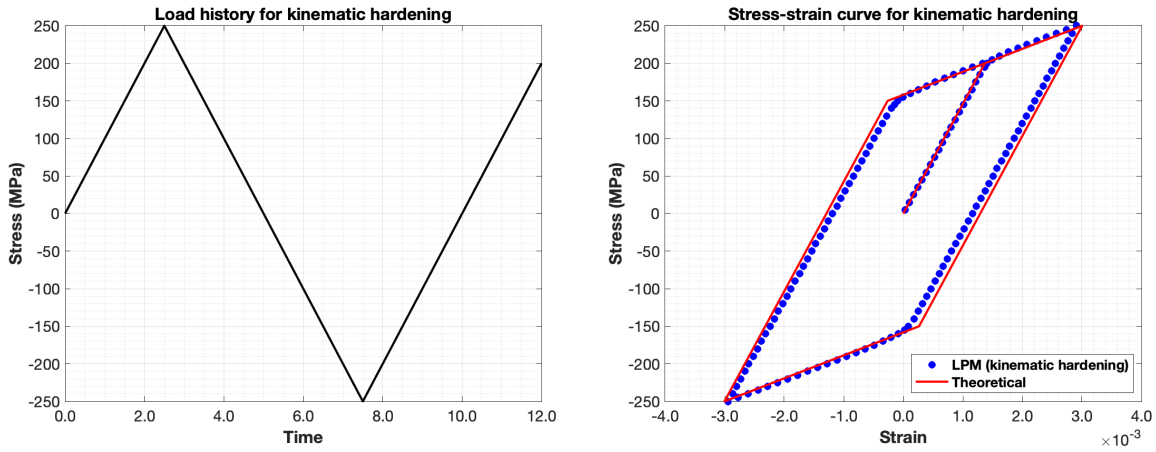

Figure 0-4. Load History and Comparison of Stress-strain Curve for Kinematic Hardening

The load history and comparison of stress-strain curves for the case of mixed isotropic-kinematic hardening are shown in Figure 2-5. Three values of factor φ, i.e., 0.2, 0.5 and 0.8, are investigated in this study. If φ is small, the material response is close to isotropic hardening. In contract, if φ is large, the material response is close to kinematic hardening. As expected for the simulation results, after one loading cycle, the case of $\varphi = 0.2$ has the largest elastic region and $\varphi = 0.8$ has the smallest elastic region. This further confirms the validity and accuracy of the proposed nonlocal yield criterion and equivalent strain hardening rules for LPM.

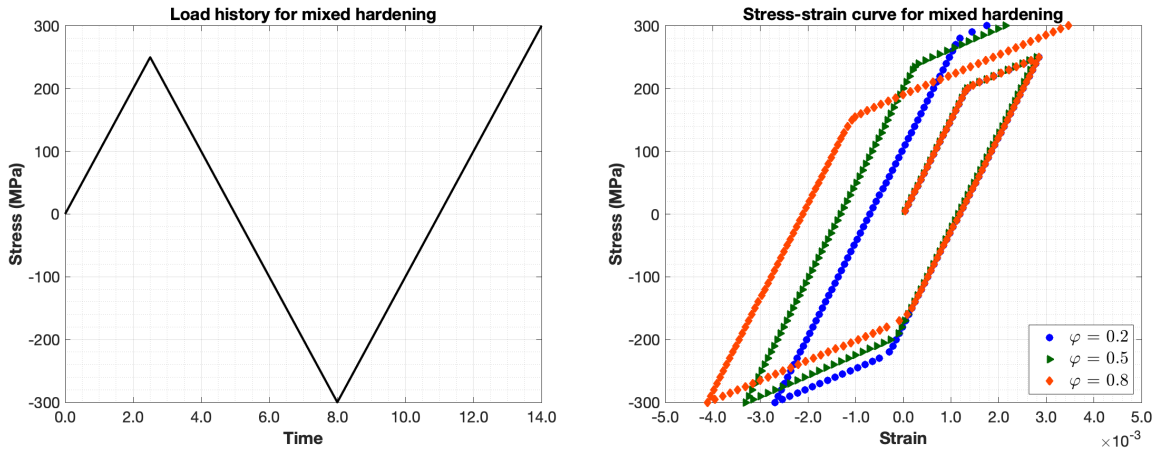

Figure 0-5. Load History and Comparison of Stress-strain Curve for Mixed Hardening

Based on above verification studies in this example, it can be observed that the proposed yield criterion for LPM can be used to successfully predict elastoplastic deformation under loading, unloading and cyclic loading for different strain hardening rules.

Three-dimensional cube under biaxial tensile test

In this example, the two-dimensional yield surface of the proposed nonlocal maximum distortion energy criterion was verified against von Mises yield surface. A three-dimensional cube of edge length 0.01 m is used in this example. The cube is constrained such that a biaxial tensile test is mimicked in the y and z directions. The left and top faces are fixed in the y and z directions, respectively. The center point of the top-left edge is fixed in all three directions. Uniformly distributed tensile loadings are applied on the right and bottom faces in the positive y and negative z directions, respectively.

Multiple simulations are performed with different combinations of the y-direction load σ_{yy} and the z-direction load σ_{zz}. Stress states were plotted based on the two principle directions. A comparison of LPM yield surface against von Mises yield surface is shown in Figure 2-6. As expected, the predicted different loading combinations using the formulated yield criterion

scatter slightly around the von Mises surface. This further verifies the formulated nonlocal maximum distortion energy yield criterion for modeling plastic deformation using LPM.

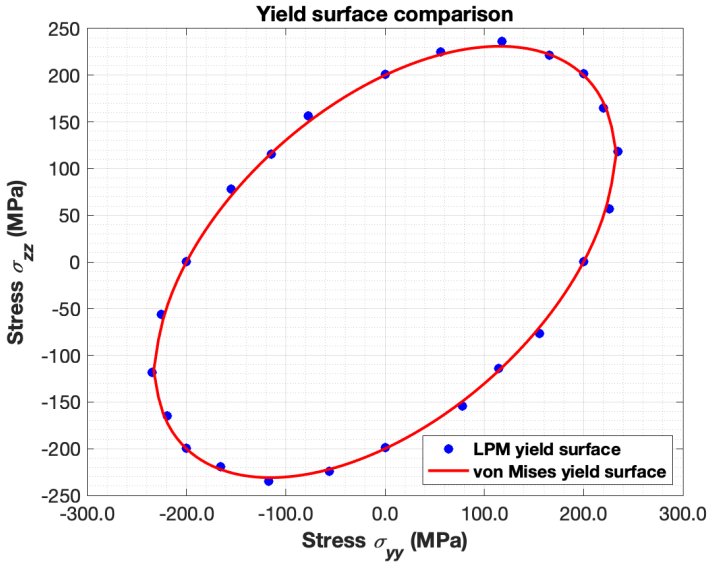

Figure 0-6. Comparison of LPM Yield Surface with von Mises Yield Surface under Biaxial Loading

Three-dimensional beam with a hole under loading and unloading tests

A three-dimensional beam which has the same dimension as the one used in example 5.1 but with a through-thickness hole of diameter 0.004 m at the center of front face is tested in this example. The top face of the beam is fully clamped, and a uniformly distributed load is applied on the bottom face in the downward direction. The beam was firstly loaded to 150 MPa, then unloaded to 0 MPa and reversely loaded to -150 MPa. Both isotropic and kinematic strain hardenings were studied. Model predictions are compared with finite element method (FEM) solutions from ABAQUS using C3D8 linear brick element with reduced integration with hourglass control[61], i.e., C3D8R element.

Comparisons of the distributions of y- displacement at three load levels, i.e., 100 MPa, 125 MPa and 150 MPa, during the loading stage are shown in Figure 2-7. It should be noted that since the specimen is under loading up to 150 MPa, both strain hardenings yield the same prediction results. For easiness of comparison, all the LPM results are colored based on the legend for the 150 MPa case, and the same for FEM results. As can be seen from the displacement plots, the hole introduces deformation localization in the specimen. And this localized deformation continues to develop with the increase of applied load. Small discrepancy in terms of deformation are observed between LPM prediction and FEM result. One source for this difference is the surface effect[57] in LPM due to incomplete neighbors for material points near the surfaces. Increasing number of material points for discretization will mitigate the surface effect and reduce the difference.

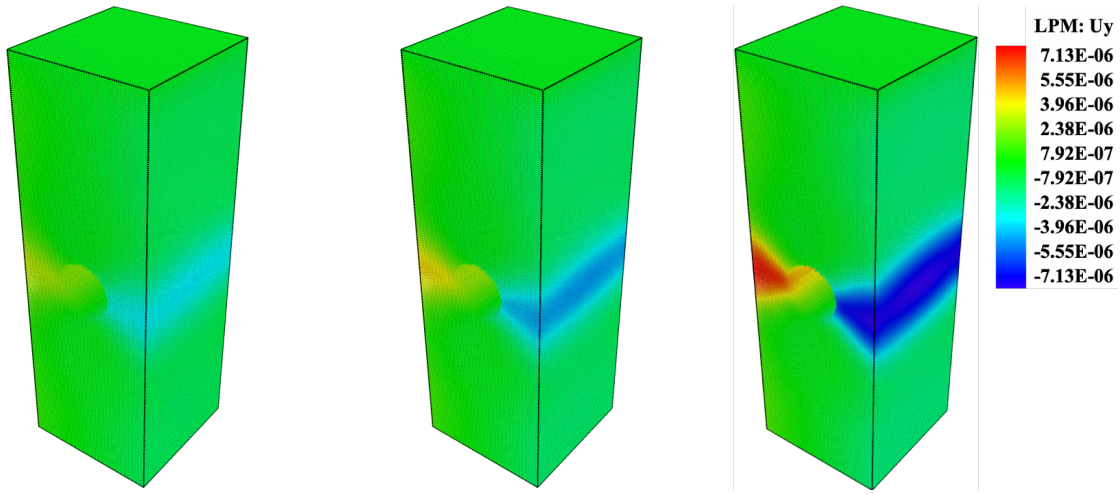

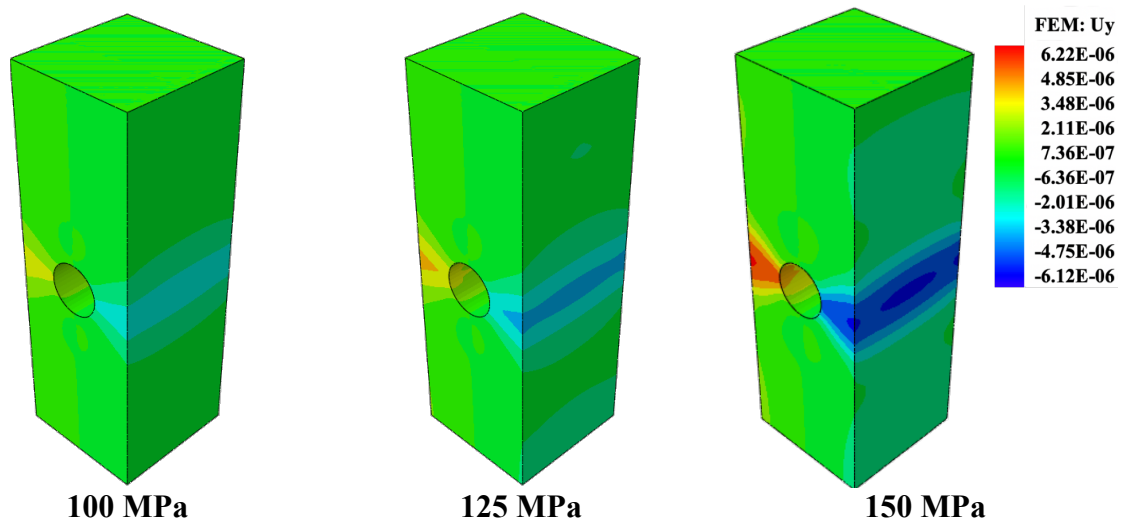

Figure 0-7. Comparison of Displacement Uy Distributions (One Legend for all LPM Results and the Other One for All FEM Results)

Comparisons of the plastic zone distributions at the same load levels are shown in Figure 2-8. As can be seen, the specimen undergoes considerable plastic deformation during the initial loading phase. Due to localization, plastic deformation initiates at the hole boundary in the direction perpendicular to the loading. With the increase of load, larger plastic deformation develops and expands the plastic zone around the hole. The butterfly shape plastic zone around the hole at the stress level of 150 MPa has been observed in both LPM and FEM models. Due to the fully clamped boundary condition, corner and edge areas of the top face deforms plastically. For regions around the hole geometry, the difference between results from LPM and FEM are very subtle. Due to aforementioned skin effect in LPM, regions near the edges of the top face have small amount of plastic deformation.

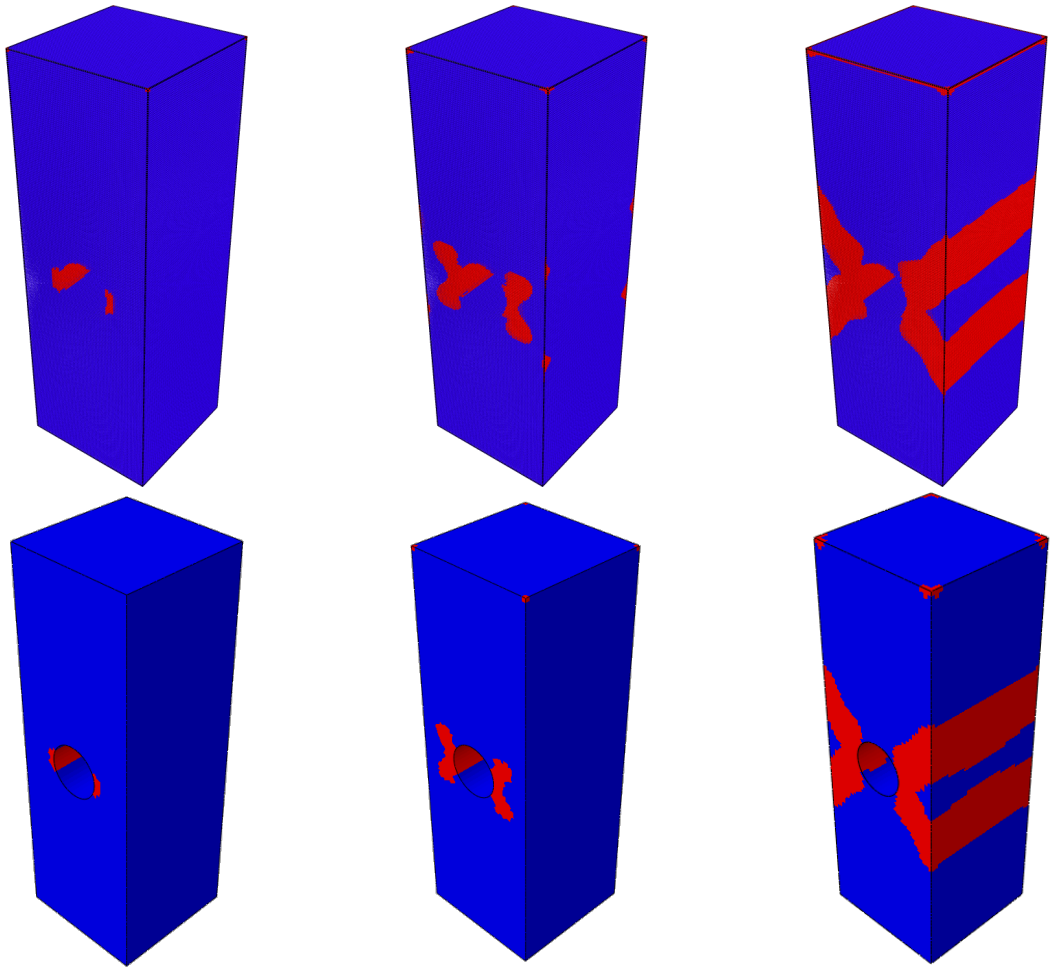

Figure 0-8. Comparison of Plastic zone Distributions (Top Row: LPM, Bottom Row: FEM; Red Color: Plastic Zone, Blue Color: Elastic Zone)

The force-displacement curves for the complete load history of both strain hardening rules are shown in Figure 2-9. As can be seen, the LPM curves match very well with FEM curves. Small difference exists after reverse yielding for the case of kinematic hardening.

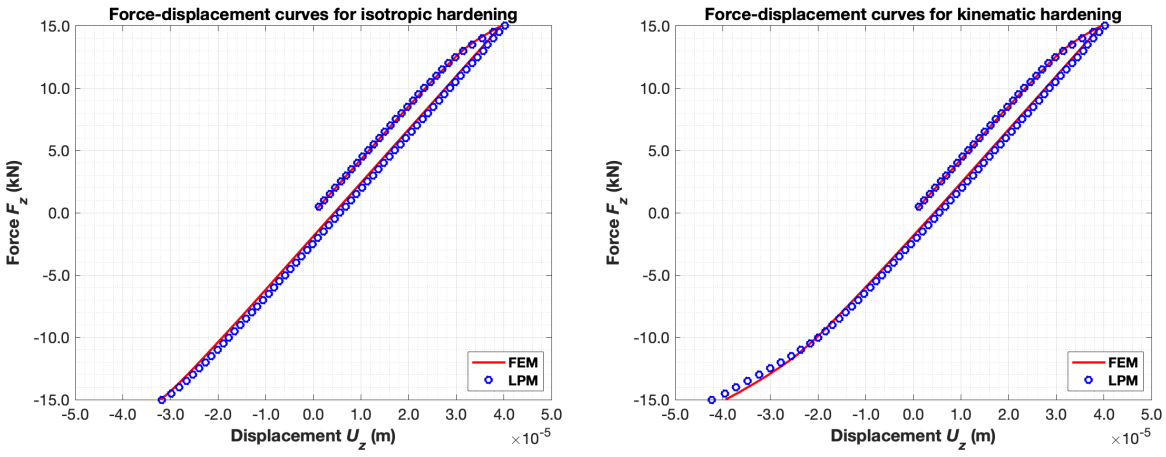

Figure 0-9. Comparison of Force-displacement Curve for Isotropic and Kinematic Hardenings

The deformed shapes of the center hole are plotted for different stress levels and compared with the initial shape. With current discretization, there are total 32 material points representing the boundary of the hole. Deformed positions of these material points are plotted by magnifying their displacements by 50 times. Figure 2-10 shows the comparison of the initial hole shape and shapes at loading to 150 MPa and unloading to 0 MPa with isotropic hardening. Among these hole shapes, the shape of loading to 150 MPa captures the elastoplastic deformation of the hole, and the shape of unloading to 0 MPa represents the residual plastic deformation of the hole. The stretch of the hole in the loading direction and compression in the other direction can be obviously observed in the plots.

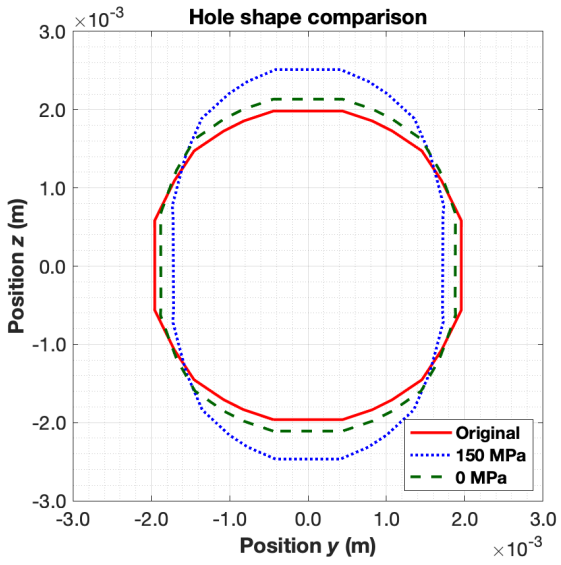

Figure 0-10. Comparison of Hole Shapes under Elastoplastic Deformation

A comparison of the hole shapes between isotropic hardening and kinematic hardening under reverse loading to -150 MPa is presented in Figure 2-11. The initial undeformed shape is also provided. As expected, the hole is compressed in the compression direction while expanded in the other direction, and kinematic hardening case has larger deformation than isotropic case because of the low reverse yield stress after initial tensile yielding.

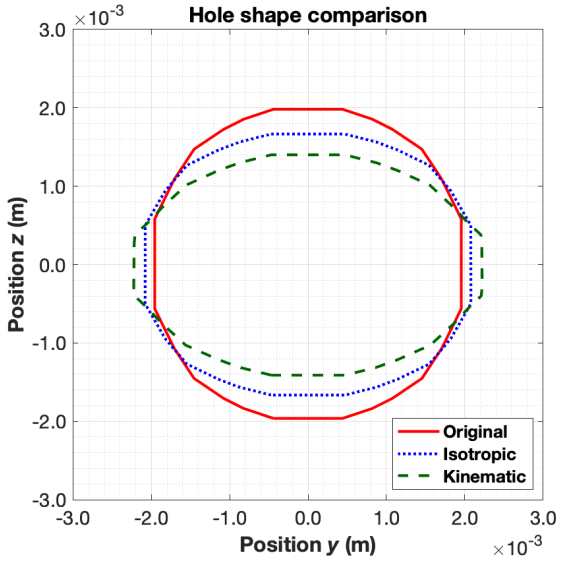

Figure 0-11. Comparison of Hole Shapes between Isotropic Hardening and Kinematic Hardening

2.6 Discussion and Conclusions

Lattice Particle Model (LPM) is a discontinuous nonlocal reformulation of classical solid mechanics using integro-differential governing equations rather than partial differential equations. Hence, LPM is more beneficial for mechanics problems involving spatial discontinuities such as crack and interface. LPM has been successfully applied to elastic/brittle materials without limit of Poisson's ratio. Initial attempt has been made by the coauthors to formulate a local bond-based critical stretch yielding criterion for LPM. However, the determination of the critical stretch is an ad-hoc, and the deformation isotropy is not guaranteed for homogeneous isotropic materials.

In this paper, following the basic idea of its formulation in classical continuum mechanics, a maximum distortion energy criterion was formulated for LPM. Important ingredients for this nonlocal yield criterion including additive decomposition of bond stretch, incremental formulation of LPM for plastic analysis, nonlocal yield function, consistency conditions and equivalent strain hardening rules were developed. An implicit solution scheme for static or quasi-static elastoplastic problems using the developed yield criterion in LPM was outlined. Several benchmark problems including monotonic tensile yielding and cyclic yielding with isotropic, kinematic and mixed strain hardenings were tested and model predictions were compared against theoretical and numerical solutions. From the comparison, the developed nonlocal maximum distortion energy criterion is valid and can yields accurate results for elastoplastic materials. In addition, following conclusions can be made:

(1) For homogeneous isotropic materials, the deformation isotropy is guaranteed in the proposed model. In the proposed model, all bonds associated with one material point change parameters from elastic stage to plastic stage when its distortion energy density reaches the critical value, which keeps isotropy of the model.

(2) The example studied in this work was based on simple cubic packing. For other 3D lattice packings, the developed model can be readily applied.

Future work is to apply the developed scheme to model fracture of ductile materials and extend the proposed formulation to anisotropic ductile materials.

3. MULTIAXIAL FATIGUE MODEL FOR RANDOM SPECTRUM LOADINGS

A multiaxial fatigue life prediction model under general multiaxial random loadings is proposed in this paper. First, a brief review for existing multiaxial fatigue models is given with a special focus is on the Liu- Mahadevan critical plane concept, which can be applied to both brittle and ductile materials. Next, the new model development based on the Liu-Mahadevan critical plane concept for random loading is presented. The key concept is to use two-steps to identify the critical plane: identify the maximum damage plane due to normal stress and calculate the critical plane orientation with respect to the maximum damage plane due to normal stress. Multiaxial rain-flow cycle counting method with mean stress correction is used to estimate the damage on the critical plane. Equivalent stress transformation is proposed to convert the multiaxial random load spectrum to an equivalent constant amplitude spectrum. The equivalent stress is then used for fatigue life predictions. The proposed model is validated with both literature and in-house testing data generated using an Al 7075-T6 alloy under various random uniaxial and multiaxial spectrums. Comparison between experimental and predicted fatigue life lives showed good agreements; thus, demonstrating efficacy of the proposed model. Finally, concluding remarks and future work based on the results obtained are discussed.

3.1 Introduction

Multiaxial fatigue models can be classified into four major categories: stress-based [11], [12], [62], strain-based [13], [14], energy-based [15], [16], and fracture mechanics-based approaches [17]. Employed under any of these categories, there is a criterion that offers a physical interpretation of the fatigue damage by relating the crack orientation (initiation and propagation) to a plane of critical loading, known as the “critical plane approach”.

The basic concept of the critical plane approach is to use the stress/strain components on a plane to calculate the fatigue damage of material under general multiaxial cyclic loadings. Many models assume the maximum shear stress plane as the critical plane, which is suitable for ductile failure [18], [19]. Other models assume that the maximum normal stress range plane as the critical plane which is mostly suitable for brittle failure[21]–[23]. However, when these two failure modes mix, or the material is neither ductile nor brittle, it is difficult to select an appropriate model. Furthermore, material's failure mode can also change with respect to the the fatigue life regime (i.e. low-cycle or high-cycle) [24]. Several attempts trying to solve this issue have been proposed in the past. One successful approach is to let the critical plane change its orientation for different failure modes, i.e., along the maximum normal stress range plane for brittle materials and along the maximum shear stress range plane for ductile materials. The concept was initially proposed using an empirical function [25], [26], [63].

Liu and Mahadevan [28], [29] proposed an analytical solution for the critical plane orientation based on the material ductility, known as Liu-Mahadevan critical plane concept. The concept was first applied using the stress-based approach for high-cycle fatigue [28] and was later extended for low-cycle fatigue using a strain-based model [29]. Extensive model validations for this concept have been performed for both brittle and ductile materials at the material and component level. However, since only the strain terms are used in the model [29], it cannot include the out-of-phase hardening behaviour explicitly. Out-of-phase loading causes rotation of the direction of the principal stresses. The rotation brings additional hardening to the material due to the activation of more slip planes compared to other types of loading. Thus, the rotation causes an increase in stress response and thus reduces the fatigue life. In order to compensate for out-of-phase hardening some empirical parameters are used [29], [64].

Calibration of these parameters requires several out-of-phase multiaxial fatigue tests. Recently, Wei and Liu [30] proposed an energy-based model integrating the Liu-Mahadevan critical plane concept. The energy-based model can be applied to a wide range of materials (both brittle and ductile) under both proportional and non-proportional loadings without the need of calibration parameters. This is because that both stress and strain terms are used in the energy-based criteria and the out-of-phase hardening effect is automatically included. Only constant amplitude loading is considered in [30]. In this paper, the Liu-Mahadevan critical plane concept is extended for random fatigue loading.

The main new development will consider the damage accumulation under general random multiaxial loadings in the Liu-Mahadevan model framework. Many existing fatigue criteria for random loading are either in time domain [65] or frequency domain [66]. Usually, time domain approaches are based on a cycle counting method and a cumulative damage rule. Rainflow cycle counting method is widely used for analysis and simplification of random fatigue load paths. Amongst other cycle counting models proposed, a new cycle counting procedure for normal stress on critical plane model was introduced by Carpinteri et al. [67]. Across all the fatigue damage accumulation rules, the linear damage accumulation rule (LDR), also known as Miner's rule, is probably the most commonly used due to simplicity [68]. For critical plane-based multiaxial fatigue model, enumeration of all possible plane orientation is usually used for damage evaluation. The maximum damage along a certain plane is identified. This is certainly possible, but usually very time consuming as exhaust search is required. In addition, cycle counting for both normal and shear stress may be required. In the current study, the authors attempt to develop a multiaxial fatigue model for random loading by integrating the Liu-Mahadevan critical plane approach along with Rainflow counting and Miner's damage

rule. For computational efficiency, a maximum damage plane is estimated first, and an equivalent stress transformation is proposed to determine fatigue life.

The remaining of the paper is organized as follows. First, a brief review of the Liu-Mahadevan model concept is given. Extension from constant amplitude loading to random spectrum loading is done by replacing the maximum normal stress amplitude plane with a maximum normal damage plane. Derivation of this maximum damage plane is discussed in detail. Next, an equivalent constant stress transformation of the random multiaxial spectrum loading is proposed for the fatigue life prediction. Following this, both literature data and in-house testing data are used to validate the proposed methodology. Finally, discussion and conclusions are provided based on the proposed method.

3.2 Brief Review of Liu-Mahadevan Model under Constant Amplitude Loading

The Liu-Mahadevan critical plane approach for stress-based fatigue life prediction under constant multiaxial loading condition[28] is given in Eq. (3.1),

$$\sqrt{\left(\frac{\sigma_{a,c}}{f_{-1}}\right)^2+\left(\frac{\tau_{a,c}}{t_{-1}}\right)^2+k\left(\frac{\sigma_{a,c}^{H}}{f_{-1}}\right)^2}=\beta \tag{3.1}$$

where $\sigma_{a,c}$, $\tau_{a,c}$, $\sigma_{a,c}^{H}$ are the normal, shear, and hydrostatic stress amplitudes acting on the critical plane, respectively. f_{-1} and t_{-1} are uniaxial and torsional fatigue stress limits for fully-reversed constant amplitude loading, respectively. Parameters k and β are material constants determined from uniaxial and pure torsional fully-reversed tests. Eq. (3.1) represents the summation of the damage caused by normal, shear and hydrostatic stress components. Most of critical plane approaches assume that the critical plane only depends on the stress state, which indicates that such models account the fatigue damage accumulation in the same way for different materials under the same stress state. Their applicability generally depends on the

material's properties. However, in the Liu-Mahadevan critical plane concept, the critical plane does not only depend on the stress state but also on the material properties. The critical plane is theoretically determined by minimizing the damage introduced by the hydrostatic stress amplitude, which has almost no applicability limitations with respect to different metals. The key concept to achieve this wide applicability of the model is to let the critical plane rotates with respect to the material ductility. A schematic illustration is shown in Figure 3-1. The critical plane has angle of α with respect the maximum normal stress plane. The angle α is zero for brittle materials and is 45 degrees for ductile materials. Instead of empirically interpolating the angle α between these two extremes, an analytical solution is obtained (see details in[28]). The results for model parameters are shown in Table 3-1 [28].

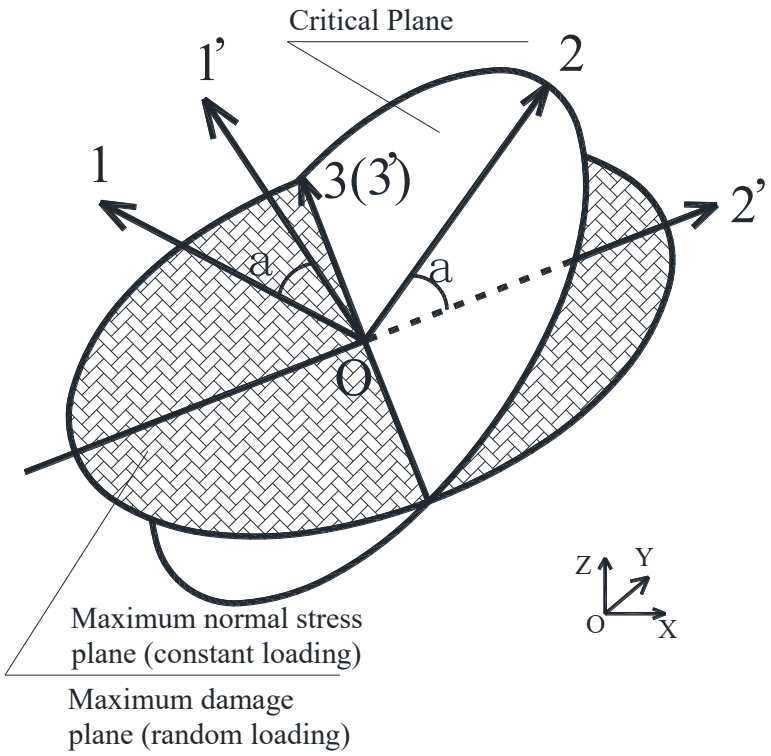

Figure 0-12 Orientation of Maximum Damage Plane and Critical Plane

Table 0-2 Liu-Mahadevan Material Parameters

Material property	$s = \frac{t_{-1}}{f_{-1}} \le 1$	$s = \frac{t_{-1}}{f_{-1}} > 1$
α	$\cos(2\alpha) = \frac{-2+\sqrt{4-4\times(1/s^2-3)\times(5-1/s^2-4s^2}}{2\times(5-1/s^2-4s^2)}$	$\alpha = 0^\circ$
k	$k = 0$	$k = 9[(\frac{t_{-1}}{f_{-1}})^2 - 1]$
β	$\beta = \sqrt{\cos^2(2\alpha)s^2 + \sin^2(2\alpha)}$	$\beta = 1$

The Liu-Mahadevan fatigue prediction model under constant loading has been validated by different materials with a wide range of ductility, from extremely brittle steels to ductile steels [28].

3.3 Proposed Model for Arbitrary Random Loading

The above discussion and review are only for constant amplitude loading. It should be noted that the relationship of critical plane with maximum normal stress amplitude plane is no longer valid under random loading as the final fracture plane may not be the same as the maximum stress amplitude plane. Now the question is: how to define the critical plane under general random loadings?

The definitions of the fatigue fracture plane and the critical plane should be clarified first before determining the critical plane orientation. In the fatigue model under constant amplitude loading proposed by Liu and Mahadevan [28], [29], the fatigue fracture plane refers to the crack plane observed at the macro level. The critical plane is not an actual crack plane. It is a

material plane on which the fatigue damage is evaluated. The two planes may or may not coincide with each other. The fatigue fracture plane is assumed to be the plane, which experiences the maximum normal stress amplitude. The critical plane orientation may differ from the fatigue fracture plane for different materials, which is depended on material ductility.

In the proposed model, it is assumed that, under variable loading condition, the fatigue fracture plane is the maximum damage plane, and damage occurs due to the normal stress amplitude acting on the plane. Normal stress spectrum on all possible orientations is computed and then the plane with maximum damage due to normal stress amplitude is found using the rainflow counting algorithm and Miner's rule. Next, the proposed study will replace the maximum normal stress amplitude plane (under constant amplitude loading) with the maximum normal damage plane (in general random loading) for all calculation steps in section 2.1. It is noted that the maximum normal damage plane definition is the same as the maximum normal stress amplitude plane under constant amplitude loading cases. Thus, the proposed extension can be considered as generalization of the Liu-Mahadevan model concept. The maximum damage plane under random loading (the same maximum normal stress plane under constant amplitude loading) and the critical plane are shown in Figure 1.

For the proposed fatigue model under variable loading, all parameters from material properties keep the same value as those under constant amplitude loadings (i.e., Table 3-1). However, the formula of the fatigue model under constant loading cannot be directly applied, because under a variable amplitude loading the stress components on the critical plane are not constant. There are two approaches to solve this issue. One is to calculate the cumulative fatigue damage cycle-by-cycle, which could be time consuming, specifically for random high cycle fatigue loading. The other one is to transfer a variable loading condition to an equivalent

constant loading condition, then the equivalent stress components will be used following the same procedure in [28]. The detailed procedure for computing the equivalent stress on the critical plane is shown below.

First, fatigue damage of normal stress D_c^{σ} and shear stress D_c^{τ} on the critical plane can be computed using Miner's rule and rainflow accounting algorithm as presented in Eq. (3.2):

$$\begin{cases} D_c^{\sigma} = \sum_{i=1}^{N_{\sigma}} \frac{1}{f\left(\sigma_{a,c}^{i}\right)} \\ D_c^{\tau} = \sum_{i=1}^{N_{\tau}} \frac{1}{f\left(\tau_{a,c}^{i}\right)} \end{cases} \tag{3.2}$$

where N_{σ} and N_{τ} are number of cycles of normal and shear stress spectrum on critical plane based on rainflow counting algorithm, respectively. The term $f(\sigma)$ is the fatigue life function of the normal or shear stress on the critical plane, which computes the number of cycles under a given loading case σ. It should be noticed that the fatigue life function is fitted by uniaxial and pure torsional S-N curves. For example, $f(\sigma)$ could be in power form (Basquin's model) given by Eq. (3.3).

$$f(\sigma)=\mathrm{A}\times\sigma^{B} \tag{3.3}$$

Thus, the term $\frac{1}{f(\sigma^{i})}$ is the fatigue damage in the i$^{\text{th}}$ cycle of normal or shear loading. Eq. (3.2) represents a summation of the fatigue damage of a random spectrum with zero mean stress.

Next, the mean stress effect of arbitrary random spectrum is included. It is well known that the mean normal stress has an important effect on fatigue life. Generally, tensile mean stress reduces the fatigue life, while compressive mean stresses are said to increase fatigue life or considered to be neutral. Under constant amplitude loading conditions, the mean stress value

is defined as the algebraic mean of the maximum and minimum stress value in one cycle. For the random loading, mean stress is determined by the average of normal stress spectrum on the maximum damage plane at i[th] cycle [69], [70], presented in the integral form in Eq. (3.4):

$$\sigma_m^i = \frac{\int \sigma_D^i(t)dt}{t^i} \tag{3.4}$$

Mean stress is introduced into the fatigue model with a correction factor $(1+\eta\frac{\sigma_m}{\sigma_y})$, where η is material coefficient, which can be obtained from uniaxial fatigue test with the same mean stress ratio, and σ_y is the yield stress. It should be noticed that σ_m is defined as acting on the maximum damage plane. Thus, the damage of normal and shear stress on the critical plane can be calculated using Miner's rule based on the rainflow accounting algorithm, given in Eq. (3.5) as:

$$\begin{cases} D_c^\sigma = \sum_{i=1}^{N_\sigma} \dfrac{1}{f\left[(1+\eta\frac{\sigma_m{}^i}{\sigma_y})\sigma_{a,c}^i\right]} \\ D_c^\tau = \sum_{i=1}^{N_\tau} \dfrac{1}{f\left[(1+\eta\frac{\sigma_m{}^i}{\sigma_y})\tau_{a,c}^i\right]} \end{cases} \tag{3.5}$$

where $\sigma_m{}^i$ is mean stress at i[th] cycle, $\sigma_{a,c}^i$ and $\tau_{a,c}^i$ are normal and shear stress amplitude on critical plane at i[th] cycle, respectively.

Following this, an equivalent stress transformation is proposed. The main objective of this paper is to convert a complex multiaxial variable amplitude load path to a simpler constant amplitude multiaxial loading condition in order to predict the fatigue life using Liu-Mahadevan model. Equivalent stress transformation from random loading to constant loading has been investigated for fatigue crack propagation [71], which is based on crack growth rate

equivalence. In this section, an equivalent stress transformation for fatigue life prediction is proposed, which is based on fatigue damage equivalence on the critical plane.

For stationary variable amplitude loading, damage from normal stress amplitude D_c^{σ}, shear stress amplitude D_c^{τ}, and hydrostatic stress amplitude D_c^{H} on the critical plane for one block is investigated using rainflow accounting algorithm and Miner's rule. Mean stress correction factor is also included. The equivalent normal stress $\sigma_{a,c}^{eq}$ and shear stress $\tau_{a,c}^{eq}$ is defined as they have the same normal and shear damage on the critical plane with a given equivalent number of loading cycles, which can be expressed using damage mechanics concept given in Eq. (3.6):

$$\begin{cases} D_c^{\sigma} = N^{eq} \times \dfrac{1}{f(\sigma_{a,c}^{eq})} \\ D_c^{\tau} = N^{eq} \times \dfrac{1}{f(\tau_{a,c}^{eq})} \end{cases} \tag{3.6}$$

where N^{eq} is number of loading cycles for equivalent normal and shear stresses. For consistency, N^{eq} is assumed to be the total number of cycles or reversals of tensile spectrum from the rainflow accounting algorithm. According to the definition of equivalent stress, the damage components on the critical plane in Eq. (3.5) and Eq. (3.6) are same. Thus, combining Eq. (3.5) and Eq. (3.6), there are two equations and two unknowns, $\sigma_{a,c}^{eq}$ and $\tau_{a,c}^{eq}$, which can be solved, as

$$\begin{cases} \sigma_{a,c}^{eq} = f^{-1}\left(\dfrac{N^{eq}}{D_c^{\sigma}}\right) = f^{-1}\left(N^{eq} \Big/ \sum_{i=1}^{N_\sigma} \dfrac{1}{f\left((1+\eta\dfrac{\sigma_m^{\,i}}{\sigma_y})\sigma_{a,c}^{i}\right)}\right) \\ \tau_{a,c}^{eq} = f^{-1}\left(\dfrac{N^{eq}}{D_c^{\tau}}\right) = f^{-1}\left(N^{eq} \Big/ \sum_{i=1}^{N_\tau} \dfrac{1}{f\left((1+\eta\dfrac{\sigma_m^{\,i}}{\sigma_y})\tau_{a,c}^{i}\right)}\right) \end{cases} \tag{3.7}$$

The equivalent hydrostatic stress $\sigma_{a,c}^{eq,H}$ can be computed from the average of the hydrostatic stress spectrum since it is not dependent on the critical plane orientation. Therefore, a random loading block can be converted to a constant loading condition with equivalent normal and shear stress, $\sigma_{a,c}^{eq}$, $\tau_{a,c}^{eq}$, on the critical plane with N^{eq} number of cycles. Comparing with the original random loading condition, the equivalent constant loading condition has the same orientation of the critical plane and the same fatigue damage on the critical plane. Thus, the equivalent normal, shear and hydrostatic stress can be used for fatigue life prediction as shown in the constant completed loading cases by Liu and Mahadaven [28]. Eq. (3.1) is modified by replacing the constant amplitude loading with the equivalent constant amplitude loading as shown in Eq. (3.8),

$$\sqrt{(\frac{\sigma_{a,c}^{eq}}{f_{-1}})^2 + (\frac{\tau_{a,c}^{eq}}{t_{-1}})^2 + k(\frac{\sigma_{a,c}^{eq,H}}{f_{-1}})^2} = \beta \tag{3.8}$$

where $\sigma_{a,c}^{eq}$ $\tau_{a,c}^{eq}$ and $\sigma_{a,c}^{eq,H}$ are the equivalent normal, shear, and hydrostatic stress amplitudes acting on the critical plane, respectively.

Finally, life prediction can be performed following the similar procedure shown in [28]. Eq. (3.8) can be rewritten as Eq. (3.9)

$$\frac{1}{\beta}\sqrt{(\sigma_{a,c}^{eq})^2+(\tau_{a.c}^{eq}\frac{f_{-1}}{t_{-1}})^2+k(\sigma_{a,c}^{eq,H})^2}=f_{-1} \tag{3.9}$$

The left-hand side of Eq. (3.9) can be treated as an effective stress term and can be related to uniaxial S-N curve for fatigue life prediction. Thus, the fatigue model for variable loading condition of finite life N is expressed in Eq. (3.10) as:

$$\frac{1}{\beta}\sqrt{(\sigma_{a,c}^{eq})^2+(\tau_{a.c}^{eq}\frac{f_{-1}}{t_{-1}})^2+k(\sigma_{a,c}^{eq,H})^2}=f_{N} \tag{3.10}$$

where N means the predicted fatigue life under the equivalent constant loading. Eq. (3.10) is the general formulation for finite life prediction under general random multiaxial loading spectrums.

3.4 Experimental Testing

Fatigue testing was conducted and the test system used was an MTS 809 close-loop servohydraulic axial-torsion load frame with a load capability of 100 kN and 1100 N m. Axial/Torsion tests were conducted at a frequency of 5 Hz, using different sinusoidal load spectrums in force and torque control. The experimental setup and test system are presented in Figure 3-2. The load spectrum was repeated until failure, which was defined as either a 5% increase in the maximum displacement or angle amplitude; or the appearance of a visible crack length of 2~5 mm on surface. A representative image of the observed fatigue failure and resultant crack orientation is presented in Figure 3-3. Duplicate tests for proportional loading conditions were performed to verify the results obtained.

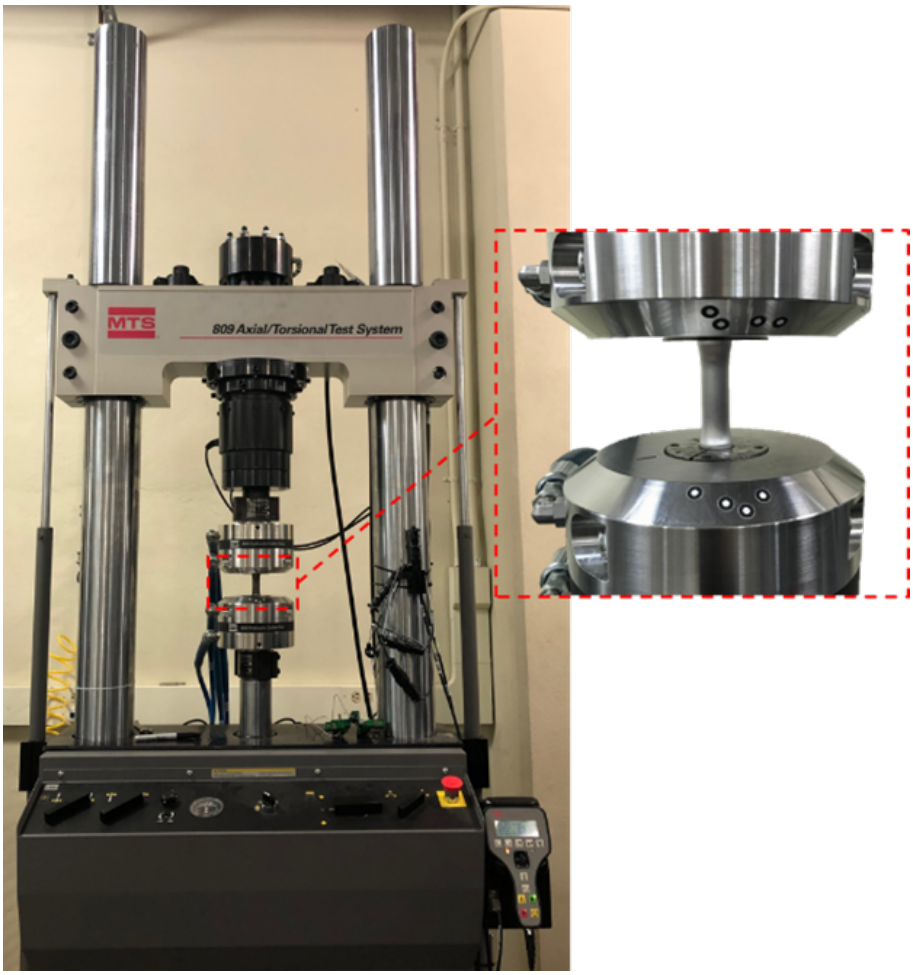

Figure 0-13. Experimental Testing Setup.

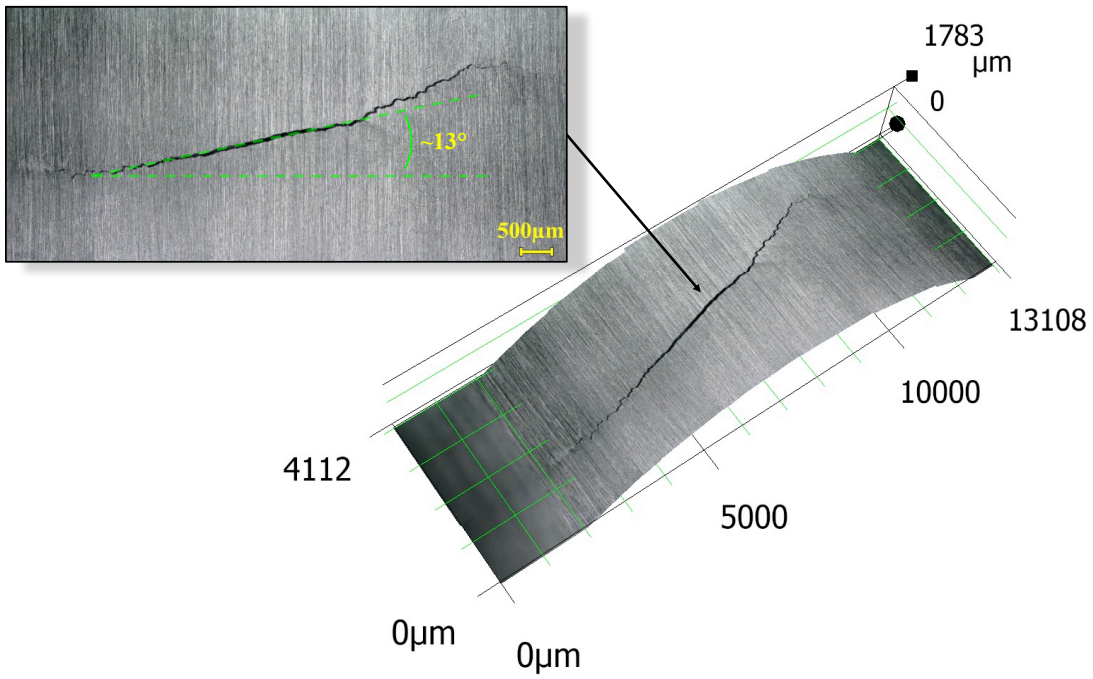

Figure 0-14 Optical Microscope Image of Fatigue Failure under Multiaxial Random Loading and Crack Orientation

Testing material is Al-7075-T6 from a commercial vendor. The specimen design follows ASTM standard E2207-15 (shown in Figure 3-4). A tubular thin-walled specimen geometry is used to minimize the stress gradient effect across the thickness direction.

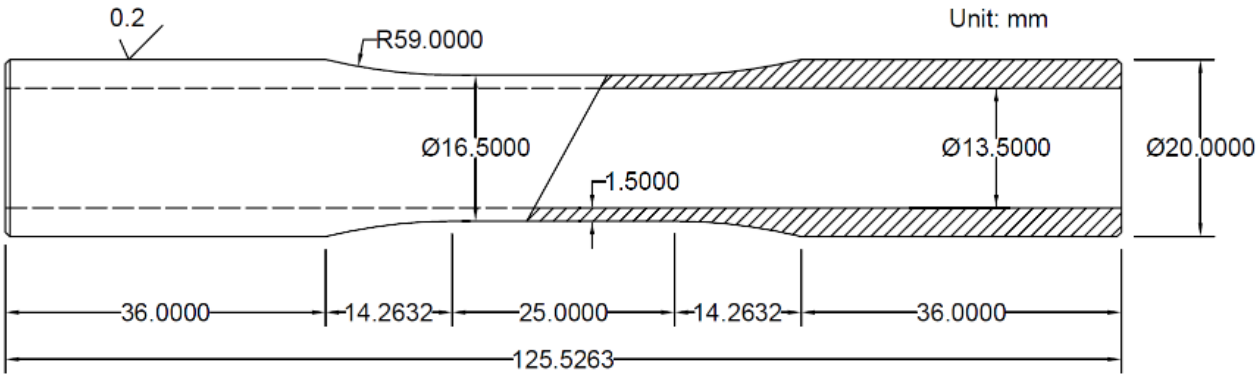

Figure 0-15. Specimen design for multiaxial fatigue testing

Nonlinear, nonstationary standard fatigue spectra were generated. Table 3-2 lists the characteristics of the selected spectra. A linear nonstationary fatigue spectrum, also generated using Auto Regressive (2) (AR(2)) process where the stationarity of spectrum was tested via Hinch method [72].

The equation used for linear nonstationary spectrum generation is,

$$x(n) = a_1(n)x(n-1) - a_2 x(n-2) + \eta \tag{3.11}$$

where

$$a_1(n) = 2\cos(\frac{2\pi}{T(n)})e^{-\frac{1}{T}}, a_2 = e^{-\frac{2}{T}} \tag{3.12}$$

$$T(n) = T_e + M_T \sin(\frac{2\pi t}{T_{\text{mod}}}) \tag{3.13}$$

with M_T=6 for non-stationary conditions and $\eta \sim N(0,1)$.

Table 0-3 Standard Fatigue Spectra.

Name	Purpose	Structural details	Description of load history	Block size (cycles)	Equiv. usage	No. of load levels	Ref
FELIX	Helicopters fixed rotors	Rotor blade bending	Blocks of cycles with different amplitude and mean stress levels	2.3×10^6	140	33	[73]
FALSTAFF	Fighter aircraft	Wing root	Maneuver dominated spectrum, moderate fluctuation of mean stress	18000	200	32	[74]

Mini TWIST	Shortened version of TWIST	Wing root bending moment	Omission of low gust load cycles	62000	4000	20	[75]

Fatigue spectra for uniaxial, in phase and out of phase axial-torsion test cases are shown in Figure 3-5. FELIX and linear spectra that are shown in Figure 3-5 (a) and (b), respectively. Non-proportional loading spectrum was generated based on FALSTAFF spectrum. Figure 3-5 (c) and (d) show the proportional and non-proportional fatigue spectra.

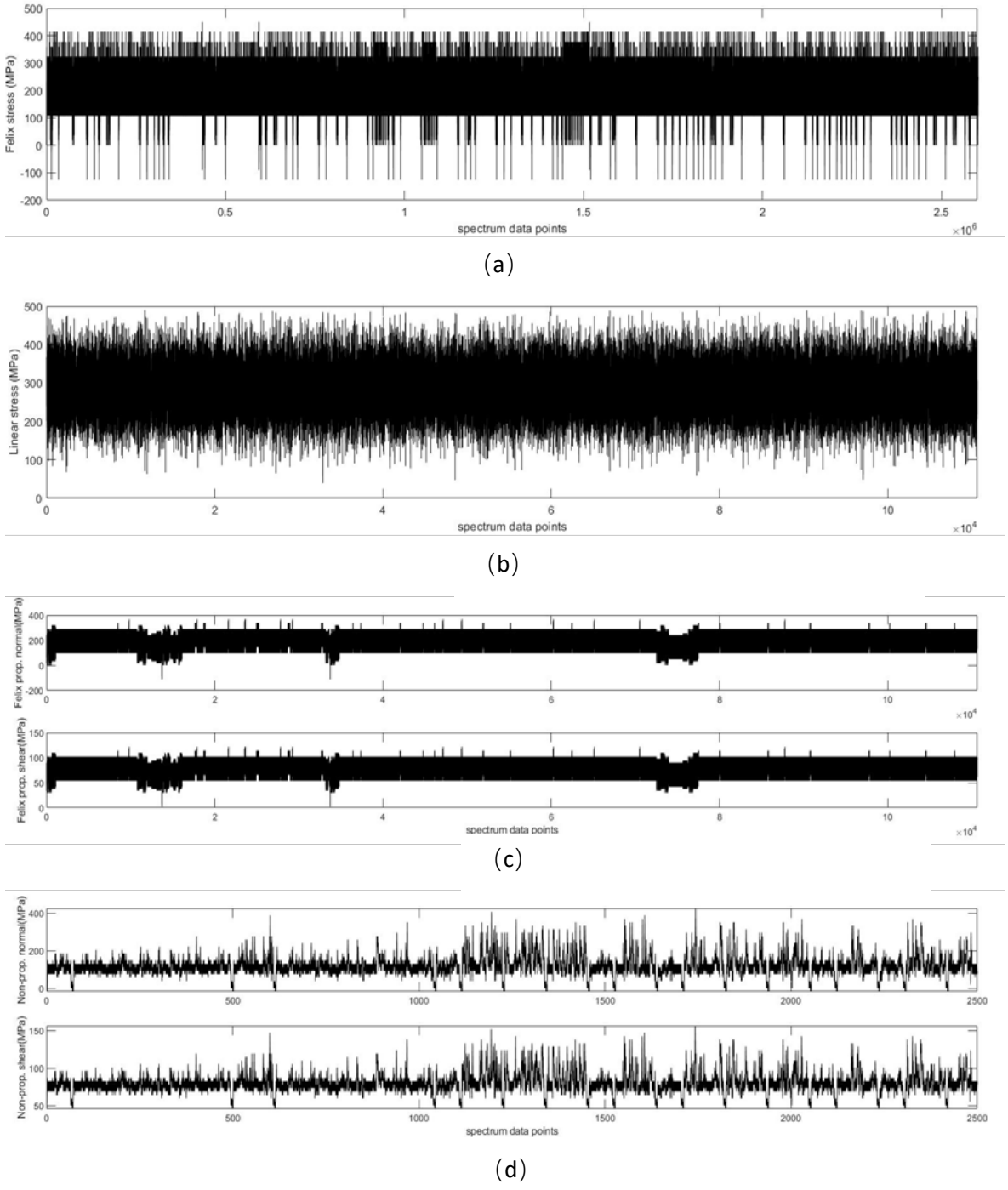

Figure 0-16. Generated Spectra for Fatigue Experiments (a) Axial Spectrum Based on FELIX, (b) Linear Spectrum Based on AR(2), (c) Proportional Spectrum Based on FELIX, and (d) Non-proportional Spectrum Based on FALSTAFF.

Fatigue test results of all finished specimen are presented in Table 3-3, which includes the test number, the load spectrum used, and number of reversals to failure.

Table 0-4 Experimental Testing Summary.

Test No.	Load	Number of reversals	Test No.	Load	Number of reversals
1	Multiaxial (Proportional)	1,340,500	7	Uniaxial	5,956,555
2	Multiaxial (Proportional)	1,748,119	8	Uniaxial	1,971,920
3	Multiaxial (Non-proportional)	1,221,030	9	Uniaxial	2,905,820
4	Multiaxial (Proportional)	2,553,210	10	Uniaxial	1,196,807
5	Multiaxial (Non-proportional)	405,053	11	Uniaxial	2,112,921
6	Uniaxial	736,909			

3.5 Model Validation

The proposed fatigue model is applied to predict the fatigue life of Al-7075-T6 under uniaxial and multiaxial variable amplitude loading conditions. The basic material properties used are from open literature [76]. Young's modulus is 71GPa. Poisson's ratio is 0.3. Yield stress is 503MPa. The proposed fatigue model predicts fatigue live under multiaxial constant loading condition based on experiment data from literature [76] and under random loading based on our in-house fatigue testing data. In order to validate the variable fatigue model, the predicted fatigue lives are compared with the experimentally obtained fatigue lives. The comparison is shown in Figure 3-6.

The solid line indicates that the predicted results are identical with experimental results, i.e., the perfect fit line. The dashed lines are the bounds of fatigue life scatter with a factor of 2. The comparison considers different loading conditions including uniaxial and multiaxial

loading, proportional and non-proportional loading. As can be seen in the figure, the predicted results are in good agreement with experimental results not only under constant loading but also under random loading with or without mean stress.

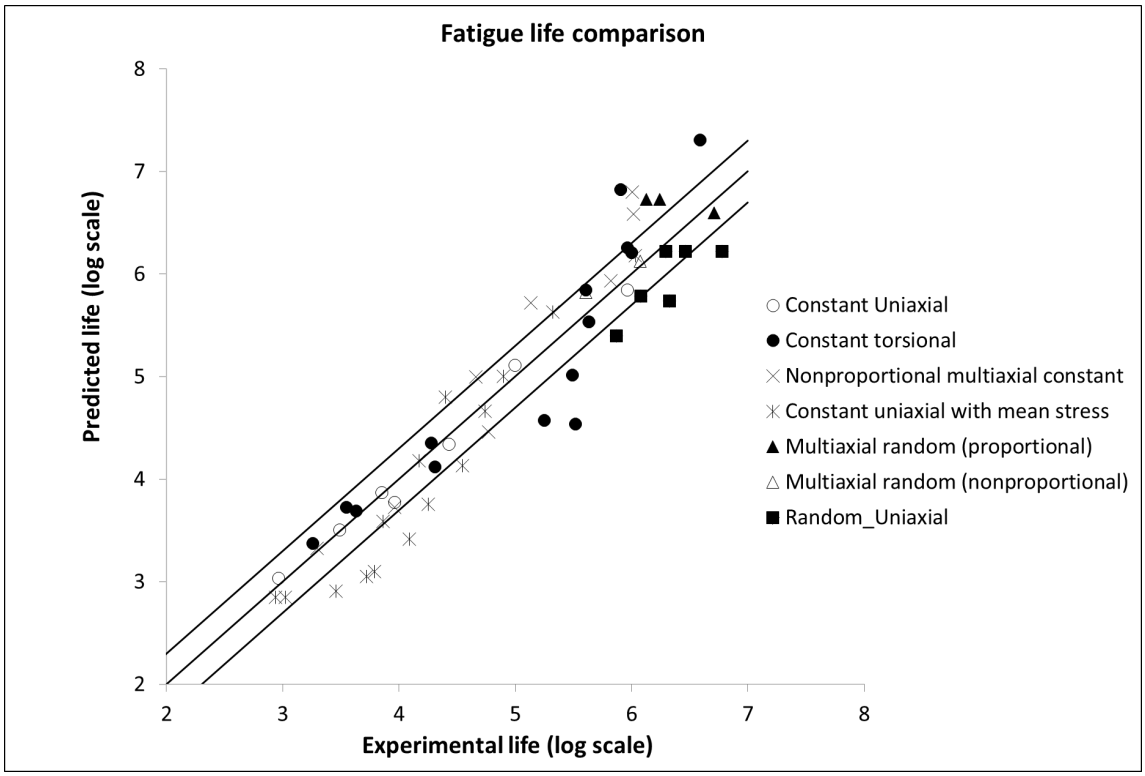

Figure 0-17. Comparison of Model Prediction with Experimental Results

3.6 Conclusion and Future Work

In this paper, a stress-based fatigue model under arbitrary random multiaxial loading is proposed using the Liu-Mahadeven critical plane concept and an equivalent stress transformation method. To validate the proposed model, Al-7076-T6 are tested under different loading conditions. It is shown that the proposed model predictions have satisfactory accuracy without systematic errors for both random uniaxial loading and multiaxial loading. Several major conclusions can be drawn from the proposed study

- The fracture plane is determined under variable loading condition by using the maximum damage plane concept.
- The proposed equivalent stress transformation can reduce a random loading case to a simple constant loading case for easy fatigue life prediction, which avoids cycle-by-cycle calculation of fatigue damage.
- The current model validation shows that the linear damage accumulation rule, i.e., the Miner's rule, provides a satisfactory result for the investigated random spectrum.

The current investigation focuses on the high cycle fatigue (HCF). Future work to extend the concept to low cycle fatigue (LCF) and to mixed HCF+LCF is needed. Linear damage accumulation is shown to have satisfactory results and the used spectrum are not highly nonstationary, such as high-low and low-high step loading. Further confirmation of the applicability of linear damage accumulation rule is needed under other types of multiaxial random loading. Probabilistic modeling considering both material randomness and loading randomness needs further study. Special focus should be on the uncertainty quantification and modeling with limited number of fatigue data is needed as it will be very time consuming and expensive to design and repeat the testing all possible combinations (e.g., loading conditions, material surface finish).

4. MULTIAXIAL FATIGUE MODEL FOR TENSION-TENSION AND TENSION-TORSION LOADINGS

A new energy-based fatigue life prediction model is proposed for arbitrary multiaxial constant loadings in this paper. First, a brief review for existing multiaxial fatigue models is given, especially focusing on energy-based models. It is observed that most multiaxial model formulation and validation are suitable for axial-torsional loadings but may not be appropriate for biaxial tension-tension loading. One possible reason is the ignorance of hydrostatic stress-state difference under these two types of loadings. In view of this, a new model is proposed by including fatigue damage contributions of equivalent tensile energy, torsional energy, and hydrostatic energy. Next, a loading transformation is proposed to transfer a complicated three-dimensional loading to an effective loading for life prediction. Detailed discussion of different types of multiaxial loading and its relationship with the ratio of distortional energy and dilatational energy is given. The hysteresis energy can be calculated integrating the proposed model with the Garud cyclic plastic model, which is directly linked to the damage accumulation and fatigue life prediction. The proposed model is validated with extensive experimental data under both tension-torsion loadings and biaxial tension-tension loadings from open literature. Comparison with several widely used multiaxial model is also given to show the model performance with respect to different biaxial tension-tension loadings. Finally, concluding remarks and future work based on the investigated materials are discussed.

4.1 Introduction

Multiaxial fatigue is a common issue for many practical engineering structures and components. Accurate fatigue life prediction is necessary to ensure the long-term integrity of these structures and components. Extensive multiaxial fatigue models have been proposed to

predict fatigue life. These multiaxial fatigue models can be classified into four categories: stress-based[11], [12], strain-based[13], [14], energy-based[15], [16] and fracture mechanics-based[17].

Stress-based models are mostly used to predict fatigue life for high cycle fatigue. Strain-based models are suitable for low cycle fatigue in which plastic deformation is significant. Since only the strain terms are used, it cannot include the out-of-phase hardening behaviour explicitly. The direction of principal stress is rotating under out-of-phase loading. Comparing with proportional loading, the rotation brings additional hardening to material which causes stress amplitude increase and thus reduces the fatigue life. In order to compensate for the out-of-phase hardening, empirical calibration parameters are used[64]. Energy-based models can consider this effect because both the stress and strain terms are inherent in the energy expression. Critical plane is a well-known approach of fracture mechanics-based models which is based on experimental observation of fatigue crack nucleation growth direction. Many models[18], [19] assume the maximum shear stress range plane as the critical plane which is suitable for ductile failure. Other models assume the maximum normal stress range plane as the critical plane which is mostly suitable for brittle failure[21]–[23]. Carpinteri [24] presented an empirical function to let the critical plane change its orientation for different failure modes, i.e., along the maximum normal stress range plane for brittle materials and along the maximum shear stress range plane for ductile materials. Liu and Mahadevan proposed an analytical solution for the critical plane orientation based on the material ductility using stress term[77] and strain term[29]. Several energy-based models[20], [30], [78] using the critical plane concepts are shown to be successful for multiaxial fatigue life prediction under non-proportional loading. Comprehensive reviews were conducted by Han et al.[79] and Lei et

al.[80] to evaluate various fatigue damage models. The use of Varvani's energy-based damage model through involvement of axial and shear energy components on the critical plane was found vigorously applicable for various multiaxial loading conditions.

The authors observed that most critical plane-based approaches ignore the damage contribution from axial stress/strain parallel to the critical plane (in another words, hydrostatic stress/strain components). This approach may be appropriate under uniaxial loadings and tension-torsion loadings but is questionable for biaxial tension-tension loading. Either direction axial stress/strain (e.g., perpendicular or parallel to the critical plane) may or may not be ignored. Extensive multiaxial fatigue models using the critical plane approach were validated under tension-torsion loading conditions. However, if the loading condition is complicated, such as biaxial tension-tension loadings and hydrostatic loadings, the critical plane approach might be hard to determine the orientation of the critical plane and usually leads to large error of the fatigue life prediction [81].

In view of the above-mentioned difficulties, the motivation of the current study is to develop a universal multiaxial fatigue formulation which is capable to both tension-torsion and tension-tension loadings. We are particularly interested in the energy-based approach as it is suitable for both high-cycle and low-cycle fatigue. In addition, out-of-phase hardening can be naturally included. Thus, the following discussion only focuses on energy-based models. In the open literature, many existing energy-based models are introduced by different authors. Morrow[82] offered an accumulated plastic work as a parameter for fatigue failure. Ellyin[83]–[85] suggested using total strain energy density for multiaxial fatigue prediction under proportional loading. Garud[86] modified Mróz's cyclic plastic model to calculate the plastic work per

cycle, which can predict multiaxial fatigue life under non-proportional loading. These plastic work-based models are not suitable for high cycle fatigue region in which plastic deformation is negligible. Glinka et al.[19] proposed a damage parameter which is a summation of normal energy density and shear energy density. Later, Glinka et al.[87] modified this parameter by including the mean stress effect. Chen et al.[78] suggested using two different energy parameters for different failure modes. They proposed to use the maximum normal stress range plane for brittle failure mode and to use the maximum shear stress range plane for ductile failure mode. Glinka's and Chen's models both use the critical plane approach, which have same problems under biaxial tension-tension loading as abovementioned. Varvani-Farahani and his coworkers[20], [88], [89] developed energy-based multiaxial models to evaluate fatigue damage and life of various materials under multiaxial loading conditions.

Based on the above review and discussion, the objective of the proposed study is to develop an energy-based multiaxial model subjected to complicated constant loading conditions, e.g. torsion-tension loading and biaxial tension-tension loading. The developed model can be applied to different materials under both proportional and non-proportional loadings without calibration using additional out-of-phase multiaxial testing results. The paper is organized as follows. First, the energy-based model is formulated for arbitrary constant amplitude loadings, and the model parameters are analytically derived. Following this, in order to apply the developed model, the relationship in terms of energy parameters and distortional/dilatational energy components is studied for fatigue life prediction. Next, several experimental data available from open literature are used to validate the proposed model. Fatigue lives are compared between computational results and experimental observations. For the biaxial tension-tension loadings, the predicted fatigue lives from the proposed model are compared

with some existing fatigue models. Finally, discussions and conclusions are drawn based on the proposed study.

4.2 Proposed Energy-based Multiaxial Fatigue Model

The proposed study includes three major components. First, distortional (W^{dis}) and dilatational energy (W^{dil}) components are calculated under general three-dimensional cyclic conditions. A cyclic-plasticity model is needed for this purpose and any available models can be used based on users' preference. We choose Garud's model due to its simplicity and it has been shown to yield very good results for fatigue analysis in Ref[30]. Next, the distortional (W^{dis}) and dilatational energy (W^{dil}) components are used to calculate the proposed energy-related damage parameters and the proposed damage criterion. The equivalent tensile energy (W^{ten}), torsional energy (W^{tor}), and hydrostatic energy (W^{H}) are proposed to formulate an energy-based criterion, which depends on the fatigue limits in terms of energies using classical uniaxial and pure torsional fatigue testing (e.g., W_{-1}^{ten} and W_{-1}^{tor}). Following this, the proposed fatigue damage criterion is extended to fatigue life prediction model by using an effective tensile energy term and uniaxial energy-N curve for life prediction[28]–[30]. A flow chart, shown in Figure 4-1, illustrates the procedures and details are discussed in the following sections.

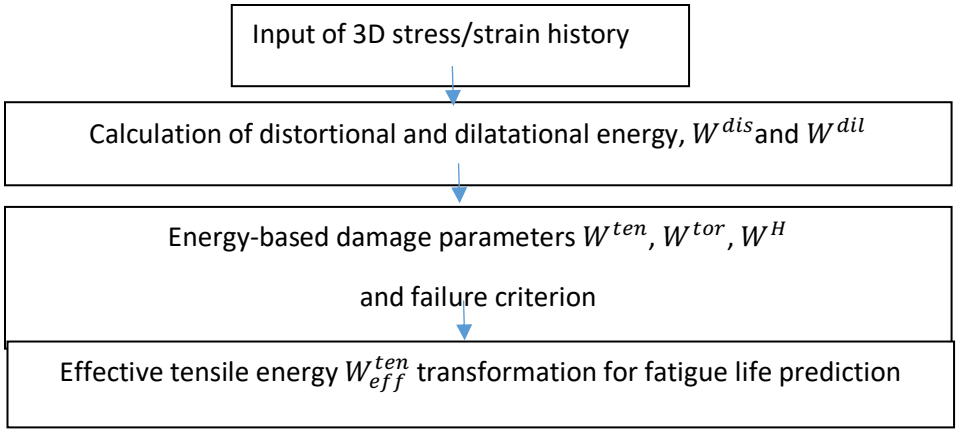

Figure 0-18Flowchart of the Proposed Multiaxial Fatigue Life Prediction Model

Distortional and Dilatational Energy Calculation

The stress and strain hysteresis loops are required before calculating the distortional and dilatational energy components. If both stress and strain components are measured and reported from experimental testing, they can used directly for energy calculation. If not, a cyclic constitutive model is required to calculate one of them given the other. For example, the stress response under the displacement-controlled lab testing needs to be calculated for the application of the proposed energy-based life prediction model. The calculation algorithms for general multiaxial cyclic loadings are discussed below.

In the elastic stage, the calculation of the stress and strain response is straightforward. A cyclic stress-strain relationship can be described by Hooke's law as:

$$\varepsilon_{ij} = \frac{1+\nu}{E}\sigma_{ij} - \frac{\nu}{E}\sigma_{kk}\delta_{ij} \tag{4.1}$$

where σ_{ij} and ε_{ij} stress and strain tensor, and δ_{ij} is Kronecker delta.

For the cyclic elastoplastic deformation, the above-mentioned solution is no longer valid. In order to calculate the stress/strain hysteresis, the Garud incremental cyclic plasticity model is employed for low cycle fatigue region[86]. Mróz introduced the field of plastic moduli [90].

The key concept in the Mróz model is that the Ramberg-Osgood curve can be regarded as a baseline stress-strain relation and is approximates by the piecewise several line segments. The plastic modulus for each segment is the slope of the line which is different for different segments. The flow rule, determining the incremental strain, is based on these plastic moduli. The approximation is illustrated in Figure 4-2. This approach can be applied to arbitrary stress-strain curves and is illustrated here using the Ramberg-Osgood function. According to the approximated stress-strain curve, plasticity surfaces are defined in the stress space corresponding to the stress points on the approximation lines. The material is considered to be isotropic. Thus, all the surfaces are concentric. For the hardening rule in Mróz model, the surface movement is defined as in the direction of the incremental stress. Garud modified the hardening rule in Mróz model as the surface movement is not only depend on the incremental stress but also the surface exterior normal, which ensures all the surfaces are non-intersecting and have a common exterior normal. Mróz model and Garud model have similar results under proportional loading and Garud modification let the cyclic plasticity model can be applied to the non-proportional loading condition. Garud model has been validated by arbitrary non-proportional loading conditions with different materials[30], [91].

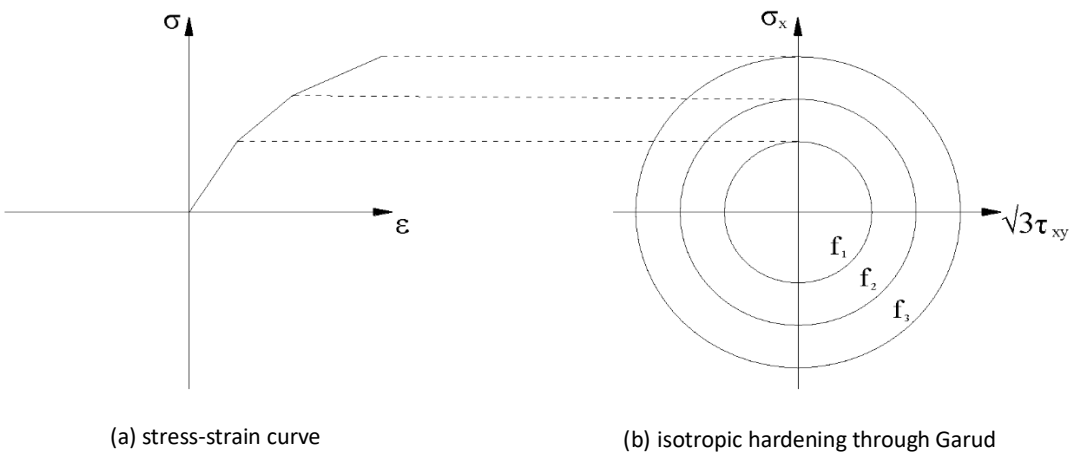

(a) stress-strain curve (b) isotropic hardening through Garud

Figure 0-19 Stain-stress Curve Approximation

Detailed derivation for the Mróz model and Garud model is not given here and interested readers can refer to the original work in Refs[86], [90]. Integrating Garud model, the stress/strain responses can be obtained for the following calculation.

The distortional and dilatational energy components are necessary for the proposed damage model and are calculated here. The total energy can be decomposed into distortional and dilatational energy as:

$$W^t = W^{dis} + W^{dil} \tag{4.2}$$

where W^t is the total energy. The distortional and dilatational energy terms per cycle are given by:

$$W^{dis} = \int_{cycle} S_{ij} d\varepsilon_{ij}^{dis} \tag{4.3}$$

$$W^{dil} = \int_{cycle} \sigma_{kk} \delta_{ij} d\varepsilon_{ij}^{dil} \tag{4.4}$$

where

$$S_{ij} = \sigma_{ij} - \frac{1}{3}\sigma_{kk}\delta_{ij} \tag{4.5}$$

$$\varepsilon_{ij}^{dis} = \varepsilon_{ij} - \frac{1}{3}\varepsilon_{kk}\delta_{ij} \tag{4.6}$$

Eqs. (4.3) and (4.4) can be rewritten in incremental form as:

$$W^{dis} = \sum\nolimits_{cycle} S_{ij}\Delta\varepsilon_{ij}^{dis} \tag{4.7}$$

$$W^{dil} = \sum\nolimits_{cycle} \sigma_{kk}\delta_{ij}\Delta\varepsilon_{ij}^{dil} \tag{4.8}$$

If the plastic deformation occurs, Eq. (4.7) includes both elastic energy and plastic energy. However, Eq. (4.8) only contains the elastic energy, because the plastic deformation is assumed to be incompressible. It should be noticed that all energy terms in the proposed model are defined as the work done by the applied load, which means the energy of the elastic reversible deformation during a cycle is not included,

$$W^{dis} = \sum\nolimits_{cycle} H[sign(S_{ij})sign(\Delta\varepsilon_{ij}^{dis})]S_{ij}\Delta\varepsilon_{ij}^{dis} \tag{4.9}$$

$$W^{dil} = \sum\nolimits_{cycle} H[sign(\sigma_{kk}\delta_{ij})sign(\Delta\varepsilon_{ij}^{dil})]\sigma_{kk}\delta_{ij}\Delta\varepsilon_{ij}^{dil} \tag{4.10}$$

where $H(x)$ is the Heaviside function state as:

$$\begin{cases} H(x) = 1 & x \geq 0 \\ H(x) = 0 & x < 0 \end{cases} \tag{4.11}$$

Eqs. (4.9) and (4.10) are used to calculate the distortional and dilatational energy components in the proposed methodology based on the stress/strain hysteresis loops.

Energy-based Damage Parameter and Failure Criterion

Above discussion is more from a pure mechanics point of view for the different energy component calculation. Distortional and dilatational energy is difficult to be used directly to develop a damage model as the material response under these two energy components are hard to be measured in fatigue testing. Instead, most fatigue testing and material properties are measured under uniaxial or pure torsional loading. Thus, the energy-based damage parameters and corresponding failure criterion are more convenient to be expressed using experimentally measurable quantities. A new fatigue criterion considering contributions of equivalent tensile energy term, torsional energy term, and hydrostatic energy term is proposed as

$$\frac{W^{ten}}{W_{-1}^{ten}} + \frac{W^{tor}}{W_{-1}^{tor}} + \frac{W^{H}}{W_{-1}^{H}} \geq 1 \tag{4.12}$$

where W^{ten}, W^{tor}, and W^{H} are the equivalent cyclic tensile energy, equivalent cyclic torsional energy, and equivalent cyclic hydrostatic energy, respectively. W_{-1}^{ten}, W_{-1}^{tor}, and W_{-1}^{H} are tensile, torsional, and hydrostatic fatigue limit in terms of energy, respectively. The equivalent tensile energy term, torsional energy term, and hydrostatic energy term can be computed using the proposed loading transformation based on the distortional energy and dilatational energy. Eq. (4.12) is a general mathematical expression of the proposed criterion, which has three terms. It should be noticed that Eq. (4.12) is reduced to two terms after loading transformation. The details are included in the discussion of the loading transformation later.

In an earlier work by Jahed et al.[88] an energy-based multiaxial fatigue model at which both components of tensile and torsional energies were introduced. Fatigue limit under hydrostatic stress amplitude is hard to measure and it is expressed using a ratio *k* parameter with the fatigue limit under uniaxial tensile loading as

$$W_{-1}^{H} = \frac{W_{-1}^{ten}}{k} \tag{4.13}$$

The parameter k is the ratio of hydrostatic fatigue limit and uniaxial tensile fatigue limit. Thus, it is material dependent an estimation procedure is discussed later. Substituting Eq. (4.13) to Eq. (4.12), one can obtain

$$\frac{W^{ten}}{W_{-1}^{ten}} + \frac{W^{tor}}{W_{-1}^{tor}} + k\frac{W^{H}}{W_{-1}^{ten}} \geq 1 \tag{4.14}$$

Eq. (4.14) shows that the final damage is a combination of normalized damage of equivalent tensile energy, torsional energy, and hydrostatic energy. This is the proposed damage criterion. The remaining question is how to calculate each energy term and how to determine the model parameters. The third term in Eq. (4.14) presents the normalized damage of the hydrostatic energy. Usually, fatigue test only provides tensile and torsional fatigue limits and cannot estimate three unknown parameters in Eq. (4.14). Thus, a simple hypothesis is made to estimate the relationship between the hydrostatic fatigue limit and tensile fatigue limit to facilitate the fatigue calculation.

Let us consider one metallic material under a hypothetical uniaxial tensile and hydrostatic fatigue loading. The uniaxial and hydrostatic loading will lead to the fatigue limit in term of stress as σ_{-1}^{ten} and σ_{-1}^{H}, respectively. If the fatigue loading is extrapolated to the extreme case under static loading (e.g., fatigue failure in one cycle), the tensile stress will approach the yield strength σ^{y} of the material. In case of hydrostatic loading, if the fatigue loading is extrapolated to the extreme case under static loading, we assume σ_{-1}^{H} will approach the ultimate strength of the material (i.e., equivalent to the maximum normal stress failure theory). Thus, the following proportional rule is assumed to hold true

$$\frac{\sigma^y}{\sigma^u} = r = \frac{\sigma_{-1}^{ten}}{\sigma_{-1}^{H}} \tag{4.15}$$

where *r* is the ratio of the yield strength and ultimate strength. The ratio *r* ranges from *0* to *1*. *r* approaches *0* when the yield strength is much less than the ultimate strength. *r* approaches 1 when the yield strength approaches the ultimate strength. It should be noted that this is a hypothesis/assumption in the proposed model. The validation section later in this paper shows good accuracy for all investigated materials for this hypothesis. Future study is required to extend the validation or modification for other material systems. For elastic deformation at the fatigue limit stage, the tensile and hydrostatic fatigue energy limit can be expressed as:

$$W_{-1}^{ten} = \frac{(\sigma_{-1}^{ten})^2}{2E} \tag{4.16}$$

$$W_{-1}^{H} = \frac{3\left(\sigma_{-1}^{H}\right)^2(1-2\nu)}{2E} \tag{4.17}$$

where *E* is the Young's modulus, *G* is the shear modulus, and ν is Poisson's ratio. Substituting Eq. (4.15) and Eq. (4.17) into Eq. (4.13), the parameter k can be solved as:

$$k = \frac{(r)^2}{3(1-2\nu)} \tag{4.18}$$

The parameter *k* is a material constant related to the Poisson's ratio and yield-to-ultimate strength ratio.

Next step is to derive the relationship in terms of energy damage parameters with respect to the distortional and dilutional energy under arbitrary loading conditions. Before we start the detailed formulation, a general description of difference between tension-torsion and tension-tension loading is discussed in terms of the ratio of distortional and dilatational energy. Let us

consider the pure uniaxial tension loading first. The ratio *t* of distortional and dilatational energy under tensile loading is defined as

$$t = \frac{W^{dis}}{W^{dil}} \tag{4.19}$$

Under pure uniaxial tension loading, the ratio *t* is a constant $\frac{2+2\nu}{1-2\nu}$, irrespective of the applied loading levels. For other multiaxial loading cases, this ratio is not a constant and depends on the loading. For larger value of *t* ($t = \frac{W^{dis}}{W^{dil}} > \frac{2+2\nu}{1-2\nu}$), it indicates larger contribution from distortional energy. The extreme value is infinity which corresponds to the pure torsional loading (i.e., W^{dil}=0). For smaller value of *t* ($t = \frac{W^{dis}}{W^{dil}} < \frac{2+2\nu}{1-2\nu}$), it indicates smaller contribution from distortional energy. The extreme value is zero which corresponds to the hydrostatic loading (i.e., W^{dil}=0). It is interesting to see that the three special values 0, $\frac{2+2\nu}{1-2\nu}$, and *+inf* are three special loading conditions (e.g., hydrostatic loading, pure tensile loading, and pure torsional loading). The three special values divide the *t* range into two segments: one segment can be treated as a combined tensile + torsional loading and the other can be treated as the combined tensile + hydrostatic loading. A schematic illustration is shown in Figure 4-3.

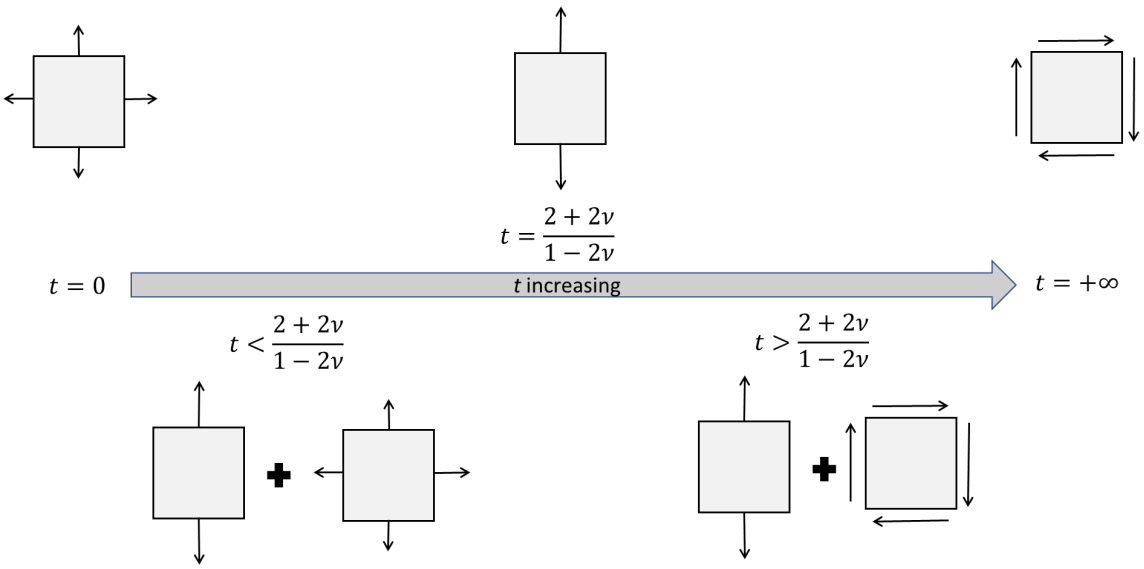

Figure 0-20 Graphic Illustration for Equivalent Loading Combination Based on t *Range*

Based on this graphic representation, we proposed the following concept to develop a multiaxial fatigue model. First, calculate the equivalent tensile energy by maximizing the extraction of proportional distortional energy and dilatational energy from the system. Mathematically,

$$W^{ten} = \min\{\frac{3}{1-2\nu}W^{dil}, \frac{3}{2+2\nu}W^{dis}\} \tag{4.20}$$

After this extraction, there may be remaining energy (either dilatational energy or distortional energy). The equivalent torsional energy is the remaining distortional energy and the equivalent hydrostatic energy is the remaining dilatational energy. It should be noticed that the equivalent torsional energy and the equivalent hydrostatic energy does not equal to the distortional energy and dilatational energy. They are the remaining energy after the extraction.

When $t = \frac{W^{dis}}{W^{dil}} \geq \frac{2+2\nu}{1-2\nu}$, we calculate the tensile energy using the dilatational energy as

$$W^{ten} = \frac{3}{1-2\nu}W^{dil} \tag{4.21}$$

Since there is remaining distortional energy after extracting the tensile energy, the equivalent torsional energy is defined as

$$W^{tor} = W^{dis} - tW^{dil} \tag{4.22}$$

All dilatational energy is used to calculate the equivalent tensile energy and there is no remaining portion. Thus, the equivalent hydrostatic energy is

$$W^{H} = 0 \tag{4.23}$$

When $t = \frac{W^{dis}}{W^{dil}} \leq \frac{2+2\nu}{1-2\nu}$, we calculate the tensile energy using the distortional energy as

$$W^{ten} = \frac{3}{2+2\nu} W^{dis} \tag{4.24}$$

Since there is remaining dilatational energy after extracting the tensile energy, the equivalent hydrostatic energy is defined as

$$W^{H} = W^{dil} - \frac{W^{dis}}{t} \tag{4.25}$$

Since there is no distortional energy left after extracting, the torsional energy is

$$W^{tor} = 0 \tag{4.26}$$

As a summary, the calculation of equivalent energy terms is summarized in Table 4-1. In practice, the ratio of dilatational and distortional *t*, is calculated first. Table 4-1 is then used to find equivalent energy terms and substituted to proposed multiaxial fatigue model (Eq. (4.12)) for fatigue analysis.

Table 0-5 Summary of the Equivalent Energy Term Calculation in the Proposed Model

t	$t = \frac{W^{dis}}{W^{dil}} \geq \frac{2+2\nu}{1-2\nu}$	$t = \frac{W^{dis}}{W^{dil}} \leq \frac{2+2\nu}{1-2\nu}$
W^{ten}	$W^{ten} = \frac{3}{1-2\nu} W^{dil}$	$W^{ten} = \frac{3}{2+2\nu} W^{dis}$

W^{tor}	$W^{tor} = W^{dis} - tW^{dil}$	$W^{tor} = 0$
W^{H}	$W^{H} = 0$	$W^{H} = W^{dil} - \frac{W^{dis}}{t}$
Failure criterion	$\frac{W^{ten}}{W_{-1}^{ten}} + \frac{W^{tor}}{W_{-1}^{tor}} \geq 1$	$\frac{W^{tor}}{W_{-1}^{tor}} + k\frac{W^{H}}{W_{-1}^{ten}} \geq 1$

In order to illustrate the calculation details, three special loading conditions are shown below to show that the proposed method can successfully reproduce the extreme cases.

Case 1: Pure torsional loading

If the dilatational energy is zero, the loading is considered as pure torsional loading in which the distortional energy equals torsional energy density, i.e. $W^{tor} = W^{dis}$. The tensile energy density and hydrostatic energy are both zero. Eq. (4.14) reduces to

$$\frac{0}{W_{-1}^{ten}} + \frac{W^{tor}}{W_{-1}^{tor}} + k\frac{0}{W_{-1}^{ten}} = \frac{W^{tor}}{W_{-1}^{tor}} \geq 1 \tag{4.27}$$

It is clearly shown that the proposed damage criterion (Eq. (4.14)) satisfies the case for pure torsional loading and correctly predict the failure case (e.g., applied W^{tor} equals to the material fatigue limit W_{-1}^{tor}).

Case 2: Hydrostatic loading

In case of hydrostatic loading (no distortional energy), the tensile and torsional energies are zero. The fatigue model has only the third term as

$$\frac{0}{W_{-1}^{ten}} + \frac{o}{W_{-1}^{tor}} + k\frac{W^{H}}{W_{-1}^{ten}} = k\frac{W^{H}}{W_{-1}^{ten}} = \frac{W^{H}}{W_{-1}^{H}} \geq 1 \tag{4.28}$$

Again, this reproduces the failure condition.

Case 3: Uniaxial tensile loading

If the ratio t of distortional and dilatational energy equals the ratio in Eq. (4.19), the loading is considered as an equivalent uniaxial tensile loading. The fatigue model keeps the first term as:

$$\frac{W^{ten}}{W_{-1}^{ten}} + \frac{0}{W_{-1}^{tor}} + k\frac{0}{W_{-1}^{ten}} = \frac{W^{ten}}{W_{-1}^{ten}} \geq 1 \tag{4.29}$$

In this case, it also successfully reproduces the failure condition. The two scenarios in Table 4-1 give the same solution (i.e., solution is continuous when $t = \frac{W^{dis}}{W^{dil}} = \frac{2+2\nu}{1-2\nu}$) and the equivalent tensile energy can be calculated either using dilatational or distortional energy as

$$W^{ten} = \frac{3}{2+2\nu} W^{dis} = \frac{3}{1-2\nu} W^{dil} \tag{30}$$

Fatigue Life Prediction Model

Above discussion is for the fatigue failure criterion at the fatigue limit stage. Following the same methodology in Refs[28]–[30], the fatigue limit criterion can be extended to finite fatigue life prediction by a transformation. For finite fatigue life prediction, the damage parameter should be correlated with the life (i.e., number of loading cycles). Eq. (4.14) can be rewritten as

$$W^{ten} + sW^{tor} + kW^{H} \geq W_{-1}^{ten} \tag{31}$$

where $s = \frac{W_{-1}^{ten}}{W_{-1}^{tor}}$. The left-hand side of the equation can be treated as the effective energy term W_{eff}^{ten} and can be used to correlate with the fatigue life using the uniaxial energy–N curve $f(N_f)$ as

$$W_{eff}^{ten} = W^{ten} + sW^{tor} + kW^{H} = W_{N_f}^{ten} = f(N_f) \tag{4.32}$$

where the ratio s is redefined as $s = \frac{W_{N_f}^{ten}}{W_{N_f}^{tor}}$. N_f is the certain cycle number to failure. The W_{-1}^{ten} and W_{-1}^{ten} are replaced by $W_{N_f}^{ten}$ and $W_{N_f}^{tor}$, respectively, which are fatigue strengths at finite fatigue life N_f. Eq. (4.32) is a nonlinear equation about N_f and numerical method and can be used to solve for N_f [28]–[30]. It should be noted that $f(N_f)$ in Eq. (4.32) can be any functions from data fitting and the current study uses power law fitting.

As a short summary, there are few material constants and loading parameters are required in the proposed model. The parameter *r* is the yield-to-ultimate strength ratio of the material, which is calculated using Eq. (4.15). *k* is a material constant depending on *r* and Poisson' ratio, which is calculated using Eq. (4.18). The parameter *s* is the ratio of tensile and torsional fatigue limits. The parameter *t* is a loading parameter and depends on the applied distortional and dilatational energy, which is calculated using Eq. (4.19).

4.3 Model Validation

Available experimental testing data on multiaxial fatigue lives from open literature are collected and used for model validation. One of the major contributions of the proposed method is that it is a universal model applicable to both tension-torsion and tension-tension loading. Thus, two major types of experimental data are collected. The proposed energy fatigue model

is firstly validated with different materials under tension-torsion constant loading conditions which are commonly used for most existing multiaxial fatigue model validation. Following this, the proposed fatigue model is also validated under the biaxial tension-tension constant loading condition. Model performance is also compared with several other models using reported values.

Validation for tension-torsion loading

Five different materials have been investigated under tensile, torsional and tension-torsion loading. A summary of the collected experimental data is shown in Table 4-2. The normal to shear fatigue limit ratio (*s)* and cyclic stress-strain coefficients in Ramberg-Osgood equation (*K* and *n*) are also reported. The loading waveforms include uniaxial (tensile and torsional) loading, in-phase, and out-phase multiaxial loading. Thus, the selection of these materials is to validate the applicability of the proposed model for different materials experiencing different loading conditions. In Table 4-2, the abbreviation for the multiaxial loading paths is illustrated in Figure 4-4.

Table 0-6 Summary of Collected Experimental Data

Material	Multiaxial loading path	*s*	*K*(MPa)/*n*	Reference
AISI Type 304 stainless steel	Pro, sin90, box, box2	0.594	1660/0.278	[18]
SAE-1045 steel	Pro, sin90, box	1.108	1258/0.208	[92]
A533B pressure vessel steel	Pro, sin90	0.997	827/0.13	[93]
Al-6061-T6	Pro	1.575	410/0.05	[94]
SM45C steel	Pro, sin22, sin45, sin90, box	0.707	1246/0.99	[95]
Al 7075	Pro	0.899	400/0.17	[76]

S460N	Pro, sin90	0.868	1115/0.16	[96]

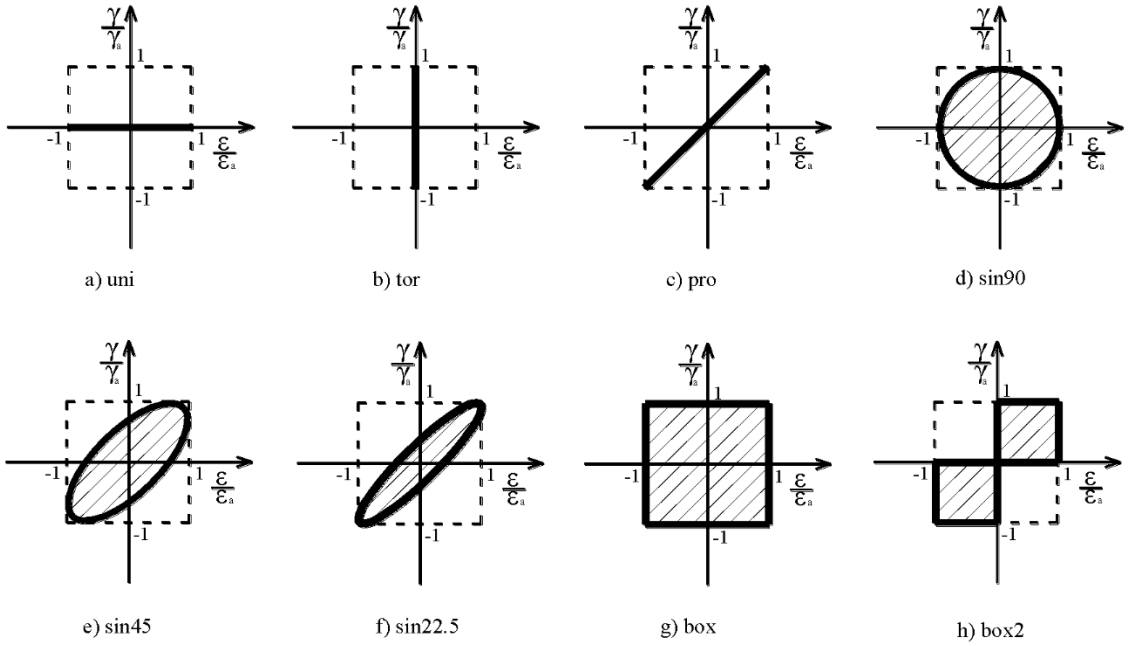

Figure 0-21 Schematic Illustration of the Investigated Loading Waveforms： (a) uni, (b) tor, (c) pro, (d) sin90, (e) sin45, (f) sin22.5, (g) box and (h)box2

Figure 4-5 shows the comparison of the proposed model predictions with experimental measurements. The *x*-axis is the experimental measurements of fatigue lives and the *y*-axis is the predicted lives. Both axes are in log scale. Solid diagonal line indicates the perfect prediction and a life factor of 2 is also shown as the dashed lines. All points are experimental data and different loading waveforms are shown in the legend. It is shown that most of the data falls in the scatter bands of life factor two. Thus, the proposed energy fatigue model is valid for uniaxial loading and multiaxial tension-torsion loading.

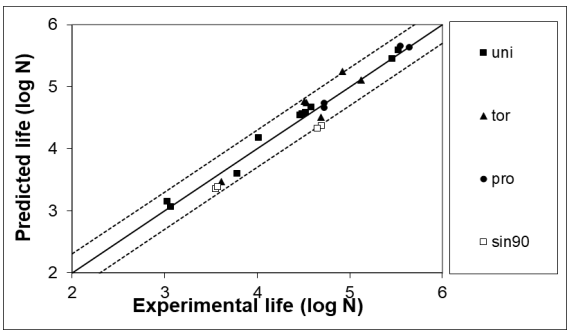

(a) AISI 304 Steel

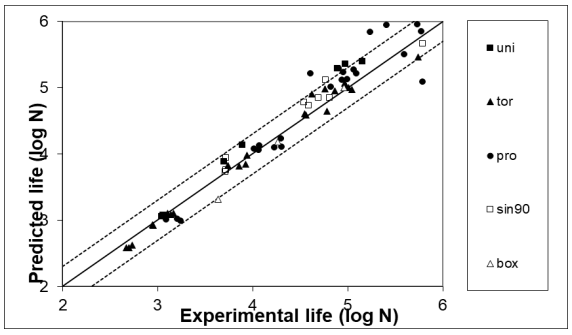

(b) SAE 1045 Steel

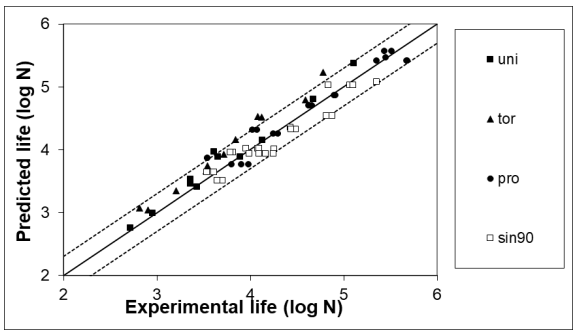

(c) A533B

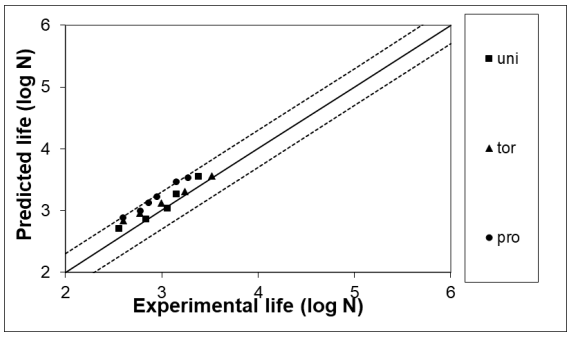

(d) Al 6061

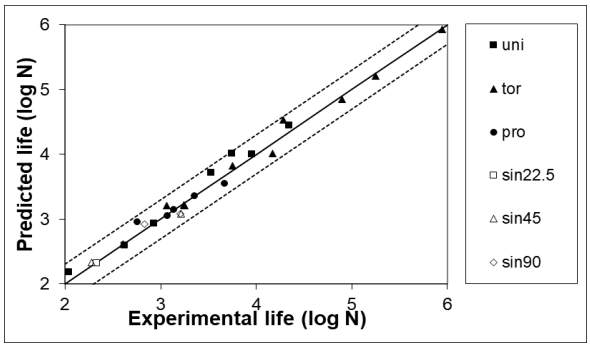

(e) SM45C Steel

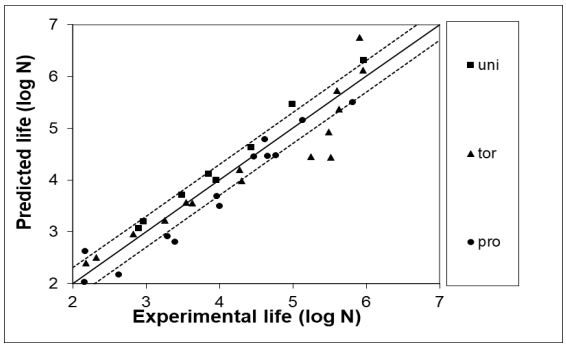

(f) Al 7075

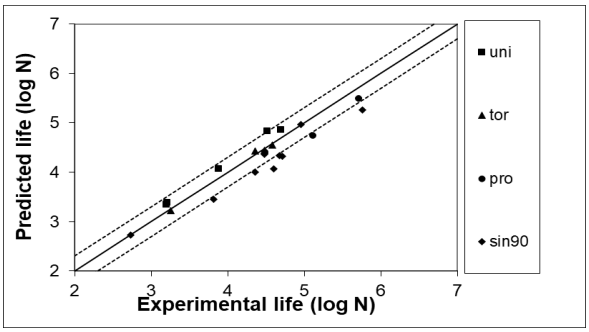

(g)S460N

Figure 0-22 Comparison of Fatigue Life Predictions and Experimental Measurements under Tension-torsion Loadings: (a) AISI 304 Steel, (b) SAE 1045, (c) A533B, (d) Al 6061, (e) SM45C Steel, (f) Al 7075 and (g)S460N.

Validation for biaxial tension-tension loading

Compared with extensive available tension-torsion experimental data in the open literature, biaxial tension-tension fatigue tests are rarely reported. Two different materials are collected and studied under biaxial tension-tension loading. The axial stress amplitude $\Delta\sigma_x$ and $\Delta\sigma_y$ in x and y directions are chosen so as to get the biaxiality ratio B, defined as:

$$B = \frac{\Delta\sigma_y}{\Delta\sigma_x} \tag{4.33}$$

Material 1: Aluminium A1050 H14

Cláudio et al.[81] performed fatigue tests on Aluminum A1050 H14 under proportional and non-proportional biaxial loading conditions. The biaxiality B is 0 for the uniaxial loading, and B is 1 for proportional and non-proportional biaxial loading. The comparison between predicted fatigue lives and experimental fatigue lives is presented in Figure 4-6. Similar with Figure 4-5, the solid line in Figure 4-6 indicates that the predicted life is exactly same as the experimental lives, and the two dashed lines show life factor of 2. The non-proportional loading phase shift is shown in legend. It should be noted that the non-proportional loading with phase shift 180° is equivalent to torsional loadings. As can be seen, the predicted lives agree very well with the experimental lives.

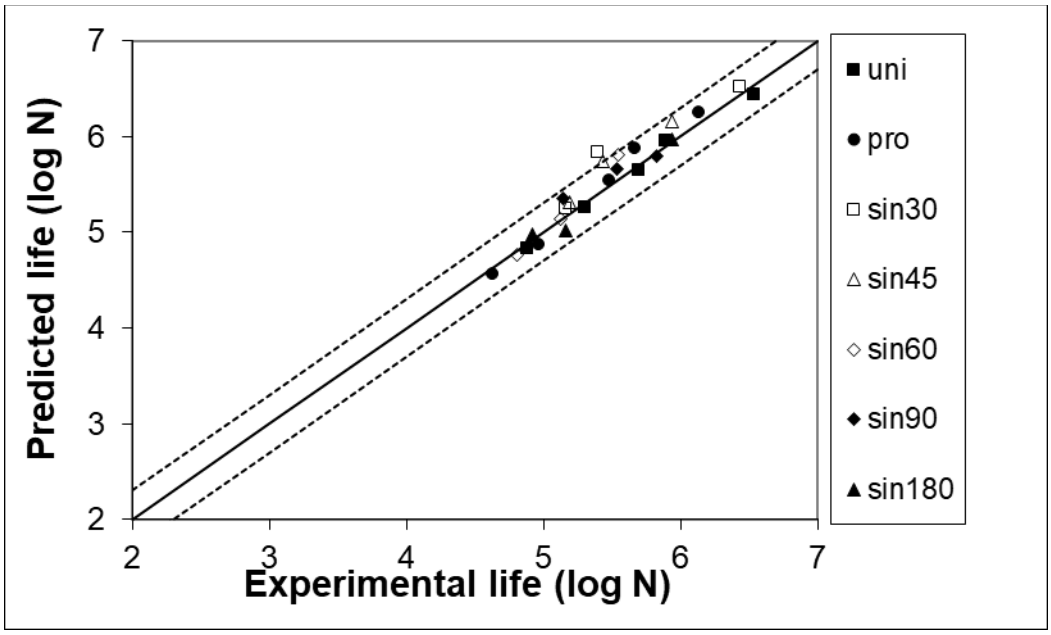

Figure 0-23 Comparison of Fatigue Life Predictions and Experimental Measurements under Biaxial Tension-tension Loadings for Aluminium A1050 H14

Because the biaxial fatigue tests are in high cycle fatigue regime, Cláudio et al. compared the experimental results with model prediction from some well-known stress-based multiaxial fatigue models (Findley[97], Fatemi and Socie (F-S)[98], Minimum Circumscribed Circle (MCC)[99], Minimum Circumscribed Ellipse (MCE)[100] and Carpinteri-Spagnoli (modified C–S)[24]) and the multiaxial fatigue model proposed by themselves (modified C-S and MCE)[81]. All selected models provide results close to the experimental data, but most of them are non-conservative. The details of the comparison can be found in Ref [81]. An error index I used for quantitative comparison is defined as:

$$I = \frac{1}{n}\sum_{i=1}^{n}\frac{|\lambda-\lambda_{ex}|}{\lambda_{ex}}100\% \tag{4.34}$$

where λ and λ_{ex} are predicted and experimental fatigue strength for a certain number of cycles, respectively. The fatigue strength at a certain number of cycles N_f is defined as:

$$\lambda(N_f) = A(N_f)^b \tag{4.35}$$

where A is the fatigue strength coefficient and b is the fatigue strength exponent. Both A and b can be obtained from uniaxial fatigue test. Because the proposed model in this paper is energy-based, the square root of the energy-based strength is used to compute the error index before comparing with other stress-based models. The error index for different models are presented in Table 4-3 including the proposed model in this paper in the last column. Fig. 7 is the plot of the error index.

Table 0-7 Error Index for All Selected Criterion with Average and Standard Deviation

Phase (°)	Findley (%)	F-S (%)	MCC (%)	MCE (%)	Mod. C-S (%)	Mod. C-S and MCE (%)	Proposed model (%)
0	7	11	4	4	7	7	2
30	12	18	12	10	16	5	4
45	2	8	7	13	14	4	4
60	20	7	5	18	8	3	2
90	26	7	5	10	10	7	3
180	34	9	3	3	9	9	2
Avg	16.7	10.1	5.8	9.5	10.5	5.6	2.8
S. dev.	12.0	4.0	3.2	5.7	3.5	2.3	2.1

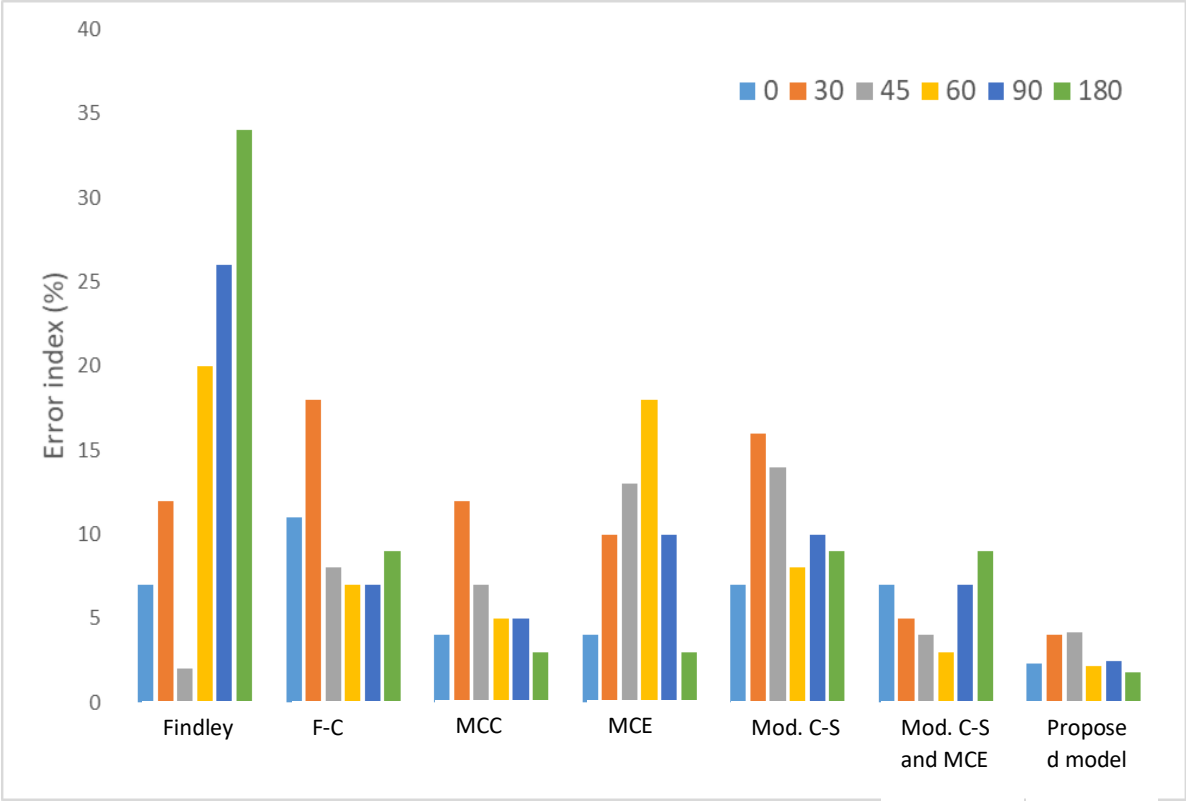

Figure 0-24 Comparison of Error Index for All Aelected Criteria

The proposed multiaxial fatigue model shows better accuracy for biaxial tension-tension test as seen in Figure 4-7. In the Table 4-3, the worst prediction of the proposed model has 4% error index under the loading with 45° phase shift. It appears that predictions for different load paths have similar error index, which indicates the proposed model has no systematic errors with respect to loading waveforms. Some other models do tend to have different errors with respect to different load forms.

Material 2: 2.5%Cr–1%Mo steel

2.5%Cr–1%Mo steel is tested by Gaur et al.[101] under cyclic proportional biaxial tension-tension loading. Gaur et al. tested fatigue life under four different biaxiality ratio B values: 0 (uniaxial), 0.25, 0.5 and 1. The R ratio ($\sigma_{min}/\sigma_{max}$) in the test is 0.25 and the positive mean

stress effect is significant. The positive mean stress in general reduce fatigue life. In the proposed model, the effect of the positive mean stress is considered naturally, because with same stress amplitude, the work done by applied load with positive mean stress is greater than the work done by the applied load with zero mean stress. Therefore, the effect energy in the model, which is used to compute the fatigue life, is larger for positive mean stress. The comparison between predicted results and experimental results are plotted in Figure 4-8.

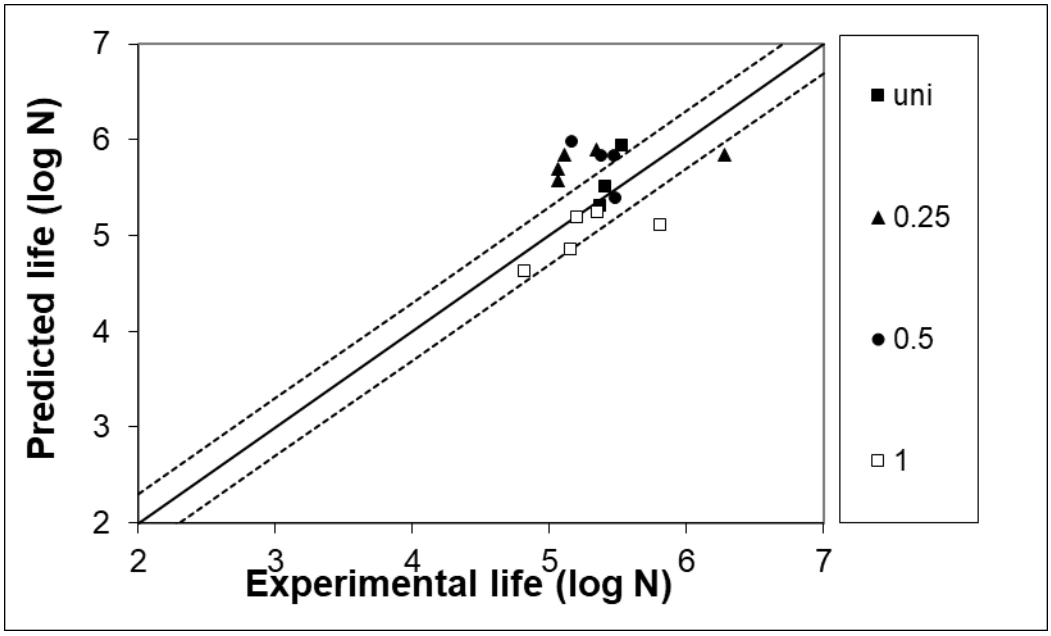

Figure 0-25 Comparison of Fatigue Life Predictions and Experimental Measurements under Biaxial Tension-tension Loadings for 2.5%Cr–1%Mo Steel

Four different biaxiality ratios are shown in the legend. It is shown that the predicted results are close to the mean value experimental data with a large scatter. The authors noticed that the experimental data reported by Gaur et al.[101] shows significant scatter, especially at longer fatigue lives. For example, 129,972 and 1,908,883 (two points of solid triangle in Figure 4-8) are the two fatigue lives for same loading condition of 270 MPa stress amplitude and 0.25 biaxiality. This is more than a magnitude difference (i.e., life factor of 10) from experimental

data. Stochastic fatigue prediction may be more appropriate for this level of uncertainties and needs further study in the future.

4.4 Discussion

The proposed multiaxial fatigue criterion is a universal model applicable to both tension-torsion and tension-tension loading. The validation shows that the predicted results have a good agreement with experimental data under tension-torsion loading, and the proposed model shows a better accuracy than some existing multiaxial fatigue life models under biaxial tension-tension loading. The effect of hydrostatic energy density amplitude is more significant under biaxial tension-tension loading than tension-torsion loading. The proposed multiaxial fatigue criterion considers whole hydrostatic contribution, because the distortional and dilatational energy densities are used in the loading transformation. Most multiaxial fatigue models based on critical plane approach tend to ignore the hydrostatic damage contribution parallel to the critical plane, which is the equivalent hydrostatic energy in the proposed criterion. A case study is presented to show the influence of the hydrostatic energy component in damage and life assessment. The material is Aluminium A1050 H14. Results are shown in Figure 4-9. The equivalent tensile and torsional energy densities in Eq. (4.12) are given as 46800Pa and 0Pa, respectively. The equivalent hydrostatic energy density increases from 0Pa to 40000Pa. It can be seen that the equivalent hydrostatic energy reduces the predicted fatigue life.

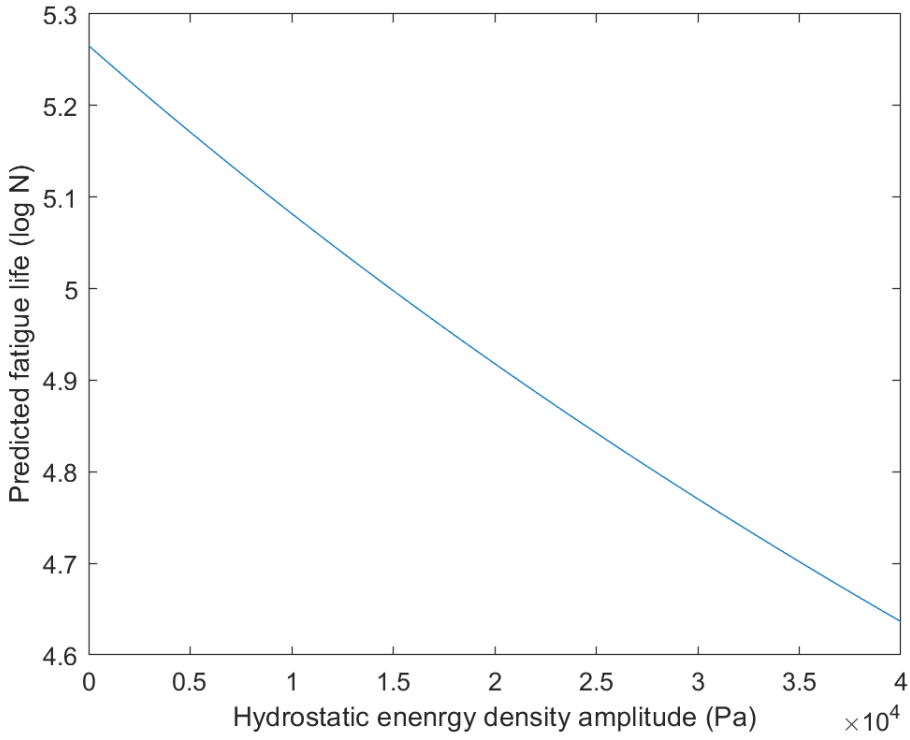

Figure 0-26 The Influence of the Equivalent Hydrostatic Energy Density

4.5 Conclusion and Future Work

In this paper, a new energy-based fatigue model is developed to assess fatigue life under various multiaxial constant amplitude loading conditions with different loading paths. The energy-based model considers three fatigue damage contributions of tensile energy term, torsional energy term, and hydrostatic energy term. In case of only stress or strain reported, Garud cyclic plasticity model is integrated to calculate stress or strain hysteresis. The proposed multiaxial energy-base model is validated by five different materials under tension-torsion loading and two materials under biaxial tension-tension loading. Both proportional and non-proportional loading are considered in the validation. several major conclusions are

- Separation of tensile energy, torsional energy, and hydrostatic energy is able to explain the different multiaxial loading conditions (e.g., tension-torsion and biaxial tension-

tension). The ratio of applied distortional and dilatational energy appears to be an important factor to sperate these two types of multiaxial loadings;

- Garud cyclic plasticity model is shown to be successful to integrate with the proposed multiaxial damage model for hysteresis energy calculation;
- The proposed energy model naturally includes the mean stress effect and does not require cycle counting. Direct load path integration is used to calculate the energy terms and has the potential to be directly applied to random variable loadings.

Since the proposed model is based on the energy concept, it can be integrated with both continuous and discrete computational mechanics models for complex material and structural fatigue analysis. Detailed investigation of the proposed model's correlation with the fatigue damage mechanism in the material (e.g., state I/II of fatigue crack growth, tensile/shear fatigue cracks) is required. As shown in one validation example, extension to probabilistic multiaxial fatigue analysis is critical in order to successfully address the huge uncertainties observed in the experiments.

5. FATIGUE ANALYSIS FOR MICROSTRUCTURES USING A LATTICE PARTICLE METHOD AND A MULTIAXIAL FATIGUE MODEL

Fatigue cracking in homogeneous and composite materials is studied using a non-local lattice particle method (LPM). The LPM defines the particle potential, which involves the pairwise and volume-related energy in the discretized system. Integrating with an energy-based fatigue criterion, LPM performs the power of fatigue simulation. Brief review of the formulation of LPM and the energy-based fatigue criterion are presented. Following this, the energy-based fatigue criterion is implemented in LPM scheme to analysis fatigue crack initiation and propagation. The key idea is to decompose the non-local energy into dilatational and distortional components, and the dilatational and distortional components can be used for the fatigue criterion to determine whether a particle is failure or not. In order to validate the proposed LPM fatigue scheme, fatigue crack propagation simulation from LPM scheme is comparing the experimental results in open literatures. The energy-based fatigue criterion with LPM performs fatigue analysis for bi-phase material. Several conclusions are drawn based on the proposed formulation and the validation results.

5.1 Introduction

Fatigue is a very common failure mode in many mechanical components. However, it is still a challenge to simulate fatigue failure under cyclic loadings. Because the fatigue failure introduces material discontinuity, and the material discontinuity is changing with fatigue crack propagation. Besides, material scientists are making great efforts to understand multiaxial fatigue problems, which involves complex stress states, loading histories and different orientations of fatigue crack.

Finite element method (FEM) is the most widely used approach to model and simulate mechanics-related problems. FEM is based on the partial differential equations in classical continuum mechanics theory. Therefore, it cannot simulate discontinuous problems directly, such as crack growth and multi-phase material interface. One major algorithm in FEM for crack growth simulation is remeshing techniques[1], [102]. However, remeshing techniques bring high computational cost, and it is not easy to apply remeshing techniques in three dimension models[103]. Extended finite element method (XFEM) is another algorithm to solve crack growth problems, which allows crack pass though elements without remeshing[104].

Due to the intrinsic nature, discrete approach is more suitable for problems involving discontinuities, such as fracture/fatigue failure problems. One major group in discrete method is the particle method/lattice method. Among various particle methods, one unique group is the so-called non-local particle methods, such as [40], [105]. Lattice Particle Model (LPM) [53], [56] is a recently developed nonlocal approach that treats material under study as a collection of interacting discrete elements or particles. And each discrete element or particle interacts with neighboring discrete elements or particles up to certain distance. Different from conventional continuum theory, LPM describes the motions of discrete elements or particles using integral differential equations rather than partial differential equations. Thus, LPM doesn't have any spatial singularity related issues even when discontinuities such as cracks exist within the domain of interests. Besides, LPM models crack nucleation by removing the interactions between interacting particles and crack propagates as a natural outcome of this successive interaction removal process [52]. Different from other meshfree methods, such as bond-based peridynamics [106] and lattice spring models[3], [42]. LPM is formulated only using the distance change between particles and doesn't pose any restrictions on material

Poisson's ratio. Materials with arbitrary value of Poisson's ratio can be accurately modeled within LPM framework [53], [56]. The uniqueness of LPM with respect to other meshfree methods is the inclusion of both pair-wise local and multi-body nonlocal potentials in the formulation. The interaction between two interacting particles has contribution from not only the two interacting particles, but also all their neighboring particles [56]. In addition to brittle materials, Wei et al. proposed a systematic formulation for elastoplastic materials for LPM[107], which is a necessary step for the accurate fatigue and fracture simulation.

For multiaxial fatigue modelling, these multiaxial fatigue models can be classified into four categories: stress-based[11], [12], strain-based[13], [14], energy-based[15], [16] and fracture mechanics-based[17]. Stress-based models are mostly used to predict fatigue life for high cycle fatigue. Strain-based models are suitable for low cycle fatigue in which plastic deformation is significant. Critical plane is a well-known approach of fracture mechanics-based models which is based on experimental observation of fatigue crack nucleation growth direction. Many models[18], [19] assume the maximum shear stress range plane as the critical plane which is suitable for ductile failure. Other models assume the maximum normal stress range plane as the critical plane which is mostly suitable for brittle failure[21]–[23]. Several energy-based models[20], [30], [78] using the critical plane concepts are shown to be successful for multiaxial fatigue life prediction under non-proportional loading. It is observed that most critical plane-based approaches ignore the damage contribution from axial stress/strain parallel to the critical plane (in another words, hydrostatic stress/strain components). This approach may be appropriate under uniaxial loadings and tension-torsion loadings but is questionable for biaxial tension-tension loading. Either direction axial stress/strain (e.g., perpendicular or parallel to the critical plane) may or may not be ignored. Extensive multiaxial fatigue models

using the critical plane approach were validated under tension-torsion loading conditions. However, if the loading condition is complicated, such as biaxial tension-tension loadings and hydrostatic loadings, the critical plane approach might be hard to determine the orientation of the critical plane and usually leads to large error of the fatigue life prediction [81]. Wei and Liu developed a universal energy-based multiaxial fatigue formulation which is capable to both tension-torsion and tension-tension loadings[108].

The new multiaxial fatigue criterion proposed by Wei and Liu[109] can be implemented in LPM, because the fatigue criterion is based on distortional and dilatational energy terms. In LPM scheme, the particle and bond fatigue damage can be computed according to distortional and dilatational energy using the new multiaxial fatigue criterion. In particular, integrating the new fatigue criterion, LPM is able to simulate fatigue crack propagation naturally with bonds break, and the fatigue criterion has power to calculate fatigue damage of each particle and bond in LPM.

Based on the above discussion, the study in this paper focuses on fatigue analysis using the multiaxial energy-based fatigue criterion integrating with LPM. In this work, a framework of fatigue damage criterion using LPM based on distortional and dilatational energy terms is proposed to enhance the modeling capability of LPM for fatigue crack initiation and propagation. This energy-based nonlocal yield criterion is consistent with the energy composition of LPM particles. The remainder of this paper is organized as follows: First, a brief review of LPM formulation and the energy-based multiaxial fatigue criterion is presented. LPM parameters in terms of material constants for different lattice structures are provided. Following this, a method is derived to calculate the distortional and dilatational energy terms

in particles and bonds. Next, the fatigue damage criterion is integrated with LPM. Bond energy terms governs the bond fatigue damage and then it used to determine bond states, broken or not. After that, numerical examples of fatigue crack initiation and propagation considering different materials and loading scenarios are modeled using the proposed framework. LPM predictions are compared with experimental results. Bi-phase material fatigue analysis is performed. Discussions and conclusions based on the proposed study are drawn at the end.

5.2 Method

Formulation of LPM

LPM formulation depends on the lattice structure used to discretize the solution domain. Various lattice structures have been employed in LPM, such as triangular and square lattice structures for two-dimensional analyses and simple cubic, body-centered cubic and face-centered cubic lattice structures for three-dimensional analyses. In LPM, a typical particle can interact with neighboring particles and remote particles depending on how many layers of particles is involved in the interaction distance. For a given interaction distance, unit cell is identified for each type of neighbor. And the potential energy for a particle is the summation of the energy associated with these unit cells. For each unit cell, the stored energy can be separated into two parts, a local pairwise energy corresponding to the stretch between two particles and a non-local multi-body energy associated with its volume change. For particle *I*, the stored energy in one of its unit cell can be written as

$$U_I = U_I^{local} + U_I^{nonlocal} \tag{5.1}$$

with the local energy U_I^{local} can be expressed in terms of distance change between particle *I* and its neighbors for current unit cell as

$$U_I^{local} = \frac{1}{2}\sum_{J=1}^{N_I} k_{IJ}\left(\delta l_{IJ}\right)^2 \tag{5.2}$$

and the nonlocal energy $U_I^{nonlocal}$ for current unit cell is calculated as

$$U_I^{nonlocal} = \frac{1}{2}T_I\left(\sum_{J=1}^{N_I}\delta l_{IJ}\right)^2 \tag{5.3}$$

In Eqs. (5.2) and (5.3), k_{IJ} is the local parameter for each pair of interacting particles, T_I is the nonlocal parameter, δl_{IJ} is the distance change between particle *I* and its neighbor *J*, N_I is the total number of neighboring particles interacting with particle *I* for current unit cell.

Equating the energy of a particle in LPM to its continuum equivalent, the material stiffness tensor can be obtained by theory of hyperelasticity as

$$C_{ijkl} = \frac{1}{V_I}\frac{\partial^2 \sum U_I}{\partial\varepsilon_{ij}\partial\varepsilon_{kl}} \tag{5.4}$$

where ε_{ij} is the strain tensor at a particle.

For small deformation, the distance change between particles can be mapped to the strain tensor using following relationship

$$\varepsilon_{IJ} = \frac{\delta l_{IJ}}{L_{IJ}} = \varepsilon_{ij} n_i n_j \tag{5.5}$$

where L_{IJ} is the initial distance between particle *I* and its neighbor *J*, n_i and n_j are the components of unit vector connecting particle *I* and it neighbor *J*.

LPM parameters can be determined by comparing the material stiffness tensor given in Eq. (5.4) with generalized Hooke's relationship. Certain constraint(s) needs to be imposed between LPM parameters for different neighbors, such as k and T should be the same for the same type of neighbors for an isotropic material.

Given the LPM parameters, the interaction between particle *I* and its neighbor *J* can be calculated by differentiating the total stored energy with respect to its distance change as

$$\mathbf{f}_{IJ} = \frac{\partial U_I}{\partial \delta l_{IJ}} \mathbf{n}_{IJ} \tag{5.6}$$

In LPM, the equation of motion for a particle *I* at time t is given by

$$m_I \ddot{\mathbf{u}}_I(t) = \sum_{J=1}^{N_I} \mathbf{f}_{IJ}(t) + \mathbf{b}_I(t) \qquad \forall (I,t) \in \Omega \times (0,\tau) \tag{5.7}$$

where m is mass, $\mathbf{u}(t)$ is the displacement vector, $\mathbf{f}_{IJ}(t)$ is the interaction force between particles *I* and *J*, and $\mathbf{b}_I(t)$ is external force vector.

Energy-based damage parameter and failure criterion

Wei and Liu proposed a new fatigue criterion based on Distortional and dilatational energy terms[109], which can be implemented in the LPM framework. The new fatigue criterion considering contributions of equivalent tensile energy term, torsional energy term, and hydrostatic energy term is proposed as

$$\frac{W^{ten}}{W_{-1}^{ten}} + \frac{W^{tor}}{W_{-1}^{tor}} + \frac{W^{H}}{W_{-1}^{H}} \geq 1 \tag{5.8}$$

where W^{ten}, W^{tor}, and W^{H} are the equivalent cyclic tensile energy, equivalent cyclic torsional energy, and equivalent cyclic hydrostatic energy, respectively. W_{-1}^{ten}, W_{-1}^{tor}, and W_{-1}^{H} are tensile, torsional, and hydrostatic fatigue limit in terms of energy, respectively. Fatigue limit under hydrostatic stress amplitude is hard to measure, so a ratio *k* parameter is used with the fatigue under uniaxial tensile loading as

$$W_{-1}^{H} = \frac{W_{-1}^{ten}}{k} \tag{5.9}$$

Substituting Eq. (5.8) to Eq. (5.9), one can obtain

$$\frac{W^{ten}}{W_{-1}^{ten}} + \frac{W^{tor}}{W_{-1}^{tor}} + k\frac{W^{H}}{W_{-1}^{ten}} \geq 1 \tag{5.10}$$

the parameter k can be solved as:

$$k = \frac{(r)^2}{3(1-2\nu)} \tag{5.11}$$

where r is the ratio of the yield strength and ultimate strength. The parameter k is a material constant related to the Poisson's ratio and yield-to-ultimate strength ratio.

W^{ten}, W^{tor}, and W^{H} can be calculated based on distortional and dilatational energy terms. A parameter *t,* the ratio of distortional and dilatational energy, is introduced before calculating W^{ten}, W^{tor}, and W^{H} . The ratio t of distortional and dilatational energy under tensile loading is

$$t = \frac{W^{dis}}{W^{dil}} = \frac{2+2\nu}{1-2\nu} \tag{5.12}$$

As shown in Eq. (5.12), the ratio t is a constant, irrespective of the applied loading levels. For other multiaxial loading cases, this ratio is not a constant and depends on the loading. For larger value of t ($t = \frac{W^{dis}}{W^{dil}} > \frac{2+2\nu}{1-2\nu}$), it indicates larger contribution from distortional energy. The extreme value is infinity which corresponds to the pure torsional loading (i.e., W^{dil}=0). For smaller value of t ($t = \frac{W^{dis}}{W^{dil}} < \frac{2+2\nu}{1-2\nu}$), it indicates smaller contribution from distortional energy. The extreme value is zero which corresponds to the hydrostatic loading (i.e., W^{dil}=0). It is interesting to see that the three special values 0, $\frac{2+2\nu}{1-2\nu}$, and $+inf$ are three special loading conditions (e.g., hydrostatic loading, pure tensile loading, and pure torsional loading). The three special values divide the t range into two segments: one segment can be treated as a combined tensile + torsional loading and the other can be treated as the combined tensile + hydrostatic loading.

Based on this representation, we proposed the following concept to develop a multiaxial fatigue model. First, calculate the equivalent tensile energy by maximizing the extraction of proportional distortional energy and dilatational energy from the system. Mathematically,

$$W^{ten} = \min\{\frac{3}{1-2\nu}W^{dil}, \frac{3}{2+2\nu}W^{dis}\} \tag{5.13}$$

After this extraction, there may be remaining energy (either dilatational energy or distortional energy). The equivalent torsional energy is the remaining distortional energy, and the equivalent hydrostatic energy is the remaining dilatational energy.

As a summary, the calculation of equivalent energy terms is summarized in Table 1. In practice, the ratio of dilatational and distortional *t*, is calculated first. Table 1 is then used to find equivalent energy terms and substituted to proposed multiaxial fatigue model (Eq. (5.8)) for fatigue analysis.

Table 1 Summary of the equivalent energy term calculation in the proposed model

t	$t = \frac{W^{dis}}{W^{dil}} \geq \frac{2+2\nu}{1-2\nu}$	$t = \frac{W^{dis}}{W^{dil}} \leq \frac{2+2\nu}{1-2\nu}$
W^{ten}	$W^{ten} = \frac{3}{1-2\nu}W^{dil}$	$W^{ten} = \frac{3}{2+2\nu}W^{dis}$
W^{tor}	$W^{tor} = W^{dis} - tW^{dil}$	$W^{tor} = 0$
W^{H}	$W^{H} = 0$	$W^{H} = W^{dil} - \frac{W^{dis}}{t}$
Failure criterion	$\frac{W^{ten}}{W_{-1}^{ten}} + \frac{W^{tor}}{W_{-1}^{tor}} \geq 1$	$\frac{W^{tor}}{W_{-1}^{tor}} + k\frac{W^{H}}{W_{-1}^{ten}} \geq 1$

The details of the fatigue criterion derivation can be seen in Ref[109].

For finite fatigue life prediction, the damage parameter should be correlated with the life (i.e., number of loading cycles). Eq. (5.10) can be rewritten as

$$W^{ten} + sW^{tor} + kW^{H} \geq W_{-1}^{ten} \tag{5.14}$$

where $s = \frac{W_{-1}^{ten}}{W_{-1}^{tor}}$. The left-hand side of the equation can be treated as the effective energy term W_{eff}^{ten} and can be used to correlate with the fatigue life using the uniaxial energy–N curve $f(N_f)$ as

$$W_{eff}^{ten} = W^{ten} + sW^{tor} + kW^{H} = W_{N_f}^{ten} = f(N_f) \tag{5.15}$$

where the ratio s is redefined as $s = \frac{W_{N_f}^{ten}}{W_{N_f}^{tor}}$. N_f is the certain cycle number to failure. The W_{-1}^{ten} and W_{-1}^{ten} are replaced by $W_{N_f}^{ten}$ and $W_{N_f}^{tor}$, respectively, which are fatigue strengths at finite fatigue life N_f. Eq. (5.15) is a nonlinear equation about N_f and numerical method can be used to solve for N_f [28]–[30].

5.3 Implementation

The aforementioned energy-based criterion can be implemented in LPM scheme to analysis material fatigue problems. In particular, the fatigue criterion used is bond-based, in which the critical energy on is defined. Once the critical energy is reached by a bond during the simulation step, the bond is considered broken and removed from future simulation steps. The entire fatigue process can be tracked by the bond breaking process. Because the energy fatigue criterion is based on the distortional and dilatational energy components, we first calculate the energy components on bonds, and then use the fatigue criterion to determine the bond fatigue damage.

Bond energy components calculation in LPM

For any particle *I*, the interaction between particle *I* and its neighbor *J*, i.e., force of bond *IJ*, is

$$f_{IJ} = k\delta l_{IJ} + T\sum_{M=1}^{N_I} \delta l_{IM} \tag{5.16}$$

The increment formulation at the n^{th} loading step is

$$\Delta f_{IJ}^{n} = k\Delta\delta l_{IJ}^{n} + T\sum_{M=1}^{N_I} \Delta\delta l_{IM}^{n} \tag{5.17}$$

where $\Delta\delta l_{IJ}^{n} = \delta l_{IJ}^{n} - \delta l_{IJ}^{n-1}$.

The interaction between particle *I* and its neighbor *J* at the n^{th} loading step can be rewritten as

$$f_{IJ}^{n} = f_{IJ}^{n-1} + \Delta f_{IJ}^{n} \tag{5.18}$$

Thus, the energy increment for particle *I* at the n^{th} loading step can be calculated as

$$\Delta \mathrm{U}_{I}^{n} = \sum_{M=1}^{N_I} \left(f_{IM}^{n} \times \Delta\delta l_{IM}^{n} \right) \tag{5.19}$$

and the total energy at particle *I* at the n^{th} loading step is

$$\mathrm{U}_{I}^{n} = \mathrm{U}_{I}^{n-1} + \Delta \mathrm{U}_{I}^{n} \tag{5.20}$$

The total energy in Eq. (5.20) can be decomposed into dilatational and distortional parts which are correspondent to volume change and shape change, respectively. Due to the regularity of unit cells for each particle, the volume change can be calculated in terms of average bond length change. And the average bond length change is

$$\overline{\delta l_I} = \frac{1}{N_I}\sum_{M=1}^{N_I} \delta l_{IM} \tag{5.21}$$

The shape change of each unit cell is $\delta l_{IJ} - \overline{\delta l_I}$. Therefore, the distortional energy can be obtained by subtracting the volumetric change portion from Eq. (5.21) as

$$U_I^{dis} = \frac{1}{2} k_I \sum_{J=1}^{N_I} \left(\delta l_{IJ} - \overline{\delta l_I} \right)^2 \tag{5.22}$$

Thus, the force increment associated with this distortion energy can be expressed as

$$\Delta f_{IJ}^{dis,n} = k \left(\Delta \delta l_{IJ}^n - \Delta \overline{\delta l_{IJ}^n} \right) \tag{5.23}$$

Similar to above process, the bond force between particle *I* and *J* associated with shape change at the nth loading step and the distortional energy of particle *I* can be expressed as

$$f_{IJ}^{dis,n} = f_{IJ}^{dis,n-1} + \Delta f_{IJ}^{dis,n} \tag{5.24}$$

$$\Delta \mathrm{U}_I^{dis,n} = \sum \left(f_{IM}^{dis,n} \times \Delta \delta l_{IM}^{dis,n} \right) \tag{5.25}$$

$$\mathrm{U}_I^{dis,n} = \mathrm{U}_I^{dis,n-1} + \Delta \mathrm{U}_I^{dis,n} \tag{5.26}$$

The bond distortional energy between particle *I* and *J* at the nth loading step and the total distortional energy has similar process as

$$\Delta \mathrm{U}_{IJ}^{dis,n} = f_{IJ}^{dis,n} \times \Delta \delta l_{IJ}^{dis,n} \tag{5.27}$$

$$\mathrm{U}_{IJ}^{dis,n} = \mathrm{U}_{IJ}^{dis,n-1} + \Delta \mathrm{U}_{IJ}^{dis,n} \tag{5.28}$$

The bond dilatational energy is associated the volume bond stretch as

$$\Delta \mathrm{U}_{IJ}^{dil,n} = f_{IJ}^{dil,n} \times \Delta \delta l_{IJ}^{dil,n} \tag{5.29}$$

$$\mathrm{U}_{IJ}^{dil,n} = \mathrm{U}_{IJ}^{dil,n-1} + \Delta \mathrm{U}_{IJ}^{dil,n} \tag{5.30}$$

Bond fatigue damage calculation

The bond fatigue damage can be computed after we obtained the bond energy components. Following the process of the energy-based fatigue criterion, first the parameter *t* of the bond between particle *I* and *J*, the ratio of distortional and dilatational energy, is calculated as

$$t_{IJ} = \frac{U_{IJ}^{dis}}{U_{IJ}^{dil}} \tag{5.31}$$

According to Table 1, the parameter t is used to find the suitable equivalent tensile, torsional and hydrostatic energies on the bond. The effective tensile energy, which is determined by these three energies, is used to solve the bond fatigue life as

$$(U_{eff}^{ten})_{IJ} = (U^{ten})_{IJ} + s(U^{tor})_{IJ} + k(U^{H})_{IJ} = U_{N_f}^{ten} = f(N_f) \qquad (5.32)$$

LPM process for fatigue simulation with the energy-based fatigue criterion

Due to material fatigue often involves a large number of loading cycles in range from thousands to millions, we divide loading cycles to several segments, which have corresponding cycle numbers N. We assume that bonds are only broken at the end of each segment, i.e., we simulate one cycle load for the ith segment, and the ith iteration of the ith segment in LPM is equivalent to applying N cycles loading. The number of loading cycles N is set to 1000 in this study. The bond fatigue damage is computed in the end of each segment iteration. If the damage is greater than 1, the bond is broken and the particles-bonds system in LPM is updated for the next segment iteration. The scheme detail of LPM for fatigue is illustrated using a flowchart in Fig. 5-1. The bond fatigue damage is calculated once in each segment. Fatigue failure can be defined as the critical number of particles involving bond breakage or critical crack length.

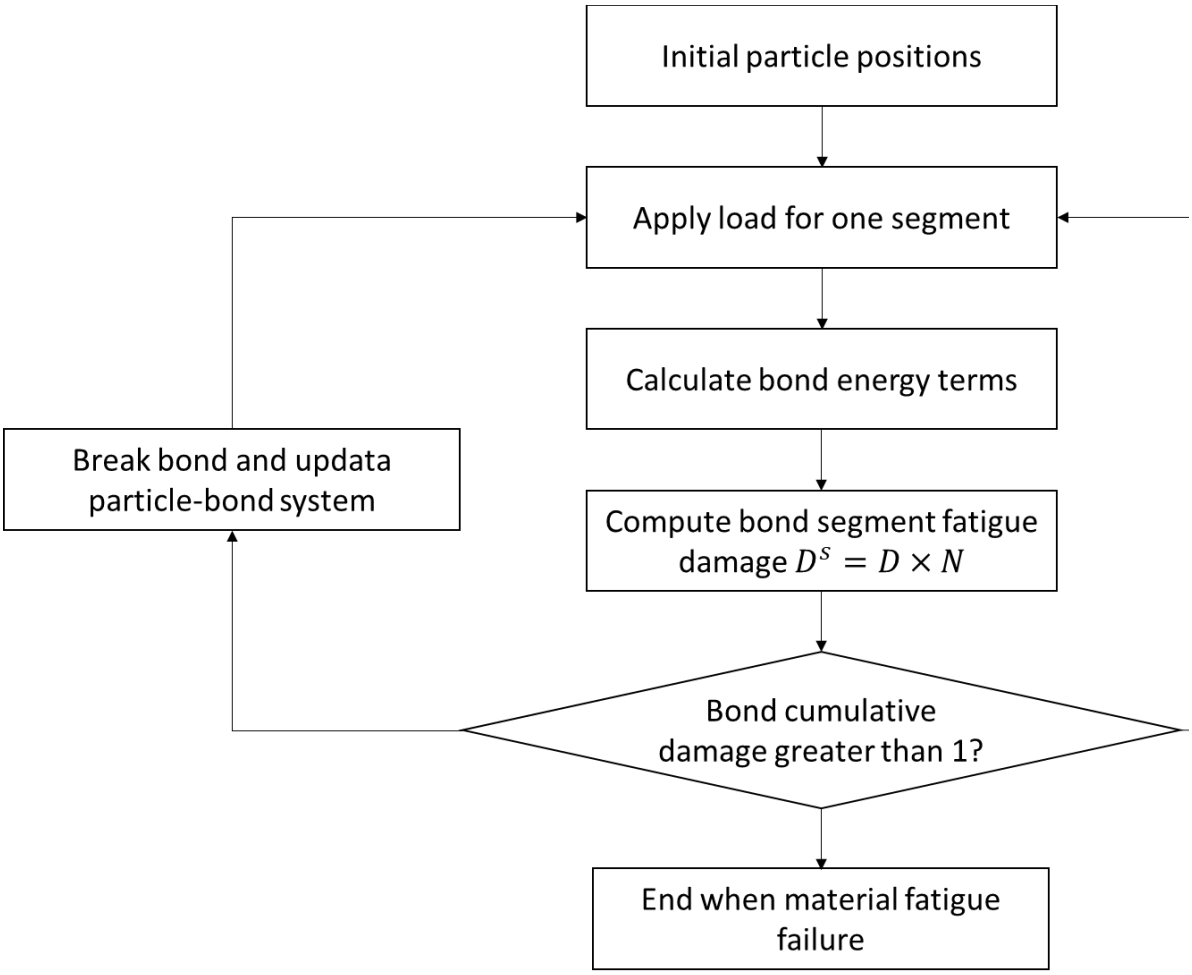

Figure 0-27Flowchart of Fatigue Simulation in LPM Scheme

5.4 Numerical Examples

In this section, several benchmark elastoplastic problems are modeled using LPM with the energy-based multiaxial fatigue criterion. In order to obtain the static solution, the Atomic-scale Finite Element Method (AFEM) [58] is used as an implicit solution scheme. For all the examples in this section, the simple cubic lattice structure is used to discretize the solution domain.

Fatigue crack propagation

In this example, we further demonstrate the modeling capability of the energy-based multiaxial fatigue criterion for fatigue crack simulation. Material used in this section is Aluminum 7075 with Young's modulus $E = 70$ GPa , Poisson's ratio $v = 0.32$. The specimen has dimension of 0.01x0.01x0.001 m. The initial crack is 0.002m. The top left edge is fixed in all three directions. Uniformly distributed cyclic tensile loadings from 0 kN to 0.5 kN are applied on the top and bottom surfaces in the y and negative y directions, respectively. The load ratio R = 0. Fig.6 (a) shows the geometry of the specimen with an initial crack. The red particles indicate the initial crack. Fig. 5-2 (b) shows the crack growth under the applied cyclic loading.

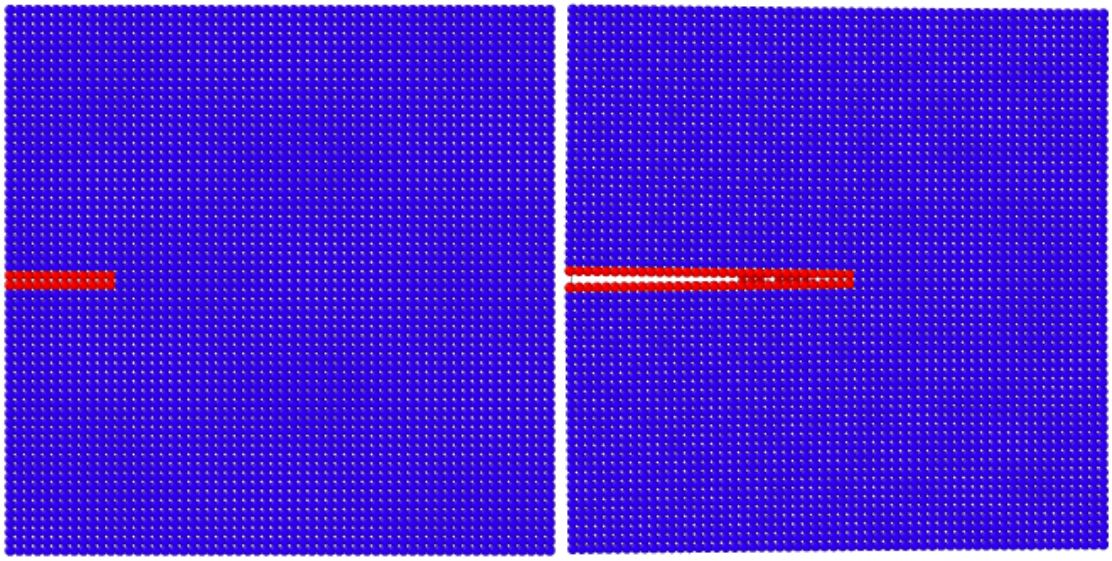

Figure 0-28 Snap Shots of the Fatigue Crack Propagation

In this example, the Paris law curve of the crack growth rate and the range of stress intensity factor is compared with experimental data. The experimental data are from the open

literature[110]. The comparison between the LPM results and the experimental data is shown in Fig. 5-3.

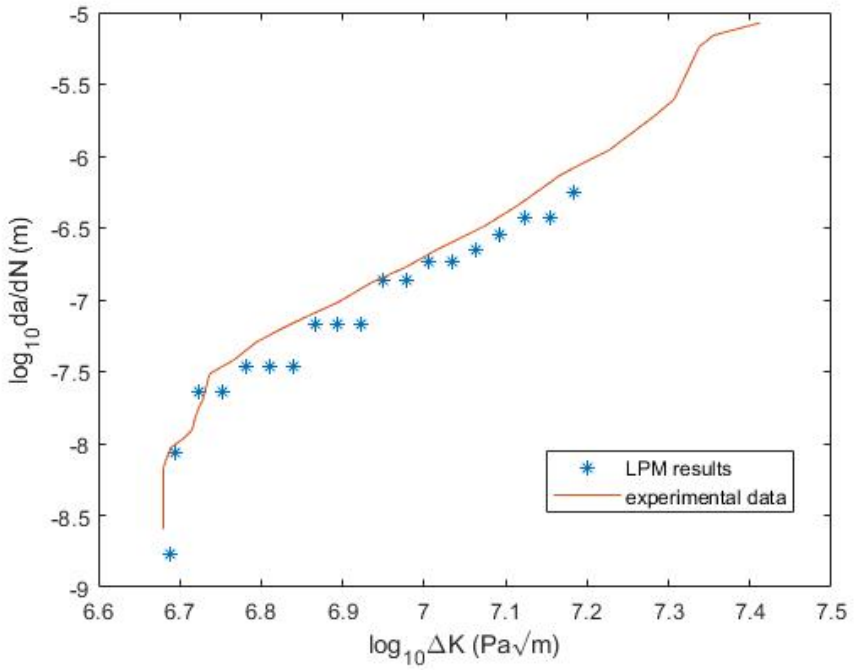

Figure 0-29 Comparison of Fatigue Crack Growth Rate

LPM simulation curve is matched with the experimental Paris law curve in Fig. 5-3 as expected. It validates that the energy-based multiaxial criterion integrated with LPM can simulate the fatigue crack propagation.

Fatigue cracks of composites

In this section, bi-phase materials fatigue damage is studied to demonstrate the LPM has the capability of complex material and structural fatigue analysis. It is hard to find experimental results of bi-phase material fatigue damage in open literature. In the future, if experimental data of such complex material is available, the LPM simulation results will be compared and validated with it. The purpose of this section is to show the flexibility of the LPM for complex

material in fatigue analysis. There is an assumption used in this section that the properties of the interface bonds taken as the arithmetic average of the two different material phases.

The microstructure of statistical bi-phase materials can be modeled by the following random field [111] which is obviously non-Gaussian,

$$I(\boldsymbol{x},\theta)=\begin{cases}0, & if\ the\ material\ at\ \boldsymbol{x}\ is\ in\ black\ phase\\ 1, & if\ the\ material\ at\ \boldsymbol{x}\ is\ in\ white\ phase\end{cases} \tag{5.33}$$

This non-Gaussian random field is widely simulated using the translation theory based on Karhunen–Loève expansion [112], which represents the second-order statistics. A general random field can be expressed as,

$$\widehat{w}(x,\theta)=\overline{w}(x)+\sum_{i=1}^{M}\lambda_i f_i(x)\xi_i \tag{5.34}$$

where, λ_i and $f_i(\mathbf{x})$ are eigen pairs solved form the second Fredholm integral equation,

$$\int_D C(x_1,x_2)f_i(x_1)dx_1=\lambda_i f_i(x_1) \tag{5.35}$$

where, $C(x_1,x_2)$ is the covariance function. The covariance function of the real material microstructure can be characterized by the two-point correlation function [113]. ξ_i contains a set of uncorrelated random variables with zero mean and unit variance. For fixed M terms, it has been proved that the K-L approximation is optimal among series expansion methods with respect to the global mean square error. For the Gaussian random field, ξ_i are independent standard normal variables. But for non-Gaussian cases, the distribution of ξ_i is non-Gaussian and unknown. The main idea is to find an underlying Gaussian random field that can match

the statistics of the target random field after a nonlinear mapping. The expression of a general random field is given as,

$$w(\boldsymbol{x},\theta) = T(G(\boldsymbol{x},\theta)) \tag{5.36}$$

where, $F_N(\cdot)$ represents the CDF of the target marginal distribution. $T(\cdot) = F_N^{-1}\{\Phi(\cdot)\}$ is the nonlinear translation form the underlying Gaussian distribution to the target non-Gaussian distribution. More specifically, the used nonlinear translation is defined as,

$$\begin{aligned} &T(G(\boldsymbol{x})) \\ &= \begin{cases} 0, & if\ G(\boldsymbol{x}) \le \Phi^{-1}(p_0), the\ material\ at\ x\ is\ in\ black\ phase \\ 1, & if\ G(\boldsymbol{x}) > \Phi^{-1}(p_0), the\ material\ at\ x\ is\ in\ white\ phase \end{cases} \end{aligned} \tag{5.37}$$

where, p_0 denotes the volume fraction of material in black phase. Determining the optimal covariance function of the underlying Gaussian random field follows the iterative approximation algorithm in [114]. The major benefit of reconstructing microstructure by non-Gaussian random fields is the high efficiency. And it can also satisfy the first and second-order statistics.

Bi-phase material samples are generated with two different materials: Aluminum 7075 (red particles in Fig. 5-4) and A533B steel (blue particles in Fig. 5-4). The geometry has dimension of 0.01x0.01x0.001m. Uniformly distributed cyclic tensile loadings from 0 kN to 0.8 kN are applied on the top and bottom surfaces in the y and negative y directions, respectively with the load ratio R = 0. Fig. 5-4 (a) show the microstructures of 3 bi-phase materials before cyclic loading. There is no initial crack. Fatigue crack initiation are presented as white particles shown in Fig. 5-4 (b). Fig. 4 (c) shows the fatigue failure pattern after fatigue crack

propagation. Since the samples are in three-dimensions, we rise the transparency of particles to show inner fatigue crack patterns.

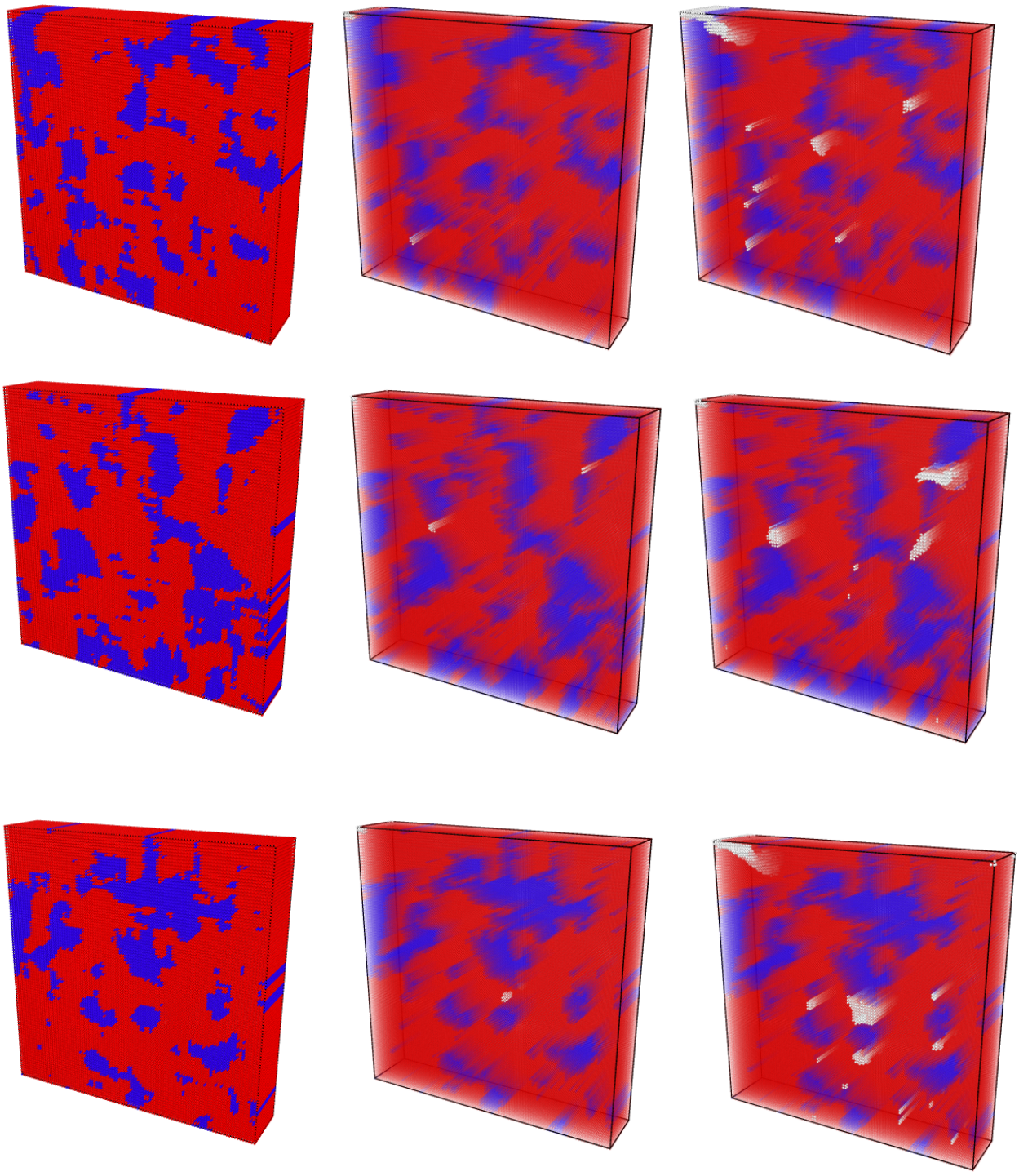

(a) (b) (c)

Figure 0-30 Fatigue Crack Initiation and Propagation in Bi-phase Material

It can be seen that the crack initiations occur near material discontinuities and force boundaries as expected. For the fatigue crack propagation, most fatigue failure particles are Aluminum 7075, which has smaller fatigue strength than A533B steel.

5.4 Discussion and Conclusions

Lattice Particle Method (LPM) is a discontinuous approach for modeling of solid materials. It removes the restriction of Poisson's ratio in traditional lattice spring models by introducing only axial interactions among discrete particles. The fatigue criterion based on distortional and dilatational energy can be integrated with LPM to do fatigue analysis. By comparing LPM simulation results with experimental data, several conclusions based on this study are concluded as follows.

(1) For fatigue crack propagation, LPM predictions have a good agreement with experimental Paris law curve. The fatigue criterion can predict fatigue crack propagation with discrete computational mechanics models;

(2) Bi-phase material fatigue analysis shows the potential of LPM for complex material and structural fatigue simulation.

The energy-based fatigue criterion is capable of modeling fatigue crack initiation and propagation using LPM. The current study was based on simple cubic packing. For other 3D packing patterns, similar fatigue criterion can also be proposed but may need further validation. Future work is to apply the developed scheme to model fatigue and fracture of more complex materials.

6. FRACTURE ANALYSIS FOR MICROSTRUCTURES USING DEEP NEURAL NETWORKS AND LATTICE PARTICLE METHOD

6.1 Introduction

Material fracture failure is a catastrophic issue for many practical engineering structures and components. Accurate fracture prediction is necessary to ensure the safety of these structures and components. The finite element method (FEM) is the most widely used approach for material mechanical modelling. Since FEM is based on partial differential equations, it may be hard to solve problems involving spatial discontinuities, such as fracture and material interface. Lattice particle method (LPM) is a recently developed discontinuous approach[53]. It treats material under study as a collection of interacting discrete elements or particles. And each discrete element or particle interacts with neighbour discrete elements or particles up to a certain distance. Due to the intrinsic characteristics of integro-differential governing equations in LPM, it is naturally suitable for discontinuous problems[10]. The development of LPM initially have been focused on elastic material[52], [53]. LPM has been demonstrated the capability of brittle material fracture simulation[10]. Chen et al. has extended LPM for simulations of heterogenous materials[115], composite materials[116]. Wei et al. proposed a rigorous formulation of LPM for ductile materials simulation[107].

For material fracture simulation, there are two stages, elastic deformation and crack propagation. The elastic deformation is linear process, while crack propagation is a nonlinear process, because material stiffness is decreasing during fracture. An integration of incremental method with LPM is needed to solve nonlinear problems, i.e., LPM tracks nonlinear deformation using many time steps, which involving a lot of iterations. Therefore, the

incremental method brings high computational cost. Besides, in order to obtain accurate fracture simulation, a large number of particles is required in LPM, which makes the LPM simulation time-consuming. To reduce computational time, deep learning is considered with LPM in this paper. In the past decade, deep learning has been successfully used in many complex tasks, such as computer vision[117], natural language processing (NLP)[118], and system control[119]. Deep learning also has been used by materials and mechanics scientist for material reconstruction[120] and material property prediction[121], [122]. For material fracture problems, most researchers have applied deep learning to predict fracture parameters, such as fracture energy[123] and stress intensity factor (SIF)[124]. Few works have been done to predict fracture patterns using deep learning. To authors' knowledge, only research done by Hsu et al.[125] and Kim et al.[126] is related to fracture patterns prediction, which includes fracture's spatial information. Hsu et al. simulated fracture crack propagation for both mode I and mode II loading conditions with an initial crack. Kim et al. predicted collision fracture patterns on a disk. Both these two works used convolutional neural networks (CNNs), an algorithm of deep learning suitable for images processing. However, for arbitrary geometries and loading conditions, a deep learning model based on CNNs is still lacking.

Inspired by the above-mentioned works, an integration of an efficient deep learning model and LPM is proposed in this paper to predict fracture pattern for arbitrary geometries and loading conditions. LPM and deep learning model has different advantages for different stages in fracture simulations. Comparing LPM, a deep learning model is more efficient which is suitable for nonlinear crack simulation. For the linear elastic stage, LPM has better accuracy, and the computational cost is not high for the linear stage. Thus, we combine LPM and a proposed deep learning model for the linear stage and nonlinear stage, respectively. Figure 6-

1 shows an example of the aforementioned linear-nonlinear process of material stress-strain curve to illustrate the proposed computational framework. It should be noticed that the geometry and loading conditions in our study are more complex than this example. LPM is used here to 1) simulate material elastic deformation in linear stage as input for the proposed deep learning model; 2) generate a training dataset of fracture pattern. With this integration, computational accuracy and efficiency are both considered.

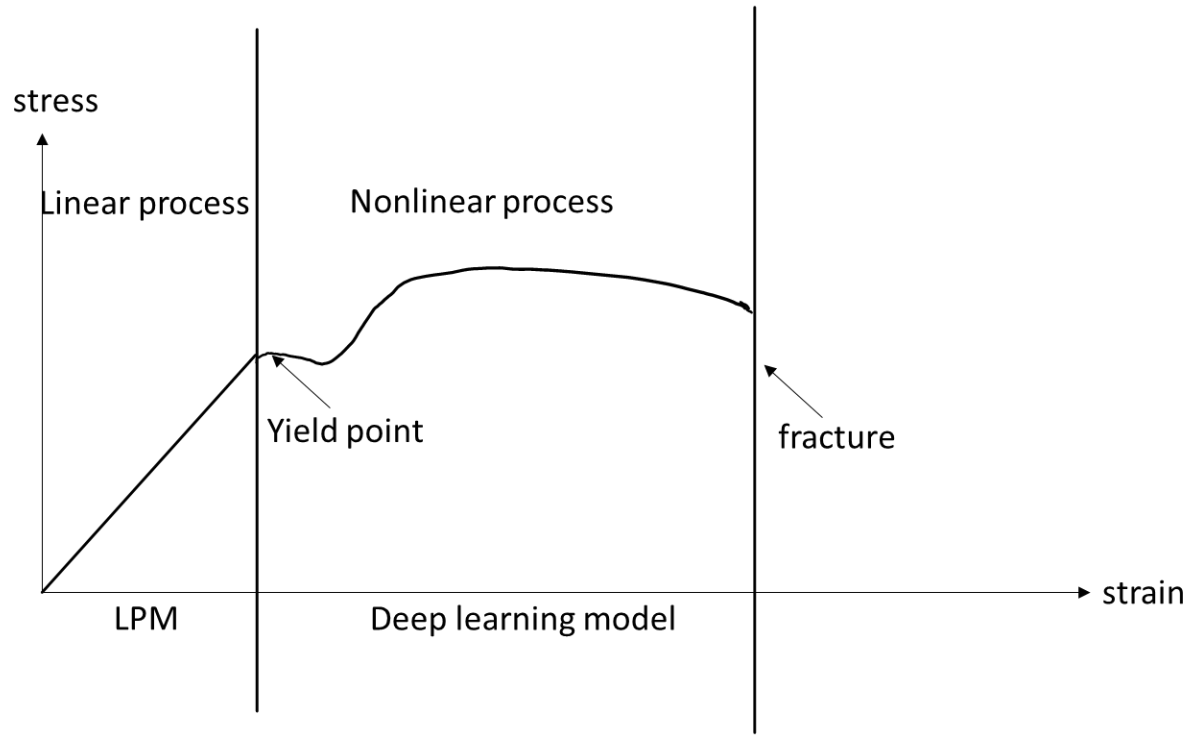

Figure 0-31 Illustration of Linear-nonlinear Process and the Proposed Framework.

This chapter is organized as follows. First, a brief review of LPM formulation and a CNNs algorithm is present in Section 2. Following this, the proposed model of combining LPM and a deep neural network is developed in Section 3. Next, the details of model implementation and experimental results are in Section 4. In Section 5, some conclusions are drawn.

6.2 Related Works

The investment in this paper proposes a computational framework for the process that involves a linear stage at the beginning and a nonlinear stage following the linear stage. Brittle material fracture belongs to this linear-nonlinear process. Under a specific loading, the deformation of the material is linear elastic before an occurrence of crack nucleation, and then with crack propagation, the deformation becomes nonlinear until fracture failure. It is demonstrated that LPM has the capacity to simulate both linear and nonlinear material behaviors[52], [107]. For the nonlinear simulation, incremental method is integrated with LPM to track the nonlinear process. The incremental method brings a large number of iterations; therefore, the nonlinear simulation is time-consuming. Here we propose a surrogate way to utilize a deep learning model to replace LPM for nonlinear simulation, which allows us to predict the fracture process efficiently. Comparing the deep learning model and LPM, the deep learning model has lower computational cost, however, the simulation of LPM is more accurate. Thus, considering both computational efficiency and accuracy, we combine LPM and the deep learning model for linear elastic stage and nonlinear fracture stage, respectively.

Lattice particle method

LPM formulation depends on the lattice structure used to discretize the solution domain. Various lattice structures have been employed in LPM, such as triangular and square lattice structures for two-dimensional analysis, and simple cubic, body-centered cubic and face-centered cubic lattice structures for three-dimensional analysis, as shown in Figure 6-2.

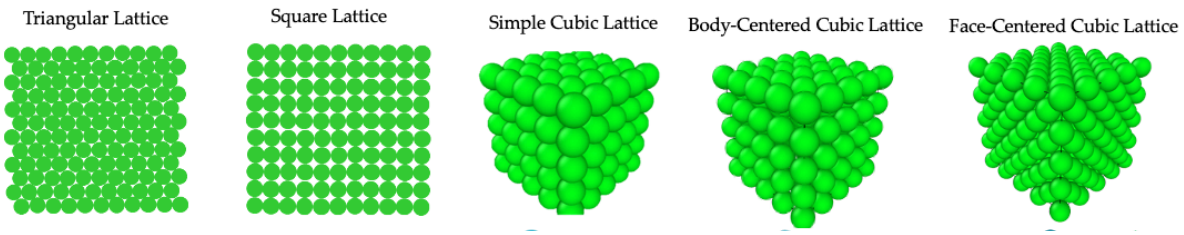

Figure 0-32 LPM Lattice Packings

In LPM, a typical particle can interact with neighboring particles and remote particles depending on how many layers of particles is involved in the interaction distance. For a given interaction distance, unit cell is identified for each type of neighbor. And the potential energy for a particle is the summation of the energy associated with these unit cells. For each unit cell, the stored energy can be separated into two parts, a local pairwise energy corresponding to the stretch between two particles and a non-local multi-body energy associated with its volume change. The details of the LPM theory can be found in Chapter 2 and Refs[56].

Convolution neural networks and fully convolution networks

A L-layer deep neural network can be expressed as a function as,

$$y(x \mid W) = \sigma^{L}(W^{L}, ..., \sigma^{2}(W^{2}, \sigma^{1}(W^{1}, x))) \tag{6.8}$$

with parameters W = $\{W^1, W^2, ..., W^L\}$ and input x. The function σ is called activation function, which acts on all components of the input vector. During the training phase, the network weights are determined by minimizing the difference between network output and observations. It is found that, given enough nodes, neural networks with non-linear activation function have the potential to approximate any complicated functions[127].

CNNs, an algorithm of deep neural networks, has achieved a great success on image learning tasks in the computer vision domain. The strength of feature extraction gives CNNs

enormous computational power when dealing with domain specific features. While the sharing of network parameters reduces the computational complexity without compromising feature extraction capabilities.

The development of CNNs originated from the competition of handwritten digit recognition in the early 90s. LeNet[128] is one of the pioneering frameworks but the following research standstill for a while due to the computing power of computer hardware. AlexNet[117] is credited as the first work in the field of computer vision with the significant advancement of computational capabilities and GPUs. AlexNet is much bigger than LeNet in considering the network size and achieved great improvement on image classification accuracy. The next milestone work is GoogLeNet[129] architecture namely Inception-v1 that gives more network utilization with fewer parameters than AlexNet. Further refinement of the Inception model led to the newer version[130]–[132] with the use of batch normalization. The universal use of a small 3x3 convolutional filter was first introduced in VGGNet[133] to deal with the parameter exploding issue when adding the depth factor in CNNs. Deep residual learning[134] is another milestone work where the layers can learn residual functions with respect to inputs. Deep residual learning is proved that is especially useful when training of much deeper networks with much performance gain.

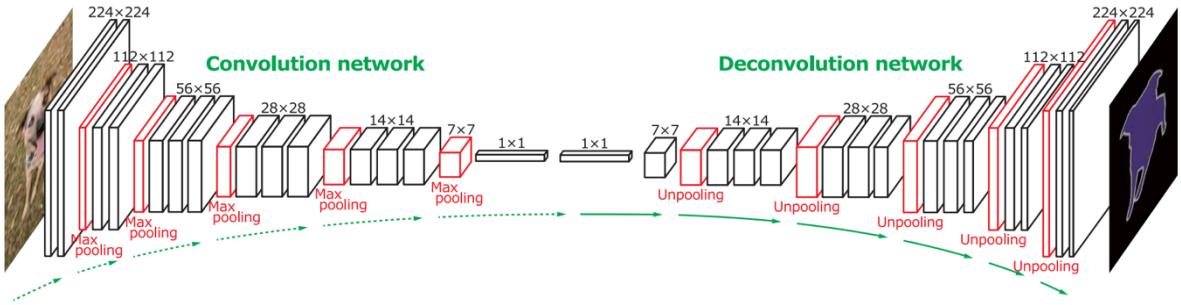

Figure 0-33 Structure of FCN. Source*: Figure adopt from the Ref*[135]

In our deep learning model, we adopt a fully convolution network (FCN)-based model[136], a special type of convolution neural network (CNN), that only contains convolution layers. CNNs are investigated to replace some fully connection layers in a typical deep neural network with convolution layers, which take advantage of visual imagery[135]. An architecture of an FCN is shown in Figure 6-3. It can be seen that the outputs of FCNs are pixelwise labeled images with same revolution of inputs. This specialty allows FCNs to commonly be applied to semantic segmentation of images.

5.3 Proposed Models

Problem statement

Fracture propagation is stochastic with random state of microstructure. The fracture pattern is often considered highly relating with material microstructures and loading conditions. Thus, our goal is to predict fracture pattern efficiently with given material microstructures and loading conditions. In this paper, we investigate fracture patterns in two-dimensional representative volume elements (RVEs), with the dimension of 0.01m by 0.01m. Figure 6-4 shows the loading conditions in this study. Top and left surfaces are fixed along vertical and horizontal axes, respectively, and the bottom and right surfaces are applied with uniform distributed displacement-controlled loads in downward and rightward directions, respectively. The ratio of these two loads magnitudes is random, which introduces randomness from loading. For LPM simulation, specimens are loaded slowly such that quasi-static assumption is valid.

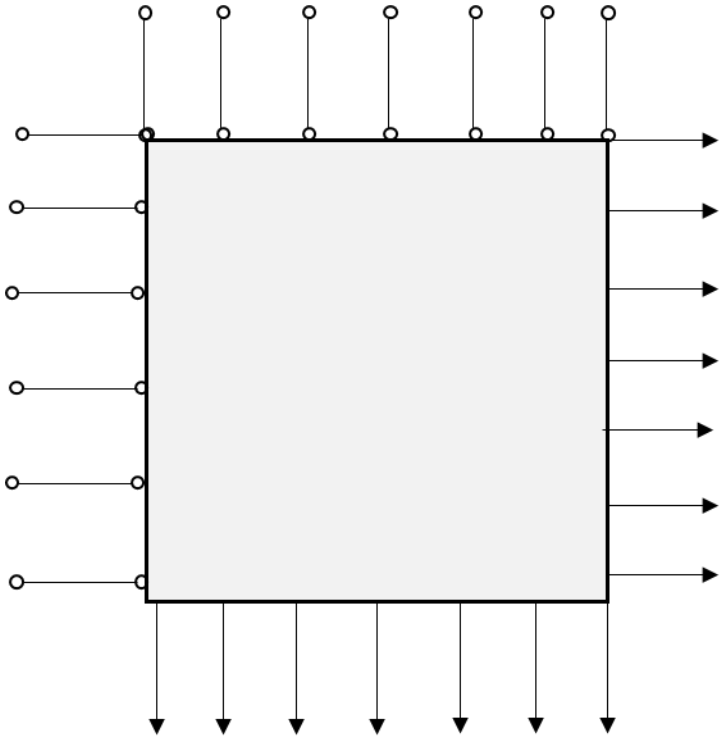

Figure 0-34 Loading Condition of RVEs

Some stochastic microstructures and corresponding fracture patterns under uniaxial loads are shown in Figure 6-5. Red circles in microstructures represent holes in RVEs. It can be seen that positions of holes are stochastic and the total number of holes in one RVE is a constant of 16. We assign the holes radius at 0.0006m and avoid overlap of holes for RVEs generation. Fracture is represented in red color. We aim to predict fracture patterns using LPM and a deep neural network with a specific microstructure and a loading condition.

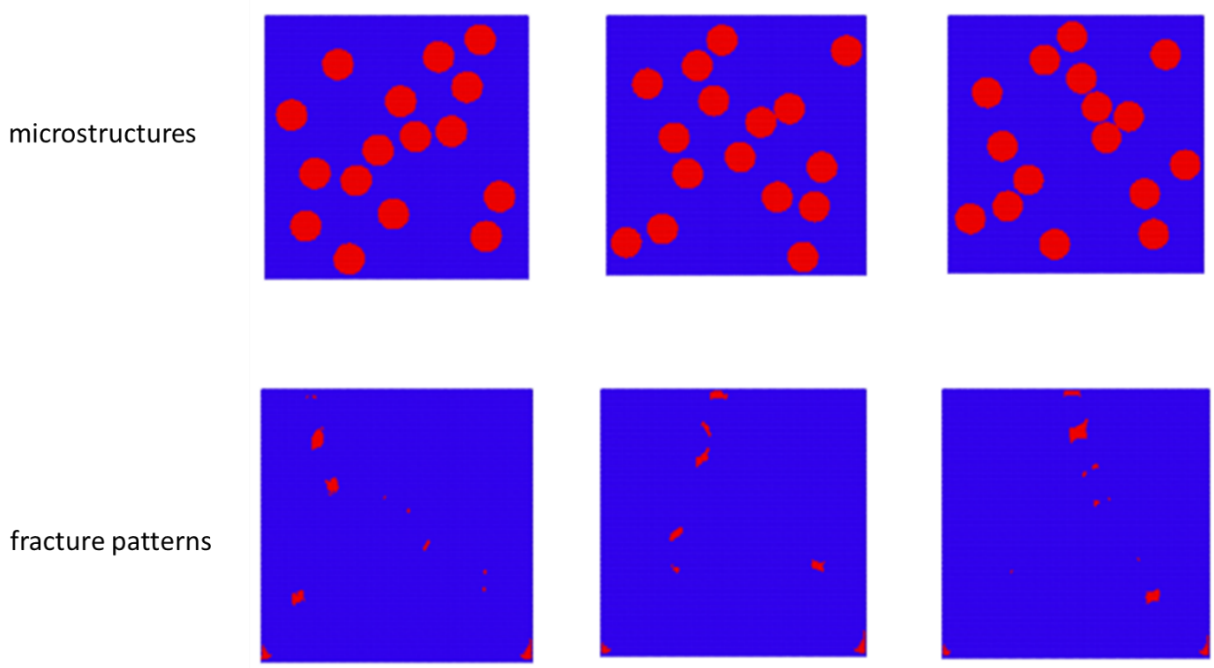

Figure 0-35 Microstructures and Corresponding Fracture Pattern

Our approach draws on success of LPM for the accuracy of simulation and deep learning for efficient nonlinear prediction. LPM can be used to compute elastic deformations of RVEs and then the proposed deep learning model takes elastic deformations and microstructures into account for fracture patterns prediction. For the proposed deep learning model, the elastic deformation and microstructures are considered as information of loading and material properties, respectively. Fracture pattern data is generated by LPM for training of the deep learning model.

LPM for fracture simulation

In order to generate training data of fracture patterns and elastic deformation, a fracture criterion is implemented in LPM. As discussed at the beginning, the fracture simulation is one of the most important advantages of LPM. Critical energy/force/elongation criteria can be

derived based on different material properties, such as fracture toughness and material strength. In particular, the fracture criterion used in this paper is bond-based, in which the critical elongation is set as 0.45% bond length. Once the critical elongation is reached by a bond during the simulation step, the bond is considered broken and removed from future simulation steps. The entire fracture process can be tracked by the bond breaking process. The flowchart of LPM fracture simulation is shown in Figure 6-6.

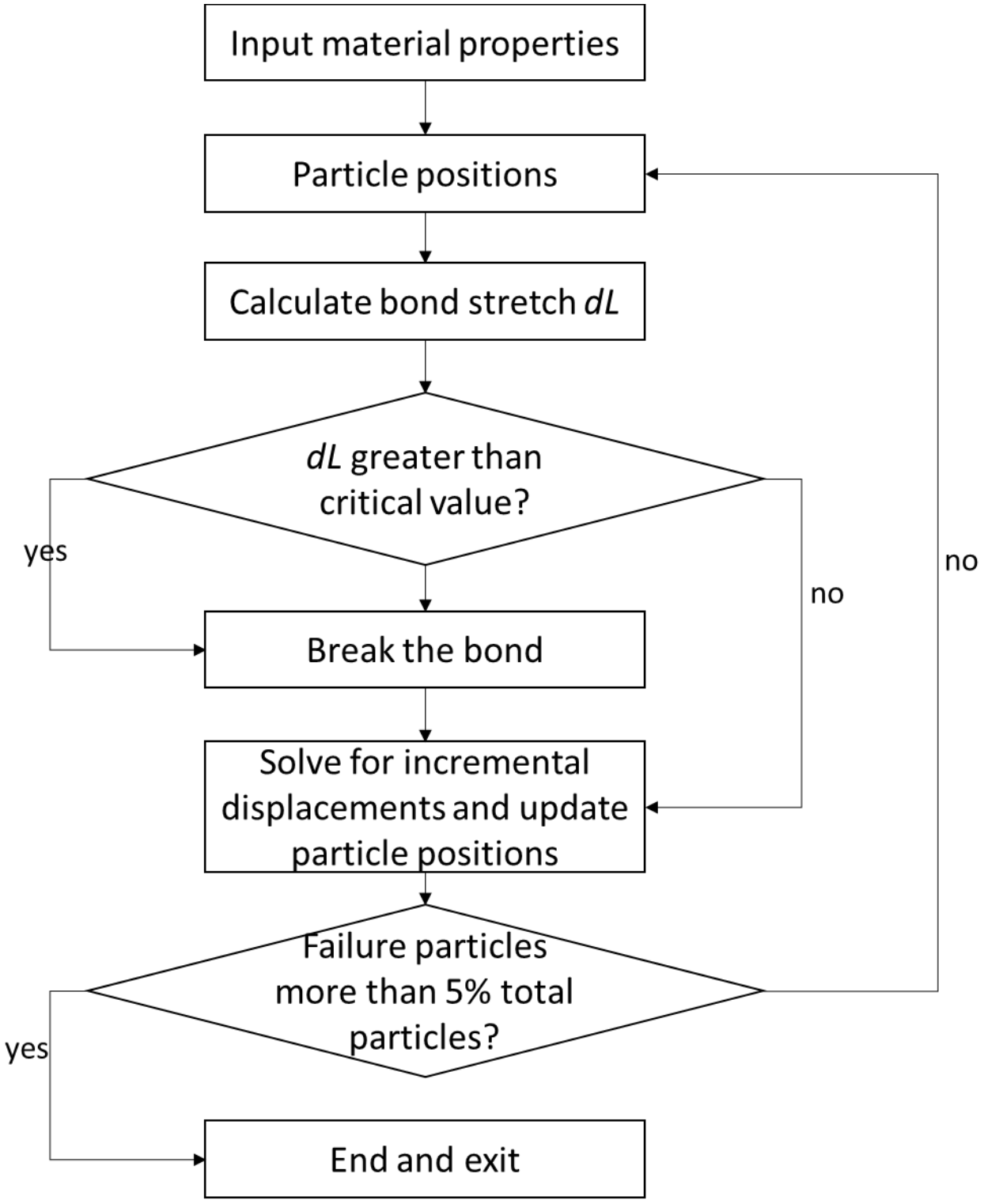

Figure 0-36 Flowchart of LPM Scheme for Fracture Simulation

In our study, each RVE consists of 26187 particles, in which particle structure is triangular. We define the failure of particle is that the particle has broken bonds. Once the number of failure particles reaches 5% of total number of particles, the material is considered as fracture failure and then material fracture pattern is collected, where particle status is labeled as 1 or 0, representing failure or not failure.

The FCN details

Fracture pattern prediction can be regarded as a task of semantic segmentation, which involves pixel-wise labeling to represent fracture failure or not. The proposed deep learning model adopts the concept of FCNs, in which data in the network is operated as images. Input data is a three-dimensional array of size $c^{in} \times h \times w$, where c^{in} denotes channels number and $h \times w$ is image dimension. The size of output array is $c^{out} \times h \times w$, where image dimension is same as input, but channels number can be different. In our investigation, the input channels, c^{in}, is three including a binary image of microstructure and two displacement images in horizontal and vertical directions, respectively. The output channels number is one, which only has one binary image of fracture pattern.

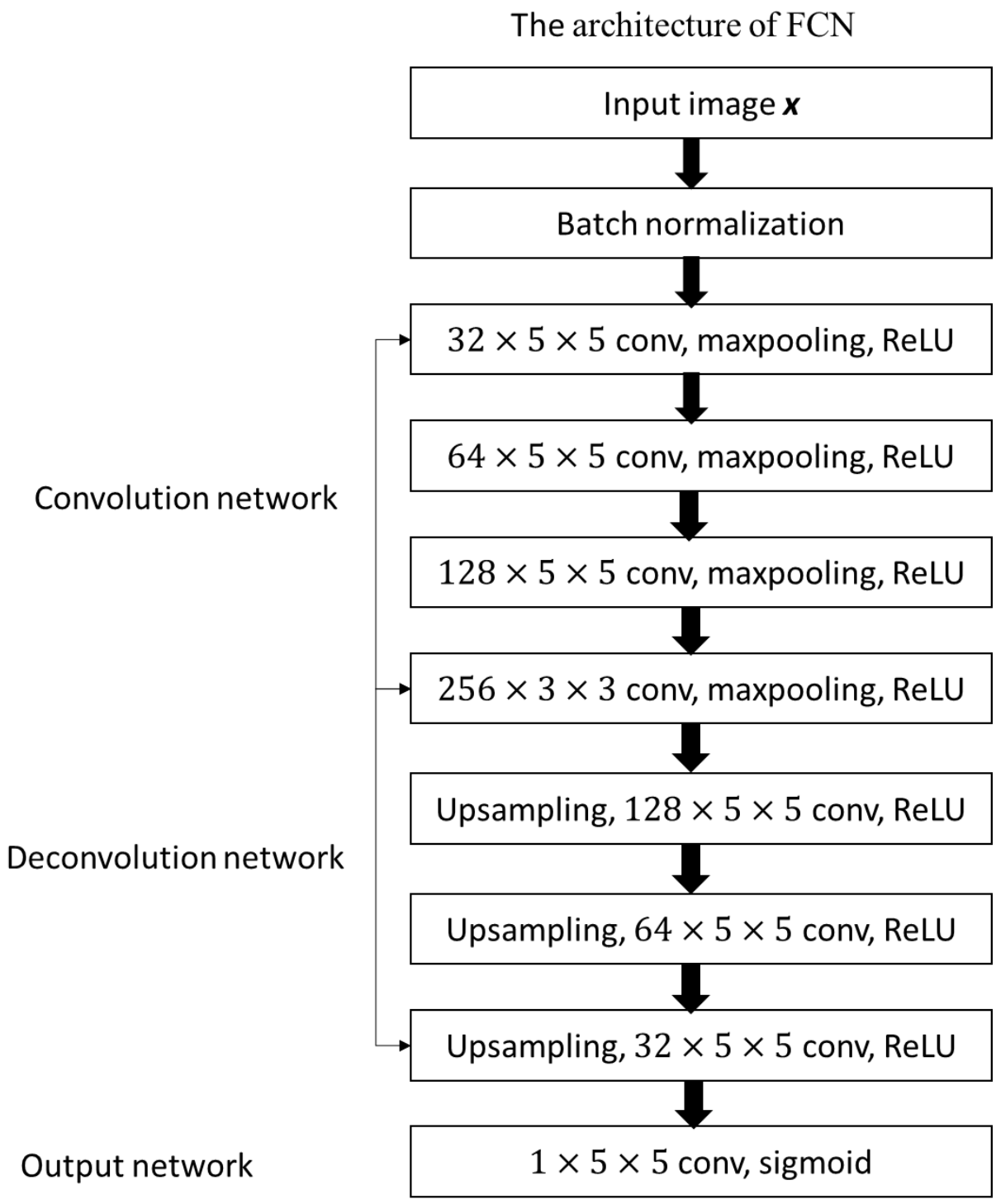

Figure 0-37 The Architecture of the Proposed FCN

The proposed neural network has three components, a convolution network, a deconvolution network, and an output network. The convolution network extracts features, and the deconvolution network labels pixels based on the features from the convolution network. The structure of the proposed FCN is shown in Figure 6-7, For the FCN, a batch normalization layer normalizes input distribution to standard Gaussian distribution. The convolution network has convolutional layers of a fixed filter size (5×5) with ReLU activation functions. The ReLU function is expressed as,

$$ReLU(x) = \max\{0, x\} \tag{6.9}$$

After each convolutional layer, there are batch normalization layers and max-pooling layers. Each pooling layer is of stride 2, down-sampling these layers by a factor of 2 along both width and height. The deconvolution network consists of up-sample layers and convolution layers following batch normalization layers. In deconvolution networks, up-sample method is bilinear interpolation with a factor of 2, and activation functions are ReLU. Because the output of the deep network is used for binary classification, the output network is a convolution layer with a logistic activation function of sigmoid. The sigmoid function in the output layer is given as,

$$sigmoid(x) = \frac{1}{1+\exp(-x)} \tag{6.10}$$

The output from the proposed network is probability of fracture failure, and the threshold is set to 0.5, i.e., the pixel is labeled as fracture failure if its output value is great than 0.5, otherwise, it is labeled as no fracture.

Training the FCN model involves minimizing a binary cross entropy loss function as:

$$L_{BCE} = -\frac{1}{N}\sum_{n=1}^{N} y_n \cdot \log(p(y_n)) + (1-y_n)\cdot \log(1-p(y_n)) \tag{6.11}$$

where N is total number of samples, y_n represents label target and $p(y_n)$ represents probability.

Physical constraint in FCN

There is a physical constraint in this problem that the fracture failure cannot occur in hole area, i.e., output pixels in hole area has zero probabilities of fracture failure. In order to improve the accuracy of the network, we apply this physical constraint following the output layer in the deep learning model by pixelwise multiplying the microstructure array as

$$y = T(x)\cdot x_m \tag{6.12}$$

where y is the output after physical constraint, T is the function representing the proposed deep network, x is the input of the deep network, x_m is the microstructure channel in the input. In the microstructure array, pixels in hole area are represented as zero, therefore, the output values of pixels in hole area are fixed to zero by the pixelwise multiplication.

5.4 Experiments and Results

In this section, we implement LPM and the deep learning to predict fracture pattern. Firstly, a dataset for the network training is generated by LPM. Then, we tune the neural network with the training dataset. Nest, the proposed model is evaluated in many aspects.

Model training

LPM is carried out to simulate 900 fracture patterns of different RVEs under random loadings. Thereinto, 80% of them are used for model training, and 20% of them are testing data. To be compatible with format of deep network implementation, all arrays from LPM simulations are converted to two-dimensional grids of size 128×128, based on the spatial coordinates corresponding to array elements, in which the nearest extrapolation method is used. The training dataset contains a binary array of RVEs' microstructures, two arrays of elastic deformations in horizontal and vertical directions and a binary array of fracture pattern. The microstructures and elastic deformations arrays are inputs, and the fracture patterns are output targets.

During training, the model performance is evaluated on testing dataset after each epoch. The detail of accuracy metric used for evaluation is discussed in next subsection. Given a large number of epochs for model training, overfitting phenomenon is found, i.e., the training accuracy metric is increasing while testing accuracy metric is decreasing. To avoid it, we adopt an early stopping approach that the training is decided to be stopped when the testing accuracy metric is smaller than its maximum value over ten epochs. For model tuning, the standard ADAM optimization algorithm and backpropagation are implemented in Pytorch. The learning rate for the ADAM optimizer was initialized to 0.0001 with a geometric decay rate of 0.9 and 0.999 for first and second moment estimates, respectively.

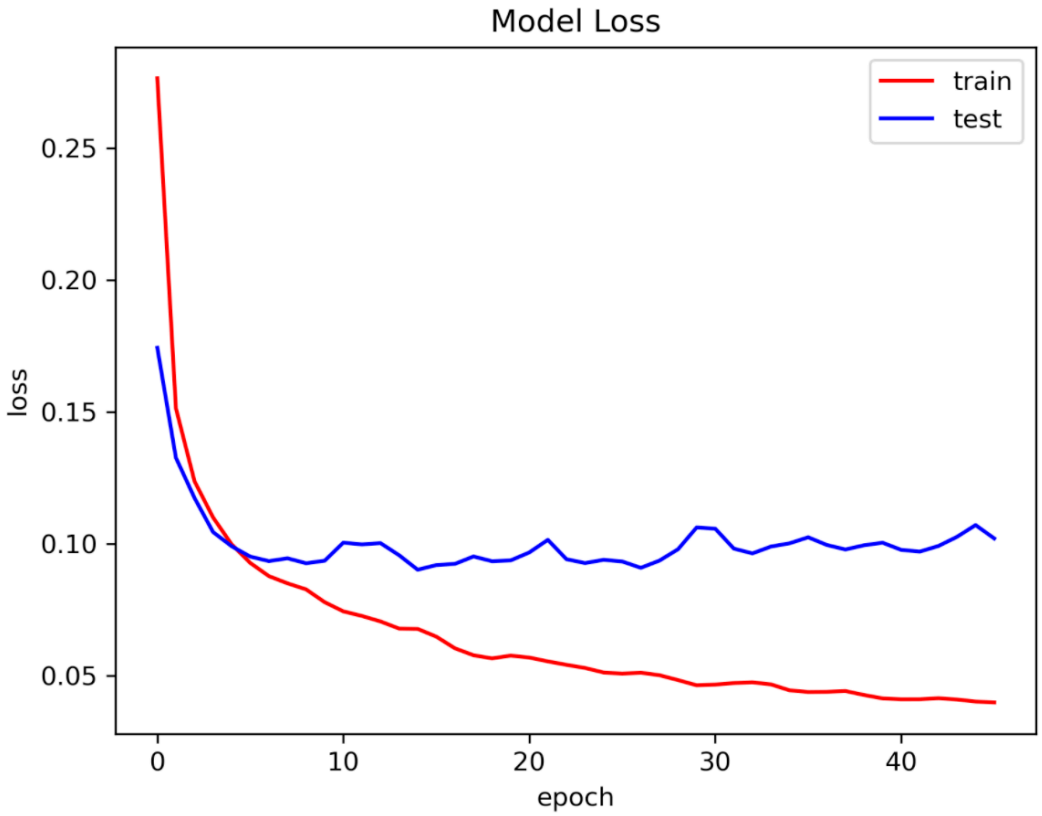

Figure 0-38 Loss History of Training and Testing Datasets

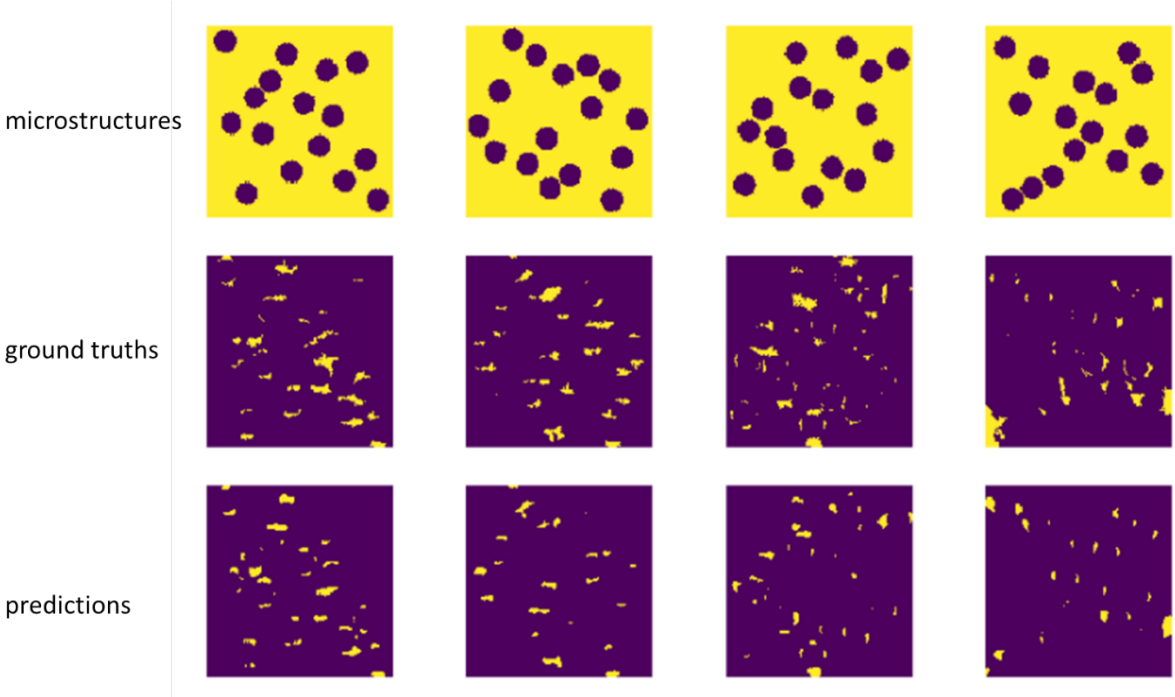

Figure 0-39 Predictions of the Deep Learning Model with Corresponding Microstructures and Truths

Figure 6-8. depicts the loss history in the training process. Figure 6-9 shows the deep learning model predictions with ground truths. The first row represents microstructures of RVEs, and the second and third rows are fracture patterns from LPM simulations and the network, respectively. It can be observed that the prediction has a good agreement with the ground truth. This verifies the predictive ability to make a solid prediction for fracture pattern.

Model evaluation

It should be noticed that fracture pattern is a kind of unbalance data that fracture pixels is around 5% of total pixels as we defined, therefore, F1 score is used as an accuracy metric to evaluate the model prediction performance. F1 score is the harmonic mean of the precision and recall, which is suitable for binary skew classification. The precision is the proportion of correct positive predictions, as

$$precision = \frac{TP}{TP + FP} \tag{6.13}$$

where TP is true positives, FP is false positives. The recall is the proportion of true positives which can be predicted, as

$$recall = \frac{TP}{TP + NP} \tag{6.14}$$

where NP False negatives. Thus, the expression of F1 score is given as

$$F1 = 2 \times \frac{precision \times recall}{precision + recall} \tag{6.15}$$

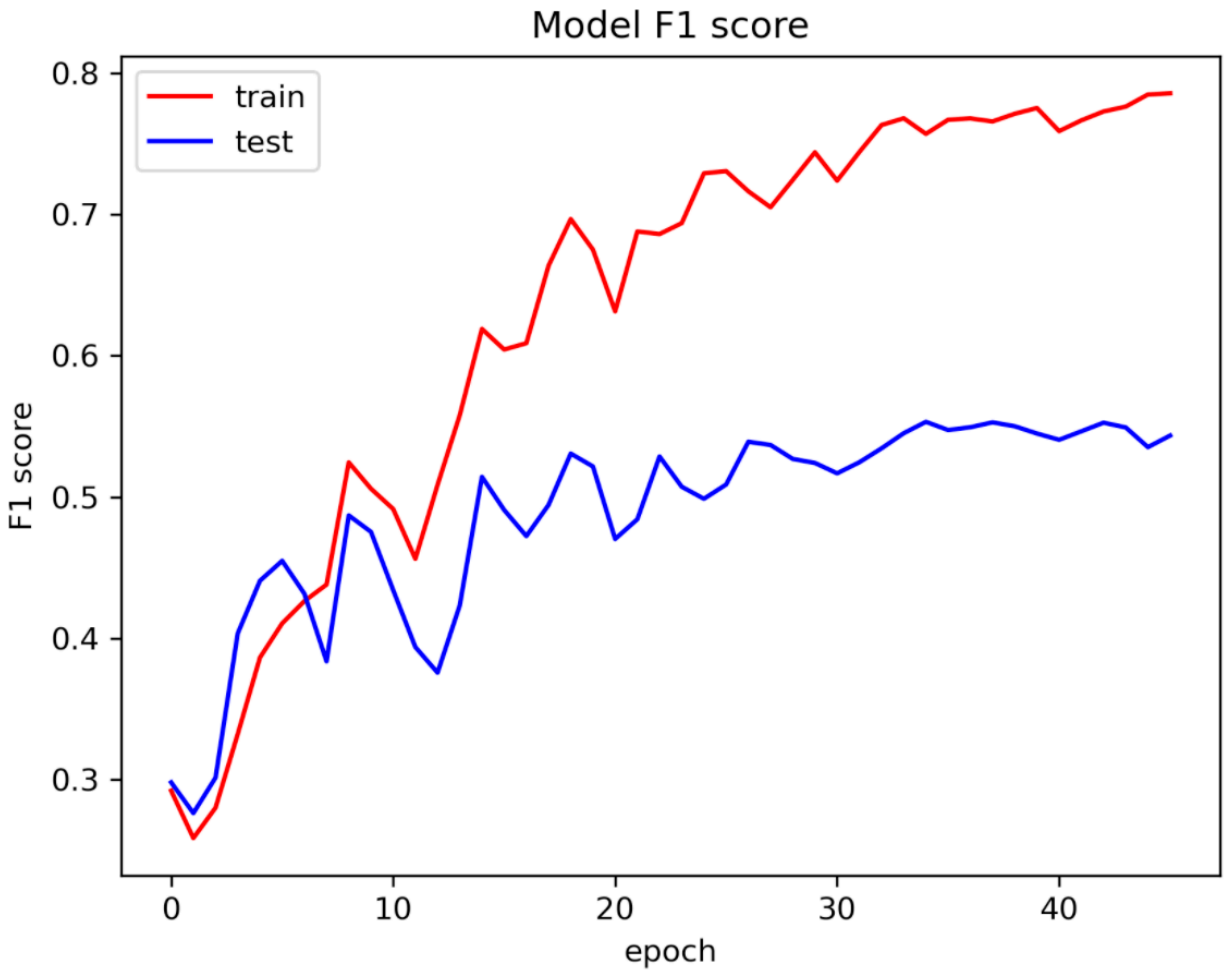

Figure 0-40 F1 Score History of Training and Testing Datasets

Figure 6-10. shows the F1 score history in the model training process. After tuning the proposed model, the F1 scores for training and testing datasets can reach to 0.8 and 0.5, respectively. However, the F1 score metric is not sufficient to evaluate the model performance in this study, because F1 score metric computes the prediction as a one-dimensional flatten array and ignores spatial information in prediction. To explain this issue, we use a typical example of two-dimensional array of size 8×8. In Figure 6-11, a ground truth and two predictions are given. The F1 scores for two predictions are 0, because both two predictions have no positives correctly predicted. While the left prediction is considered much more

accurate than the right prediction, since the predicted positives in the left prediction is spatially closer to the true positives in the ground truth. We then adopt max pooling with a factor of 2 to extract the spatial accuracy of the ground truth and two predictions, as shown in Figure 6-12. After max pooling, the F1 scores for the left and right predictions are changed to 1 and 0, respectively.

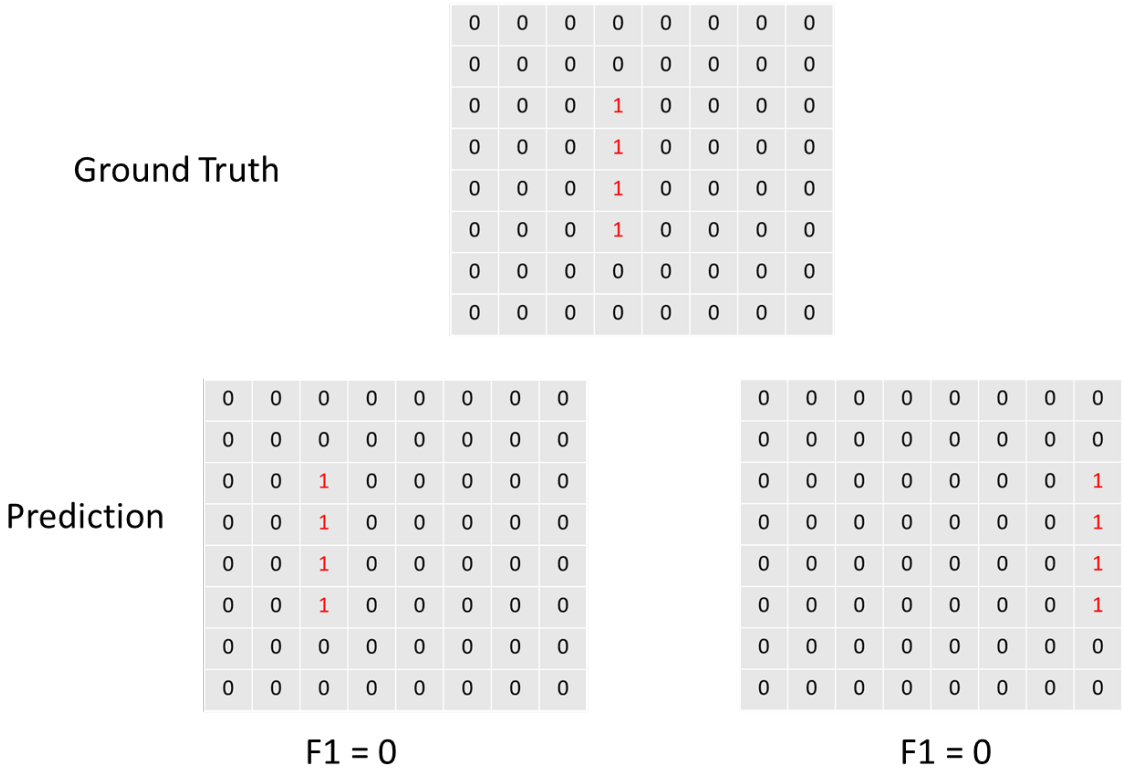

Figure 0-41 An Example of F1 Score Calculation without Max Pooling Operation

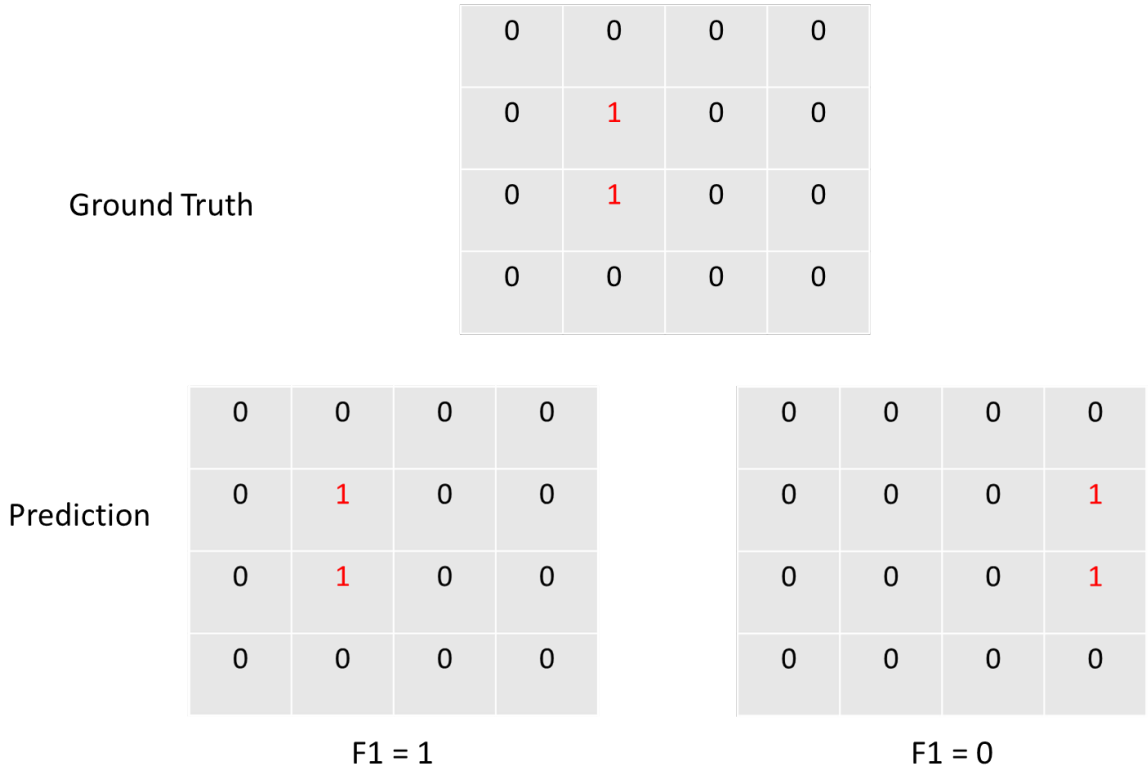

Figure 0-42 An Example of F1 score Calculation after Max Pooling Operation

This indicates that max pooling operation can be used for spatial accuracy evaluation, and the F1 score is higher with max pooling if the prediction has better spatial accuracy. Therefore, we perform max pooling for the predictions from the proposed model and the ground truths generated by LPM, and then we compare the F1 scores to show the spatial accuracy. The array size is changed from 128×128 to 64×64. It can be seen in Figure 6-13, the F1 score is improved to 0.6, which demonstrates the spatial accuracy of the proposed model.

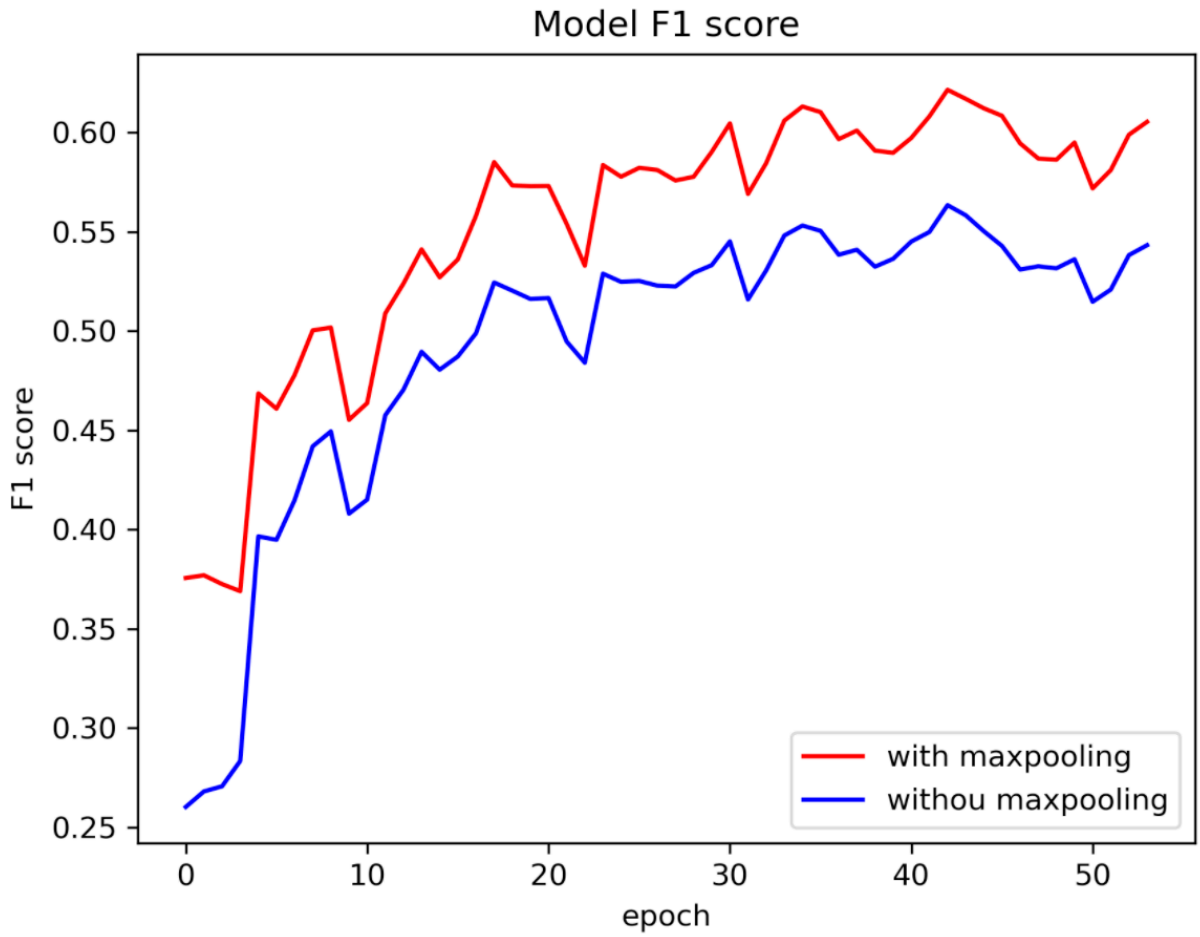

Figure 0-43 F1 Score History of Training and Testing Datasets after Max Pooling

Effect of physical constraints

The contribution of the physical constraint can be obtained via accuracy metric, shown in Figure 6-14. Comparing the F1 scores with and without the physical constraint, it can be observed that the physical constraint improves the model accuracy and accelerates the tuning process by reducing the model training iterations before overfitting. This work shows that the potential of utilizing physics prior knowledge to help designing neural network for physics problems.

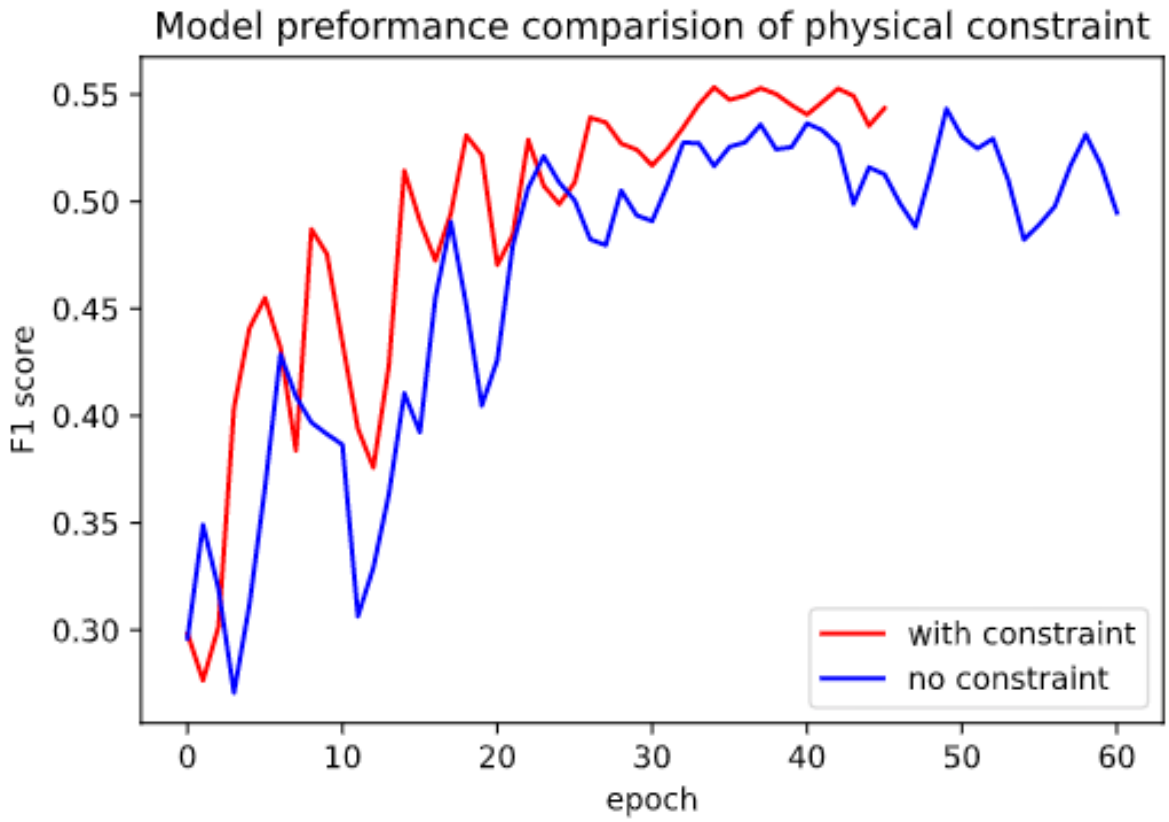

Figure 0-44 The Physical Constraint Effect Shown by F1 Scores

Comparison of different loadings

A benchmark is investigated to verify the predictive power of the proposed model, which has a given arbitrary microstructure under two different loadings. The microstructure is shown in the first row in Fig. 15. The first loading scenario is to load the specimen on right surface in horizontal direction, and the second loading scenario applies load on the bottom surface downward. The boundary conditions for two scenarios are same that left and top surfaces are clamped in horizontal and vertical directions, respectively, see the second row in Figure 6-15. The third and fourth rows in Figure 6-15. present the ground truths and the predictions. As expected, the predicted fracture patterns are similar with the ground truths, meanwhile, with

same microstructure is predicted patterns are different for different loadings. This benchmark demonstrates that the proposed model is able to predict the fracture pattern without a limitation of material microstructure and loading conditions.

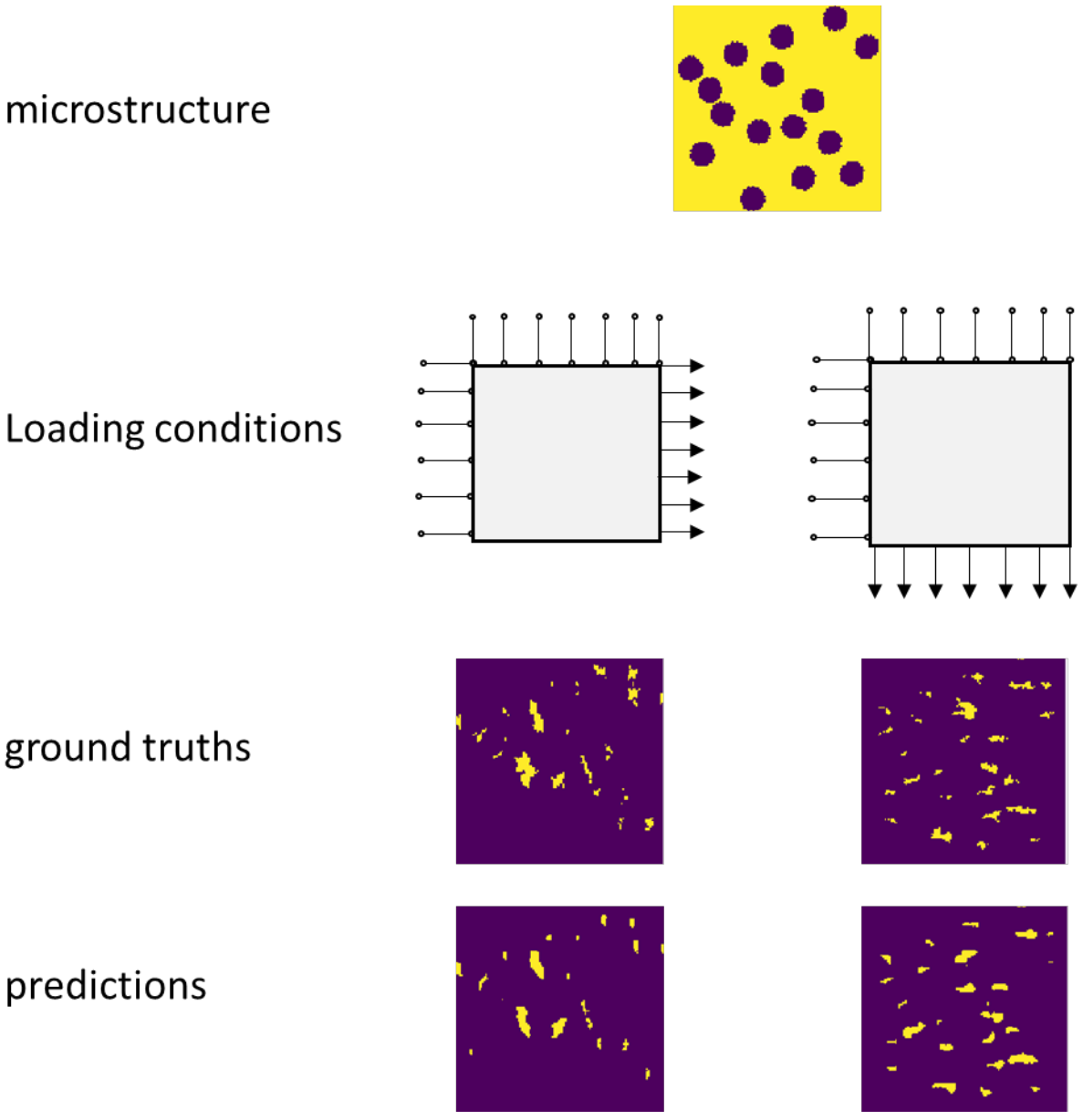

Figure 0-45 Fracture Patterns under Different Loadings with Same Microstructure

5.5 Conclusion

In this paper, a new computational framework is developed to predict fracture pattern under various loading conditions with different microstructures. The framework includes LPM for elastic linear deformation simulation and a proposed deep learning model for nonlinear fracture simulation, which considers both computational accuracy and efficiency. LPM is used to calculate material elastic displacement as the inputs for the deep learning model, and also generate dataset to tune the deep network. The proposed deep learning model is based on the concept of FCNs. A physical constraint is integrated to improve the deep learning model predictive performance. The proposed model is evaluated by different microstructures and loading conditions. Several major conclusions are

- The proposed computational framework takes advantages of LPM and the deep learning model and can predict fracture pattern efficiently without losing accuracy. Predicted fracture patterns of different microstructures and different loading conditions have good agreement with ground truths;
- The proposed deep learning model with a physical constraint has better predictive performance. The applied physical constraint improves the F1 score 10% higher and reduces iteration number of the model training;
- Using max-pooling operation, we demonstrate that the proposed model considers the spatial accuracy of prediction.

The proposed deep learning model is integrated with LPM in this study. It should be mentioned that the deep learning model has potential to integrating with other mechanics models to predict material fracture patterns. Future work will be toward extending the proposed model to fracture analysis of ductile materials and composite materials, which will require

more complex mechanics models. The performance of the deep learning network has potential to be improved by modifying the network structure with CNNs algorithms, such as ResNet[134] and Feature Pyrimad Networks (FPN)[137].

7. SUMMARY AND FUTURE WORK

7.1 Conclusions

In this dissertation, we make a lot of efforts to simulate material failure. First, a yield criterion based on maximum distortional energy is developed for LPM, which is suitable for failure analysis due to its discontinuity. Then we investigate multiaxial fatigue models for random and constant biaxial loadings. Following this, the multiaxial fatigue model is integrated with LPM for fatigue simulation of bi-phase material. Finally, a surrogate model based on neural network is proposed to reduce computational cost of fracture failure simulation with various microstructures.

In Chapter 2, following the basic idea of its formulation in classical continuum mechanics, a maximum distortion energy criterion was formulated for LPM. Important ingredients for this nonlocal yield criterion including additive decomposition of bond stretch, incremental formulation of LPM for plastic analysis, nonlocal yield function, consistency conditions and equivalent strain hardening rules were developed. An implicit solution scheme for static or quasi-static elastoplastic problems using the developed yield criterion in LPM was outlined. Several benchmark problems including monotonic tensile yielding and cyclic yielding with isotropic, kinematic and mixed strain hardenings were tested and model predictions were compared against theoretical and numerical solutions. From the comparison, the developed nonlocal maximum distortion energy criterion is valid and can yields accurate results for elastoplastic materials.

In Chapter 3, a stress-based fatigue model under arbitrary random multiaxial loading is proposed using the Liu-Mahadeven critical plane concept and an equivalent stress transformation method. The current investigation focuses on the high cycle fatigue (HCF).

Linear damage accumulation is shown to have satisfactory results and the used spectrum are not highly nonstationary, such as high-low and low-high step loading.

In Chapter 4, a new energy-based fatigue model is developed to assess fatigue life under various multiaxial constant amplitude loading conditions with different loading paths. The energy-based model considers three fatigue damage contributions of tensile energy term, torsional energy term, and hydrostatic energy term. In case of only stress or strain reported, Garud cyclic plasticity model is integrated to calculate stress or strain hysteresis. Both proportional and non-proportional loading are considered in the validation.

In Chapter 5, The fatigue criterion based on distortional and dilatational energy can be integrated with LPM to do fatigue analysis. The energy-based fatigue criterion is capable of modeling fatigue crack initiation and propagation using LPM. For fatigue crack propagation, LPM predictions have a good agreement with experimental Paris law curve. Bi-phase material fatigue analysis shows the potential of LPM for complex material and structural fatigue simulation.

In Chapter 6, a new computational framework is developed to predict fracture pattern under various loading conditions with different microstructures. The framework includes LPM for elastic linear deformation simulation and a proposed deep learning model for nonlinear fracture simulation, which considers both computational accuracy and efficiency. LPM is used to calculate material elastic displacement as the inputs for the deep learning model, and also generate dataset to tune the deep network. The proposed model is evaluated by different microstructures and loading conditions. Predicted fracture patterns of different microstructures and different loading conditions have good agreement with ground truths.

7.2 Future Work

There are many future works in the remainder of the investigation. It includes the following issues:

1. Extension of LPM to more complex nonlinear constitutive laws of solids, such as viscoelasticity, cohesive zone model and crystal plasticity. This will make LPM to be applied to more different kinds of materials.
2. Investigation of fracture failure criterion for LPM. Comparing with the fatigue criterion used in LPM, the fracture criterion is naïve depending on either critical bond stretch or bond force. More rigorous fracture criterion is needed for general facture failure problems, such as maximum normal stress and maximum shear stress fracture.
3. Modifying the neural network with state-of -the-art CNNs algorithms, such as ResNet[134] and Feature Pyrimad Networks (FPN)[137] to improve the predictive performance.

REFERENCES

[1] A. Trädegård, F. Nilsson, and S. Östlund, "FEM-remeshing technique applied to crack growth problems," *Comput. Methods Appl. Mech. Eng.*, 1998, doi: 10.1016/S0045-7825(97)00287-9.

[2] M. Elices, G. V. Guinea, J. Gómez, and J. Planas, "The cohesive zone model: Advantages, limitations and challenges," *Eng. Fract. Mech.*, 2001, doi: 10.1016/S0013-7944(01)00083-2.

[3] Y. Wang and P. Mora, "Macroscopic elastic properties of regular lattices," *J. Mech. Phys. Solids*, vol. 56, no. 12, pp. 3459–3474, 2008, doi: 10.1016/j.jmps.2008.08.011.

[4] A. Pazdniakou and P. M. Adler, "Lattice spring models," *Transp. Porous Media*, vol. 93, no. 2, pp. 243–262, 2012, doi: 10.1007/s11242-012-9955-6.

[5] E. Madenci and S. Oterkus, "Ordinary state-based peridynamics for plastic deformation according to von Mises yield criteria with isotropic hardening," *J. Mech. Phys. Solids*, 2016, doi: 10.1016/j.jmps.2015.09.016.

[6] A. Hrennikoff, "Solution of problems of elasticity by the framework method," *J. Appl. Mech.*, vol. 8, pp. A619–A715, 1941.

[7] P. D. Beale and D. J. Srolovitz, "Elastic fracture in random materials," *Phys. Rev. B*, vol. 37, no. 10, pp. 5500–5507, 1988, doi: 10.1103/PhysRevB.37.5500.

[8] S. F. Zhao and G. F. Zhao, "Implementation of a high order lattice spring model for elasticity," *Int. J. Solids Struct.*, 2012, doi: 10.1016/j.ijsolstr.2012.05.015.

[9] H. Chen, E. Lin, Y. Jiao, and Y. Liu, "A generalized 2D non-local lattice spring model for fracture simulation," vol. 54, pp. 1541–1558, 2014, doi: 10.1007/s00466-014-1075-4.

[10] H. Chen, Y. Jiao, and Y. Liu, "A nonlocal lattice particle model for fracture simulation of anisotropic materials," *Compos. Part B Eng.*, vol. 90, pp. 141–151, 2016, doi: 10.1016/j.compositesb.2015.12.028.

[11] R. E. Little, "Fatigue Stresses from Complex Loadings," *Mach. Des.*, vol. 38, pp. 145–149, 1966.

[12] B. F. Langer, "Design of Pressure Vessels Involving Fatigue," in *Pressure Vessel Engineering*, R. W. Nichols, Ed. Amsterdam: Elsevier Publishing Co., 1971, pp. 59–100.

[13] G. Z. Libertiny, "Short Life Fatigue under Combined Stresses," *J. Strain Anal.*, vol. 2, no. 1, pp. 91–95, 1967.

[14] S. Y. Zamrik, "An Investigation of Strain Cycling Behavior of 7075-T6 Aluminum under Combined State of Strain," 1972. doi: NASA CR-72843.

[15] A. O. Findley, W. N., Mathur, P. N., Szezepanski, E., and Temel, "Energy- versus

Stress Theories for Combined Stress--A Fatigue Experiment using a Rotating Disk," *J. Basic Eng. Ser. D Trans. A.S.M.E,* vol. 83, no. 1, pp. 10–14, 1961.

[16] B. N. Leis, "An Energy-Based Fatigue and Creep-Fatigue Damage Parameter," *J. Press. Vessel Technol. Trans. A.S.M.E.*, vol. 99, no. 4, pp. 524–533, 1977.

[17] S. Kruch, P. Prigent, and J. L. Chaboche, "A fracture mechanics based fatigue-creep-environment crack growth model for high temperature," *Int. J. Press. Vessel. Pip.*, vol. 59, no. 1–3, pp. 141–148, 1994, doi: 10.1016/0308-0161(94)90149-X.

[18] D. Socie, "Multiaxial Fatigue Damage Models," *J. Eng. Mater. Technol.*, vol. 109, no. October 1987, pp. 293–298, 1987, doi: 10.1115/1.3225980.

[19] G. Glinka, G. Shen, and A. Plumtree, "A Multiaxial Fatigue Strain Energy Density Parameter Related To the Critical Fracture Plane," *Fatigue Fract. Eng. Mater. Struct.*, vol. 18, no. 1, pp. 37–46, 1995, doi: 10.1111/j.1460-2695.1995.tb00140.x.

[20] A. Varvani-Farahani, "New energy-critical plane parameter for fatigue life assessment of various metallic materials subjected to in-phase and out-of-phase multiaxial fatigue loading conditions," *Int. J. Fatigue*, vol. 22, no. 4, pp. 295–305, 2000, doi: 10.1016/S0142-1123(00)00002-5.

[21] K. N. Smith, P. Watson, and T. H. Topper, "Stress-Strain Function for the Fatigue of Metals," *Journal of Materials*, vol. 5. pp. 767–778, 1970.

[22] C. C. C. F. A. Chu and J. J. Bonnen, "Multiaxial Stress-Strain Modelling and Fatigue Life Prediction of {SAE} Axle Shafts," *Adv. Multiaxial Fatigue, {ASTM} {STP} 1191*, pp. 37–54, 1993.

[23] K. S. Kim, K. M. Nam, G. J. Kwak, and S. M. Hwang, "A fatigue life model for 5% chrome work roll steel under multiaxial loading," *Int. J. Fatigue*, vol. 26, no. 7, pp. 683–689, 2004, doi: 10.1016/j.ijfatigue.2003.11.005.

[24] A. Carpinteri and A. Spagnoli, "Multiaxial high-cycle fatigue criterion for hard metals," *Int. J. Fatigue*, vol. 23, pp. 135–145, 2001, doi: 10.1016/S0142-1123(00)00075-X.

[25] J. A. Araújo, A. Carpinteri, C. Ronchei, A. Spagnoli, and S. Vantadori, "An alternative de fi nition of the shear stress amplitude based on the Maximum Rectangular Hull method and application to the C-S (Carpinteri-Spagnoli) criterion," pp. 764–771, 2014, doi: 10.1111/ffe.12180.

[26] A. Carpinteri, C. Ronchei, A. Spagnoli, and S. Vantadori, "Lifetime estimation in the low / medium-cycle regime using the Carpinteri – Spagnoli multiaxial fatigue criterion," *Theor. Appl. Fract. Mech.*, vol. 73, pp. 120–127, 2014, doi: 10.1016/j.tafmec.2014.06.002.

[27] A. Carpinteri, A. Spagnoli, C. Ronchei, D. Scorza, and S. Vantadori, "Critical plane criterion for fatigue life calculation : time and frequency domain formulations," *Procedia Eng.*, vol. 101, pp. 518–523, 2015, doi: 10.1016/j.proeng.2015.02.062.

[28] Y. Liu and S. Mahadevan, “Multiaxial high-cycle fatigue criterion and life prediction for metals,” *Int. J. Fatigue*, vol. 27, no. 7, pp. 790–800, 2005, doi: 10.1016/j.ijfatigue.2005.01.003.

[29] Y. Liu and S. Mahadevan, “Strain-based multiaxial fatigue damage modelling,” *Fatigue Fract. Eng. Mater. Struct.*, vol. 28, no. 12, pp. 1177–1189, 2005, doi: 10.1111/j.1460-2695.2005.00957.x.

[30] H. Wei and Y. Liu, “A critical plane-energy model for multiaxial fatigue life prediction,” *Fatigue Fract. Eng. Mater. Struct.*, vol. 40, no. 12, pp. 1973–1983, 2017, doi: 10.1111/ffe.12614.

[31] S. Li and W. K. Liu, “Meshfree and particle methods and their applications,” *Appl. Mech. Rev.*, vol. 55, no. 1, p. 1, 2002, doi: 10.1115/1.1431547.

[32] V. Nguyen, M. Stroeven, and L. J. Sluys, “Multiscale Continuous and Discontinuous Modeling of Heterogeneous Materials: a Review on Recent Developments,” *J. Multiscale Model.*, vol. 03, no. 04, pp. 229–270, 2011, doi: 10.1142/S1756973711000509.

[33] A. K. Noor and M. P. Nemeth, “Micropolar beam models for lattice grids with rigid joints,” *Comput. Methods Appl. Mech. Eng.*, vol. 21, no. 2, pp. 249–263, 1980, doi: 10.1016/0045-7825(80)90034-1.

[34] E. Schlangen and E. Garboczi, “Fracture simulations of concrete using lattice models: Computational aspects,” *Eng. Fract. Mech.*, vol. 57, no. 2, pp. 319–332, 1997.

[35] J. E. Bolander and N. Sukumar, “Irregular lattice model for quasistatic crack propagation,” *Phys. Rev. B - Condens. Matter Mater. Phys.*, vol. 71, no. 9, pp. 1–12, 2005, doi: 10.1103/PhysRevB.71.094106.

[36] P. Grassl, Z. Bazant, and C. Gianluca, “Lattice-cell approach to quasibrittle fracture modeling,” in *Computational Modelling of Concrete Structures: Proceedings of the EURO-C conference 2006*, 2006, pp. 263–268.

[37] G. Cusatis, Z. P. Bažant, and L. Cedolin, “Confinement-shear lattice CSL model for fracture propagation in concrete,” *Comput. Methods Appl. Mech. Eng.*, 2006, doi: 10.1016/j.cma.2005.04.019.

[38] G. Wang, A. Al-Ostaz, A. H. D. Cheng, and P. R. Mantena, “Hybrid lattice particle modeling: Theoretical considerations for a 2D elastic spring network for dynamic fracture simulations,” *Comput. Mater. Sci.*, 2009, doi: 10.1016/j.commatsci.2008.07.032.

[39] G.-F. Zhao, J. Fang, and J. Zhao, “A 3D distinct lattice spring model for elasticity and dynamic failure,” *Int. J. Numer. Anal. Methods Geomech.*, vol. 35, pp. 859–885, 2011, doi: 10.1002/nag.

[40] S. F. Zhao and G. F. Zhao, “Implementation of a high order lattice spring model for elasticity,” *Int. J. Solids Struct.*, vol. 49, no. 18, pp. 2568–2581, 2012, doi:

10.1016/j.ijsolstr.2012.05.015.

[41] A. P. Jivkov and J. R. Yates, “Elastic behaviour of a regular lattice for meso-scale modelling of solids,” *Int. J. Solids Struct.*, 2012, doi: 10.1016/j.ijsolstr.2012.06.010.

[42] M. Ostoja-Starzewski, “Lattice models in micromechanics,” *Appl. Mech. Rev.*, vol. 55, no. 1, p. 35, 2002, doi: 10.1115/1.1432990.

[43] Z. Pan, R. Ma, D. Wang, and A. Chen, “A review of lattice type model in fracture mechanics: theory, applications, and perspectives,” *Eng. Fract. Mech.*, 2018, doi: 10.1016/j.engfracmech.2017.12.037.

[44] M. Nikolić, E. Karavelić, A. Ibrahimbegovic, and P. Miščević, “Lattice Element Models and Their Peculiarities,” *Archives of Computational Methods in Engineering*, vol. 25, no. 3. pp. 753–784, 2018, doi: 10.1007/s11831-017-9210-y.

[45] G. A. Buxton, C. M. Care, and D. J. Cleaver, “A lattice spring model of heterogeneous materials with plasticity A lattice spring model of heterogeneous materials with plasticity,” *Model. Simul. Mater. Sci. Eng.*, vol. 9, pp. 485–497, 2001, doi: 10.1088/0965-0393/9/6/302.

[46] H. Yan, G. Li, and L. M. Sander, “Fracture growth in 2d elastic networks with born model,” *Epl*, vol. 10, no. 1, pp. 7–13, 1989, doi: 10.1209/0295-5075/10/1/002.

[47] G. F. Zhao, J. Lian, A. Russell, and N. Khalili, “Implementation of a modified Drucker–Prager model in the lattice spring model for plasticity and fracture,” *Comput. Geotech.*, 2019, doi: 10.1016/j.compgeo.2018.11.021.

[48] Y. P. Cheng, M. D. Bolton, and Y. Nakata, “Crushing and plastic deformation of soils simulated using DEM,” *Geotechnique*, vol. 54, no. 2, pp. 131–141, 2004, doi: 10.1680/geot.2004.54.2.131.

[49] N. H. T. Nguyen, H. H. Bui, G. D. Nguyen, and J. Kodikara, “A cohesive damage-plasticity model for DEM and its application for numerical investigation of soft rock fracture properties,” *Int. J. Plast.*, 2017, doi: 10.1016/j.ijplas.2017.07.008.

[50] J. T. Foster, S. A. Silling, and W. W. Chen, “Viscoplasticity using peridynamics,” *Int. J. Numer. Methods Eng.*, no. August 2009, pp. 1242–1258, 2010, doi: 10.1002/nme.

[51] M. M. Rahaman, P. Roy, D. Roy, and J. N. Reddy, “A peridynamic model for plasticity: Micro-inertia based flow rule, entropy equivalence and localization residuals,” *Comput. Methods Appl. Mech. Eng.*, 2017, doi: 10.1016/j.cma.2017.07.034.

[52] H. Chen, E. Lin, Y. Jiao, and Y. Liu, “A generalized 2D non-local lattice spring model for fracture simulation,” *Comput. Mech.*, vol. 54, no. 6, pp. 1541–1558, 2014, doi: 10.1007/s00466-014-1075-4.

[53] H. Chen and Y. Liu, “A non-local 3D lattice particle framework for elastic solids,” *Int. J. Solids Struct.*, vol. 81, pp. 411–420, 2016, doi: 10.1016/j.ijsolstr.2015.12.026.

[54] M. S. Daw and M. I. Baskes, “Embedded-atom method: Derivation and application to impurities, surfaces, and other defects in metals,” *Phys. Rev. B*, vol. 29, no. 12, 1984, doi: 10.1103/PhysRevB.29.6443.

[55] H. Chen, Y. Jiao, and Y. Liu, “Investigating the microstructural effect on elastic and fracture behavior of polycrystals using a nonlocal lattice particle model,” *Mater. Sci. Eng. A*, vol. 631, pp. 173–180, 2015, doi: 10.1016/j.msea.2015.02.046.

[56] H. Chen, E. Lin, and Y. Liu, “A novel Volume-Compensated Particle method for 2D elasticity and plasticity analysis,” *Int. J. Solids Struct.*, vol. 51, no. 9, pp. 1819–1833, 2014, doi: 10.1016/j.ijsolstr.2014.01.025.

[57] H. Chen, “Constructing continuum-like measures based on a nonlocal lattice particle model: Deformation gradient, strain and stress tensors,” *Int. J. Solids Struct.*, 2019, doi: 10.1016/j.ijsolstr.2019.04.014.

[58] B. Liu, Y. Huang, H. Jiang, S. Qu, and K. C. Hwang, “The atomic-scale finite element method,” *Comput. Methods Appl. Mech. Eng.*, vol. 193, no. 17–20, pp. 1849–1864, 2004, doi: 10.1016/j.cma.2003.12.037.

[59] E. Lin, H. Chen, and Y. Liu, “Finite element implementation of a non-local particle method for elasticity and fracture analysis,” *Finite Elem. Anal. Des.*, vol. 93, no. C, pp. 1–11, 2015, doi: 10.1016/j.finel.2014.08.008.

[60] E. A. de Souza Neto, D. Peric, and D. R. Owen, *Computational Methods for Plasticity: Theory and Applications*. John Wiley & Sons, 2011.

[61] T. Belytschko, J. S. J. Ong, Wing Kam Liu, and J. M. Kennedy, “Hourglass control in linear and nonlinear problems,” *Comput. Methods Appl. Mech. Eng.*, 1984, doi: 10.1016/0045-7825(84)90067-7.

[62] G. Li, S. Datta, A. Chattopadhyay, N. Iyyer, and N. Phan, “An online-offline prognosis model for fatigue life prediction under biaxial cyclic loading with overloads,” *Fatigue Fract. Eng. Mater. Struct.*, vol. 42, no. 5, pp. 1175–1190, 2019, doi: 10.1111/ffe.12983.

[63] A. Fatemi and N. Shamsaei, “Multiaxial fatigue: An overview and some approximation models for life estimation,” *Int. J. Fatigue*, vol. 33, no. 8, pp. 948–958, 2011, doi: 10.1016/j.ijfatigue.2011.01.003.

[64] M. V. Borodii and V. A. Strizhalo, “Analysis of the experimental data on a low cycle fatigue under nonproportional straining,” *Int. J. Fatigue*, vol. 22, no. 4, pp. 275–282, 2000, doi: 10.1016/S0142-1123(00)00005-0.

[65] T. Łagoda, E. Macha, and A. Niesłony, “Fatigue life calculation by means of the cycle counting and spectral methods under multiaxial random loading,” *Fatigue Fract. Eng. Mater. Struct.*, vol. 28, no. 4, pp. 409–420, 2005, doi: 10.1111/j.1460-2695.2005.00877.x.

[66] A. P. X. Pitoiset, I. Rychlik, “Spectral methods to estimate local multiaxial fatigue

failure for," *Mater. Struct.*, no. 1996, pp. 715–727, 2001.

[67] A. Carpinteri, A. Spagnoli, and S. Vantadori, "A multiaxial fatigue criterion for random loading," *Fatigue Fract. Eng. Mater. Struct.*, vol. 26, no. 6, pp. 515–522, 2003, doi: 10.1046/j.1460-2695.2003.00620.x.

[68] A. Fatemi and L. Yang, "Cumulative fatigue damage and life prediction theories: A survey of the state of the art for homogeneous materials," *Int. J. Fatigue*, 1998, doi: 10.1016/S0142-1123(97)00081-9.

[69] C. H. W. M. W. Brown, D. K. Suker, "An analysis of mean stress in multiaxial random fatigue," *Fatigue Fract. Eng. Mater. Struct.*, vol. 19, no. 2, pp. 323–333, 1996, doi: 10.1111/j.1460-2695.1996.tb00970.x.

[70] A. Niesłony and M. Böhm, "Mean stress effect correction in frequency-domain methods for fatigue life assessment," *Procedia Eng.*, vol. 101, no. C, pp. 347–354, 2015, doi: 10.1016/j.proeng.2015.02.042.

[71] Y. L. Yibing Xiang, "Equivalent Stress Transformation for Efficient Probabilistic Fatigue-Crack Growth Analysis under Variable Amplitude Loadings," *J. Aerosp. Eng.*, vol. 29, no. 2, 2015, doi: 10.1061/(ASCE)AS.

[72] M. J. Hinich, "Testing for Gaussianity and linearity of a stationary time series," *J. time Ser. Anal.*, vol. 3, no. 3, pp. 169–176, 1982.

[73] D. J. Edwards PR, "Standardized Fatigue Loading Sequences for Helicopter Rotors (HELIX and FELIX)," in *RAE-Reports TR 84084 and TR 84085*, Royal Aircraft Establishment, 1984.

[74] W. Aicher *et al.*, "Description Of A Fighter Aircraft Loading Standard for Fatigue Evaluation FALSTAFF," in *Common report of FCW Emmen, LBF, NLR, IABG*, 1976.

[75] H. Lowak, J. B. Dejonge, J. Franz, and D. Schuetz, "Minitwist, a Shortened Version of Twist.," in *NLR-Report MP 79018, LBF-Report TF-146*, 1979.

[76] T. Zhao and Y. Jiang, "Fatigue of 7075-T651 aluminum alloy," *Int. J. Fatigue*, vol. 30, no. 5, pp. 834–849, 2008, doi: 10.1016/j.ijfatigue.2007.07.005.

[77] Y. Liu and S. Mahadevan, "Multiaxial high-cycle fatigue criterion and life prediction for metals," *Int. J. Fatigue*, 2005, doi: 10.1016/j.ijfatigue.2005.01.003.

[78] X. Chen, S. Xu, and D. Huang, "Critical plane-strain energy density criterion for multiaxial low-cycle fatigue life under non-proportional loading," *Fatigue Fract. Eng. Mater. Struct.*, vol. 22, no. 8, pp. 679–686, 1999, doi: 10.1046/j.1460-2695.1999.00199.x.

[79] C. Han, X. Chen, and K. S. Kim, "Evaluation of multiaxial fatigue criteria under irregular loading," *Int. J. Fatigue*, vol. 24, no. 9, pp. 913–922, 2002, doi: 10.1016/S0142-1123(02)00013-0.

[80] B. M. Lei *et al.*, "Toward consistent fatigue crack initiation criteria for 304L austenitic

stainless steel under multi-axial loads," *Int. J. Fatigue*, vol. 75, pp. 57–68, 2015, doi: 10.1016/j.ijfatigue.2015.02.001.

[81] R. A. Cláudio, L. Reis, and M. Freitas, "Biaxial high-cycle fatigue life assessment of ductile aluminium cruciform specimens," *Theor. Appl. Fract. Mech.*, 2014, doi: 10.1016/j.tafmec.2014.08.007.

[82] J. Morrow, *Cyclic plastic strain energy and fatigue of metals*. ASTM International, 1965.

[83] F. Ellyin and K. Golos, "Multiaxial fatigue damage criterion," *J. Eng. Mater. Technol. Trans. ASME*, vol. 110, no. 1, pp. 63–68, 1988, doi: 10.1115/1.3226012.

[84] F. Ellyin, "Cyclic strain energy densitiy as a criterion for multiaxial failure fatigue." pp. 571–583, 1989.

[85] F. Ellyin and D. Kujawski, "A Multiaxial Fatigue Criterion Including Mean-Stress Effect," *Adv. Multiaxial Fatigue*, pp. 55–66, 1993, doi: 10.1520/stp24795s.

[86] Y. S. Garud, "A New Approach to the Evaluation of Fatigue Under Multiaxial Loadings," *J. Eng. Mater. Technol.*, vol. 103, no. 2, p. 118, 1981, doi: 10.1115/1.3224982.

[87] P. A. Glinka G, Wang G, "Mean stress effects in multiaxial fatigue," *Fatigue Fract Eng Mater Struct*, vol. 18, no. 7–8, pp. 755–764, 1995.

[88] H. Jahed, A. Varvani-Farahani, M. Noban, and I. Khalaji, "An energy-based fatigue life assessment model for various metallic materials under proportional and non-proportional loading conditions," *Int. J. Fatigue*, 2007, doi: 10.1016/j.ijfatigue.2006.07.017.

[89] G. R. Ahmadzadeh and A. Varvani-Farahani, "Energy-based damage descriptions to assess fatigue life of steel samples undergoing various multiaxial loading spectra," *Int. J. Damage Mech.*, vol. 28, no. 1, pp. 35–57, 2019, doi: 10.1177/1056789517741531.

[90] Z. Mróz, "On the description of anisotropic workhardening," *J. Mech. Phys. Solids*, vol. 15, no. 3, pp. 163–175, 1967, doi: 10.1016/0022-5096(67)90030-0.

[91] Y. S. Garud, "Prediction of Stress-Strain Response under General Multiaxial Loading," *Mech. Test. Deform. Model Dev. ASTM*, pp. 223–238, 1982.

[92] D. Kurath, P., Downing, S. D. and Galliart, "Summary of non-hardened notched shaft round robin program," *Multiaxial Fatigue Anal. Exp. SAE*, pp. 12–32, 1989.

[93] D. V. Nelson and A. Rostami, "Biaxial Fatigue of A533B Pressure Vessel Steel," *J. Press. Vessel Technol.*, vol. 119, no. 3, p. 325, 1997, doi: 10.1115/1.2842312.

[94] R. M. Lin, H., Nayeb-Hashemi, H., Pelloux, "A multiaxial fatigue damage model for orthotropic materials under proportional loading," *Fatigue Fract. Engng Mater. Struct*, vol. 16, no. 7, pp. 723–742, 1993.

[95] J. . Kim, K. S., Park, J. C. Lee, “Multiaxial fatigue under variable amplitude loads,” *J. Eng. Mater. Technol*, vol. 121, no. 3, pp. 286–293, 1999.

[96] Y. Jiang, O. Hertel, and M. Vormwald, “An experimental evaluation of three critical plane multiaxial fatigue criteria,” *Int. J. Fatigue*, vol. 29, no. 8, pp. 1490–1502, 2007, doi: 10.1016/j.ijfatigue.2006.10.028.

[97] W. N. Findley, “A Theory for the Effect of Mean Stress on Fatigue of Metals Under Combined Torsion and Axial Load or Bending,” *J. Eng. Ind.*, vol. 81, no. 4, pp. 301–305, 1959.

[98] A. Fatemi and D. F. Socie, “A Critical Plane Approach To Multiaxial Fatigue Damage Including Out-of-Phase Loading,” *Fatigue Fract. Eng. Mater. Struct.*, vol. 11, no. 3, pp. 149–165, 1988, doi: 10.1111/j.1460-2695.1988.tb01169.x.

[99] I. V. Papadopoulos, “Critical plane approaches in high-cycle fatigue: On the definition of the amplitude and mean value of the shear stress acting on the critical plane,” *Fatigue Fract. Eng. Mater. Struct.*, vol. 21, no. 3, pp. 269–285, 1998, doi: 10.1046/j.1460-2695.1998.00459.x.

[100] M. De Freitas, B. Li, and J. L. T. Santos, “A numerical approach for high-cycle fatigue life prediction with multiaxial loading,” *Multiaxial fatigue Deform. Test. Predict. ASTM Int.*, pp. 139–156, 2000.

[101] V. Gaur, V. Doquet, E. Persent, and E. Roguet, “Effect of biaxial cyclic tension on the fatigue life and damage mechanisms of Cr-Mo steel,” *Int. J. Fatigue*, 2016, doi: 10.1016/j.ijfatigue.2016.01.021.

[102] R. Branco, F. V. Antunes, and J. D. Costa, “A review on 3D-FE adaptive remeshing techniques for crack growth modelling,” *Eng. Fract. Mech.*, vol. 141, pp. 170–195, Jun. 2015, doi: 10.1016/j.engfracmech.2015.05.023.

[103] M. Baydoun and T. P. Fries, “Crack propagation criteria in three dimensions using the XFEM and an explicit-implicit crack description,” *Int. J. Fract.*, vol. 178, pp. 51–70, 2012, doi: 10.1007/s10704-012-9762-7.

[104] N. Moes, J. Dolbow, and T. Belytschko, “A finite element method for crack growth without remeshing,” *Int. J. Numer. Methods Eng.*, vol. 46, no. 1, pp. 131–150, Sep. 1999, doi: 10.1002/(SICI)1097-0207(19990910)46:1<131::AID-NME726>3.0.CO;2-J.

[105] P. Grassl, Z. P. Bazant, and G. Cusatis, “Lattice-cell approach to quasibrittle fracture modeling,” *Comput. Model. Concr. Struct.*, vol. 6, pp. 263–268, 2006, [Online]. Available: http://eprints.gla.ac.uk/31957/.

[106] S. A. Silling and E. Askari, “A meshfree method based on the peridynamic model of solid mechanics,” *Comput. Struct.*, vol. 83, no. 17–18, pp. 1526–1535, 2005, doi: 10.1016/j.compstruc.2004.11.026.

[107] H. Wei, H. Chen, and Y. Liu, “A Nonlocal Lattice Particle Model for J2 Plasticity,” *Int. J. Numer. Methods Eng.*, vol. 121, no. 24, pp. 5469–5489, 2020, [Online].

Available: https://doi.org/10.1002/nme.6446.

[108] H. Wei and Y. Liu, “An energy-based model to assess multiaxial fatigue damage under tension-torsion and tension-tension loadings,” *Int. J. Fatigue*, vol. 141, p. 105858, Dec. 2020, doi: 10.1016/j.ijfatigue.2020.105858.

[109] H. Wei and Y. Liu, “An energy-based model to assess multiaxial fatigue damage under tension-torsion and tension-tension loadings,” *Int. J. Fatigue*, vol. 141, no. April, p. 105858, 2020, doi: 10.1016/j.ijfatigue.2020.105858.

[110] T. Zhao, J. Zhang, and Y. Jiang, “A study of fatigue crack growth of 7075-T651 aluminum alloy,” *Int. J. Fatigue*, vol. 30, no. 7, pp. 1169–1180, 2008, doi: 10.1016/j.ijfatigue.2007.09.006.

[111] J. W. Feng, C. F. Li, S. Cen, and D. R. J. Owen, “Statistical reconstruction of two-phase random media,” *Comput. Struct.*, vol. 137, pp. 78–92, 2014.

[112] A. Der Kiureghian and J.-B. Ke, “The stochastic finite element method in structural reliability,” *Probabilistic Eng. Mech.*, vol. 3, no. 2, pp. 83–91, 1988.

[113] Y. Jiao, F. H. Stillinger, and S. Torquato, “Modeling heterogeneous materials via two-point correlation functions: Basic principles,” *Phys. Rev. E - Stat. Nonlinear, Soft Matter Phys.*, vol. 76, no. 3, pp. 1–37, 2007, doi: 10.1103/PhysRevE.76.031110.

[114] H. Kim and M. D. Shields, “Modeling strongly non-Gaussian non-stationary stochastic processes using the iterative translation approximation method and Karhunen–Loève expansion,” *Comput. Struct.*, vol. 161, pp. 31–42, 2015.

[115] H. Chen, L. Meng, S. Chen, Y. Jiao, and Y. Liu, “Numerical investigation of microstructure effect on mechanical properties of bi-continuous and particulate reinforced composite materials,” *Comput. Mater. Sci.*, vol. 122, pp. 288–294, 2016, doi: 10.1016/j.commatsci.2016.05.037.

[116] H. Chen and Y. Liu, “Deformation and failure analyses of cross-ply laminates using a nonlocal discrete model,” *Compos. Struct.*, vol. 152, pp. 1001–1013, 2016, doi: 10.1016/j.compstruct.2016.06.054.

[117] A. Krizhevsky, I. Sutskever, and G. E. Hinton, “ImageNet Classification with Deep Convolutional Neural Networks,” *Adv. Neural Inf. Process. Syst.*, pp. 1097–1105, 2012, Accessed: Apr. 03, 2021. [Online]. Available: http://code.google.com/p/cuda-convnet/.

[118] D. Amodei *et al.*, “Deep Speech 2 : End-to-End Speech Recognition in English and Mandarin,” in *International conference on machine learning*, 2016, pp. 173–182.

[119] V. Mnih *et al.*, “Human-level control through deep reinforcement learning,” *Nature*, vol. 518, no. 7540, p. 529, 2015.

[120] R. Cang, H. Li, H. Yao, Y. Jiao, and Y. Ren, “Improving direct physical properties prediction of heterogeneous materials from imaging data via convolutional neural network and a morphology-aware generative model,” *Comput. Mater. Sci.*, vol. 150,

pp. 212–221, Jul. 2018, doi: 10.1016/j.commatsci.2018.03.074.

[121] M. A. Bessa *et al.*, “A framework for data-driven analysis of materials under uncertainty: Countering the curse of dimensionality,” *Comput. Methods Appl. Mech. Engrg*, vol. 320, pp. 633–667, 2017, doi: 10.1016/j.cma.2017.03.037.

[122] X. Li, Z. Liu, S. Cui, C. Luo, C. Li, and Z. Zhuang, “Predicting the effective mechanical property of heterogeneous materials by image based modeling and deep learning,” *Comput. Methods Appl. Mech. Eng.*, vol. 347, pp. 735–753, 2019, doi: 10.1016/j.cma.2019.01.005.

[123] I. M. Nikbin, S. Rahimi R., and H. Allahyari, “A new empirical formula for prediction of fracture energy of concrete based on the artificial neural network,” *Eng. Fract. Mech.*, vol. 186, pp. 466–482, Dec. 2017, doi: 10.1016/j.engfracmech.2017.11.010.

[124] V. Kushvaha, S. Anand Kumar, P. Madhushri, and A. Sharma, “Artificial neural network technique to predict dynamic fracture of particulate composite,” *J. Compos. Mater.*, vol. 54, no. 22, pp. 3099–3108, 2020, doi: 10.1177/0021998320911418.

[125] Y. C. Hsu, C. H. Yu, and M. J. Buehler, “Using Deep Learning to Predict Fracture Patterns in Crystalline Solids,” *Matter*, vol. 3, no. 1, pp. 197–211, 2020, doi: 10.1016/j.matt.2020.04.019.

[126] M. Kim, N. Winovich, G. Lin, and W. Jeong, “Peri-Net: Analysis of Crack Patterns Using Deep Neural Networks,” *J. Peridynamics Nonlocal Model.*, vol. 1, no. 2, pp. 131–142, 2019, doi: 10.1007/s42102-019-00013-x.

[127] K. Hornik, “Approximation capabilities of multilayer feedforward networks,” *Neural Networks*, vol. 4, no. 2, pp. 251–257, Jan. 1991, doi: 10.1016/0893-6080(91)90009-T.

[128] L. Cun *et al.*, “Handwritten Digit Recognition with a Back-Propagation Network,” in *Advances in neural information processing systems*, 1990, pp. 396–404.

[129] M. D. Zeiler, G. W. Taylor, and R. Fergus, “Adaptive deconvolutional networks for mid and high level feature learning,” in *Proceedings of the IEEE International Conference on Computer Vision*, 2011, pp. 2018–2025, doi: 10.1109/ICCV.2011.6126474.

[130] C. Szegedy *et al.*, “Going Deeper with Convolutions,” in *Proceedings of the IEEE conference on computer vision and pattern recognition*, 2015, pp. 1–9.

[131] S. Ioffe and C. Szegedy, “Batch Normalization: Accelerating Deep Network Training by Reducing Internal Covariate Shift,” in *International conference on machine learning*, Jun. 2015, pp. 448–456, Accessed: Apr. 03, 2021. [Online]. Available: http://proceedings.mlr.press/v37/ioffe15.html.

[132] C. Szegedy, V. Vanhoucke, S. Ioffe, and J. Shlens, “Rethinking the Inception Architecture for Computer Vision,” in *Proceedings of the IEEE conference on computer vision and pattern recognition*, 2016, pp. 2818–2826.

[133] K. Simonyan and A. Zisserman, “Very deep convolutional networks for large-scale

image recognition," Sep. 2015, Accessed: Apr. 03, 2021. [Online]. Available: http://www.robots.ox.ac.uk/.

[134] K. He, X. Zhang, S. Ren, and J. Sun, "Deep Residual Learning for Image Recognition," in *Proceedings of the IEEE Conference on Computer Vision and Pattern Recognition*, 2016, pp. 770–778, Accessed: Apr. 03, 2021. [Online]. Available: http://image-net.org/challenges/LSVRC/2015/.

[135] H. Noh, S. Hong, and B. Han, "Learning Deconvolution Network for Semantic Segmentation," in *Proceedings of the IEEE International Conference on Computer Vision*, 2015, pp. 1520–1528.

[136] J. Long, E. Shelhamer, and T. Darrell, "Fully Convolutional Networks for Semantic Segmentation," in *Proceedings of the IEEE Conference on Computer Vision and Pattern Recognition (CVPR)*, 2015, pp. 3431–3440.

[137] T.-Y. Lin, P. Dollár, R. Girshick, K. He, B. Hariharan, and S. Belongie, "Feature Pyramid Networks for Object Detection," in *Proceedings of the IEEE Conference on Computer Vision and Pattern Recognition*, 2017, pp. 2117–2125.